INFORMATION TO USERS

This material was produced from a microfilm copy of the original document. While the most advanced technological means to photograph and reproduce this document have been used, the quality is heavily dependent upon the quality of the original submitted.

The following explanation of techniques is provided to help you understand markings or patterns which may appear on this reproduction.

1. The sign or "target" for pages apparently lacking from the document photographed is "Missing Page(s)". If it was possible to obtain the missing page(s) or section, they are spliced into the film along with adjacent pages. This may have necessitated cutting thru an image and duplicating adjacent pages to insure you complete continuity.

2. When an image on the film is obliterated with a large round black mark, it is an indication that the photographer suspected that the copy may have moved during exposure and thus cause a blurred image. You will find a good image of the page in the adjacent frame.

3. When a map, drawing or chart, etc., was part of the material being photographed the photographer followed a definite method in "sectioning" the material. It is customary to begin photoing at the upper left hand corner of a large sheet and to continue photoing from left to right in equal sections with a small overlap. If necessary, sectioning is continued again — beginning below the first row and continuing on until complete.

4. The majority of users indicate that the textual content is of greatest value, however, a somewhat higher quality reproduction could be made from "photographs" if essential to the understanding of the dissertation. Silver prints of "photographs" may be ordered at additional charge by writing the Order Department, giving the catalog number, title, author and specific pages you wish reproduced.

5. PLEASE NOTE: Some pages may have indistinct print. Filmed as received.

University Microfilms International
300 North Zeeb Road
Ann Arbor, Michigan 48106 USA
St. John's Road, Tyler's Green
High Wycombe, Bucks, England HP10 8HR

78-4708

GILLIGAN, John Gerard, 1949-
NEUTRAL ATOM TRANSPORT IN TOKAMAK PLASMAS
BY MULTIGROUP DISCRETE ORDINATES METHODS.

The University of Michigan, Ph.D., 1977
Physics, fluid and plasma

University Microfilms International, Ann Arbor, Michigan 48106

NEUTRAL ATOM TRANSPORT IN TOKAMAK PLASMAS BY MULTIGROUP DISCRETE ORDINATES METHODS

by
John Gerard Gilligan

A dissertation submitted in partial fulfillment
of the requirements for the degree of
Doctor of Philosophy
(Nuclear Engineering)
in The University of Michigan
1977

Doctoral Committee:

Professor Terry Kammash, Chairman
Professor James Duderstadt
Professor Ward D. Getty
Professor William Kerr
Professor Richard K. Osborn
Samuel L. Gralnick, Princeton
Plasma Physics Laboratory

ACKNOWLEDGMENTS

There are many people, without whose help, this investigation might not have been carried out. From the beginning, I owe a debt of gratitude to my advisor, Professor Terry Kammash, for encouragement in times of dim light and for his firm but free hand in continued guidance.

At the Princeton Plasma Physics Laboratory, where the majority of this research has been conducted, my advisors "away from home" deserve special recognition: Dr. Samuel Gralnick and Dr. William G. Price, Jr., for their careful direction, immeasurable patience, and inspiring confidence in my ability to successfully complete this work.

I express sincere gratitude to Dr. Robert G. Mills as head of the Fusion Reactor Design Division, for financial support during this period and for his genuine concern throughout the project. I am also very grateful to Dr. Fred H. Tenney for many stimulating discussions on the subject of neutral atom transport. The support of all the other members of the Division has, indeed, been important, but I would especially like to thank Dr. Charles Bathke for his timely encouragement and open ear policy.

A special compliment is paid to Mrs. Connie Hopkins for answering many questions about the preparation of the manuscript, and to Miss Marjorie Halliday for her

painstaking efforts in typing and assembling the drafts of this dissertation.

I gratefully acknowledge the financial assistance of the Atomic Energy Commission in the form of a Nuclear Traineeship while at the University of Michigan.

I would like to take this opportunity to dedicate this dissertation to my parents; without whose faith, this work would not have been possible.

TABLE OF CONTENTS

ACKNOWLEDGEMENTS..... ii

LIST OF TABLES..... v

LIST OF ILLUSTRATIONS..... vii

LIST OF APPENDICES..... ix

NOMENCLATURE..... x

CHAPTER

I. INTRODUCTION..... 1

Problem Definition
Background Material

II. THE NEUTRON - NEUTRAL ANALOGY..... 17

Neutron and Neutral Interactions
The Neutron Transport Equation
Methods for Solution

III. THE MULTIGROUP DISCRETE ORDINATES (MGDO) FORMULATION..... 42

The Neutral Transport Equation
The Neutral Multigroup Equations
Multigroup Discrete
Ordinates Methods

IV. NUMERICAL SOLUTIONS..... 63

Generation of the Multigroup
Cross sections
Transport Code Utilization

V. THE USEFULNESS OF MGDO NEUTRAL SOLUTIONS..... 110

The More Rigorous MGDO Method
A Benchmark Problem
The Neutral Module Application

VI. CONCLUDING REMARKS..... 147

APPENDICES..... 149

LIST OF REFERENCES..... 171

LIST OF TABLES

Table		Page
II.1	Reflection coefficients for hydrogen atoms incident on metallic surfaces.....	35
IV.1	Parameters for the fits used to determine plasma densities and temperatures.....	86
IV.2	Results for different total numbers of energy groups and spatial intervals for the TFTR plasma.....	94
IV.3	Spatial mesh structure for the TFTR plasma.....	98
IV.4	Comparison of P_0, P_1 and P_3 scattering results in a homogeneous plasma slab.....	100
IV.5	Comparison of results for different orders of scattering and angular quadrature for the TFTR plasma.....	103
IV.6	The plasma zone structure generated for a_n = .95 in the TFTR plasma.....	107
IV.7	Comparison of results for different convergence criteria and plasma zone structures for the TFTR plasma.....	108
V.1	A summary of approximations used in neutral transport studies.....	112
V.2	Effects of approximations for the charge exchange reaction product and geometry configuration for the TFTR plasma.....	119
V.3	Summary of parameters for the MGDO code ANISN in the comparison study.....	124

LIST OF TABLES

Table		Page
V.4	Summary of parameters for the generation method in the comparison study.....	125
V.5	Summary of neutral transport results for the comparison study.....	129
V.6	Charge exchange power loss for the ST tokamak.....	135
V.7	Comparison of time reduction runs for the TFTR plasma.....	140
V.8	Results of forward and reverse group structure, initial flux approximations, and inner iteration limit for the TFTR plasma.....	142

LIST OF ILLUSTRATIONS

Figure		Page
1.1	The principle parts of a tokamak.....	5
2.1	Possible interactions of hydrogen atoms with plasma.....	20
2.2	The neutral interaction cross sections....	23
3.1	Schematic representation of the charge exchange collision.....	47
4.1	Behavior of the function I_{ℓ}.....	67
4.2	The effective interaction rates of hydrogen atoms incident on Maxwellian targets..	69
4.3	Flow of the calculations done in the code GIMUXS.....	78
4.4	Plasma temperature and density profiles for the ST and TFTR plasmas.....	85
4.5	The fraction of total particles in a Maxwellian flux distribution (A) with energy less than ε.....	90
4.6	The energy group limits formed for various values of the parameter k.....	92
4.7	Hydrogen atom densities for the TFTR tokamak calculated using different total numbers of groups.....	93
4.8	The spectrum of outfluxed neutrals for TFTR using different total number of groups.....	95

LIST OF ILLUSTRATIONS

Figure		Page
5.1	The charge exchange reactions product ($v\ \sigma_{cx}$).....	118
5.2	Calculated hydrogen atom densities for the ST and TFTR tokamaks by the MGDO and generation methods.....	126
5.3	The spectrum of outfluxed neutrals for the ST tokamak by the MGDO and generation methods.....	130
5.4	The spectrum of outfluxed neutrals for the TFTR tokamak by the MGDO and generation methods.....	131
C.1	Orientation of vectors for the integration of equation (C.21) in infinite cylindrical geometry.....	166
C.2	The ratio of $Ki_1(\rho)$ to $e^{-\rho}$ for values of the argument ρ.....	169

LIST OF APPENDICES

Appendix		Page
A.	THE NEUTRAL MULTIGROUP CROSS SECTION CODE-GIMUXS.....	149
B.	THE NEUTRAL ANALYSIS PROGRAM-NEUTER....	154
C.	GENERATION METHOD NEUTRAL TRANSPORT....	157

NOMENCLATURE

$A(x)$	Fraction of total particles in a Maxwellian flux distribution with normalized energy less than x.
A	Atomic mass number.
a_n	Zone structure constant.
B	Conversion constant from energy in $eV^{\frac{1}{2}}$ to speed in cm sec^{-1} for hydrogen atoms $= 1.39 \times 10^6$ cm sec^{-1} $eV^{-\frac{1}{2}}$.
C	A constant value of the charge exchange reaction rate (cm^3 sec^{-1}).
c	Speed of light $= 2.99 \times 10^{10}$ cm sec^{-1}.
E, E', E_T	Particle energies (eV).
E_g, E_h	Energies of group limits (eV).
$\bar{E}_g$	Arithmetic mean group energy (eV).
$f_{i,e}$	Non-isotropic ion and electron distribution functions.
H_i^g	The function of particles in group g of a Maxwellian density distribution.
$h_{i,e}$	Isotropic ion and electron distribution functions.

I	Symbol for an integral to be evaluated.
I_{ℓ}	Legendre coefficient integral of the charge exchange scattering kernel.
K_s^{eff}	The charge exchange scattering kernel.
$K_{s\ell}$	Legendre coefficient of the charge exchange scattering kernel.
$K_{s\ell}^{h\rightarrow g}$	Group-to-group, Legendre coefficient, charge exchange scattering cross section.
Ki_1	The first repeated integral of the Bessel function.
k	Group structure constant.
$N_{i,e}$	Plasma ion or electron density (cm^{-3}).
n, n^g	Neutral density (cm^{-3}).
$P, P_{\underline{v}_T}, P^{eff}$	Scattering probability functions.
$P_{(\underline{r})}, P', P''$	Integration limit points.
P_{ℓ}	The Legendre Polynominal.
Q	External stationary particle source (cm^{-3} sec^{-1}).
r_o	Minor radius of the plasma (cm).

$T_{i,e}$	Plasma ion or electron temperature (eV).
$\underline{v}, \underline{v}', \underline{v}_T$ $\underline{v}_{Eg}, \underline{v}_n$	Particle velocity vectors (cm sec^{-1}).
Z	Atomic charge state.
Φ	Angular particle flux (cm^{-2} sec^{-1} per unit solid angle and unit energy).
ϕ_ℓ	Legendre flux moment.
Φ_g	Group flux.
σ_s, σ_a	Macroscopic scattering and total absorption cross sections (cm^{-1}).
$\sigma_s^{eff}, \sigma_a^{eff}$	Macroscopic effective scattering and total absorption cross sections in a moving media (cm^{-1}).
$\sigma_{a,g}$	Total group absorption cross section.
$\sigma_{ii}, \sigma_{ei}, \sigma_{cx}$	Microscopic ion impact ionization, electron impact ionization and charge exchange cross sections (cm^2).
$\underline{\Omega}, \underline{\Omega}', \underline{\Omega}_T$	Particle direction vectors.
$d\Omega, d\Omega', d\Omega_T$	Elements of solid angle.
$\langle \sigma v \rangle$	Averaged reaction rate ($cm^3 sec^{-1}$).

CHAPTER I

INTRODUCTION

Problem Definition

The purpose of this dissertation is to examine the feasibility, practicality and usefulness of employing multigroup discrete ordinates (MGDO) neutron transport methods for the calculation of low energy neutral atom transport in tokamak plasmas.

Our motivation stems from several sources: An awareness that fewer approximations are used by MGDO methods than in previous neutral analyses, the convenience offered by the existing set of versatile MGDO transport equation solvers, and the desire to decrease the computation time of a neutral module in a larger plasma simulation code. As will be seen, neutral atoms play a primary role in the evolution of the tokamak discharge. Thus, a precise determination of this transport process is essential for a complete understanding of a tokamak reactor which is envisioned as a thermonuclear power source.

Proposal

As early as 1959 Zubarev and Klimov [1] used a neutron transport solution technique to analyze neutral behavior in a plasma. However, it was not until 1974 that Greenspan [2]

pointed out the feasibility of using MGDO neutron computational methods for the same problem. The application is made possible because the interactions of neutral atoms with a plasma are analogous to those of neutrons diffusing in a medium and hence, are governed by the same Boltzmann transport equation. In the present investigation an approach similar to that of Greenspan is taken, but a more thorough examination is made of neutral interactions and an alternate derivation is given for the multigroup equations.

The practicality of MGDO neutral analysis is demonstrated by numerically generating the appropriate multigroup cross sections and obtaining solutions for a realistic plasma-neutral model with the MGDO transport code ANISN [3]. It is shown that the operational parameters of the code treat fully all aspects of the neutral transport process.

Because of the importance of neutral behavior in tokamak plasmas many methods have previously been developed for their analysis [1,4-10]. However, a number of approximations have been introduced to arrive at tractable solutions and to speed up computer calculation time. The advantage of MGDO methods, which will be demonstrated, is that fewer approximations are utilized in treating the transport problem. The usefulness of the MGDO method as a standard in the calculations of neutral benchmark problems is therefore self evident. Accordingly, a comparison study with the widely used neutral transport module of the Düchs

plasma simulation code [8] reveals significant errors associated with their initial approximations.* The suitability of the MGDO methods in the same neutral module application is also evaluated.

Organization

The remaining section in this chapter discusses the role of the neutral species in tokamak discharges and reviews the literature which has described neutral behavior. The analogy between neutral particle transport and neutron transport is developed in Chapter II by examining the basic particle interactions. The derivation of the neutral multigroup equations, including the charge exchange scattering source, constitutes Chapter III. The numerical evaluation of the multigroup cross sections is performed and the MGDO transport equations are solved in Chapter IV. Chapter V evaluates the effects of previously used approximations and presents the results of the comparison study.

Background Material

Neutral Processes

There are two types of particles in fusion systems; charged and uncharged. The former category consists of ions and electrons and is by far the most abundant. The latter group is referred to as neutral and may include atoms and

*A newer version of the code employs a Monte Carlo algorithm with improved accuracy.

molecules, either in excited or ground states. Neutrals, as well as plasma ions, can further be classified as belonging to the working (filling) gas component of the discharge or to an ever present impurity component.

Shown schematically in Figure 1.1 are the main features of a tokamak system emphasizing neutral particle sources. A current is induced in the plasma by the action of external coils which simultaneously heats the plasma (along with the neutral beam) and provides a confining (poloidal) magnetic field. Other coils (toroidal, vertical field, etc.) also aid in the overall confinement and control scheme. The beneficial goal of separation of plasma and solid material (vacuum wall) during the discharge is only loosely met, however, and so plasma particles leak out, contacting the vacuum chamber wall. In a similar manner it is possible for material originating outside the plasma to be transported into the discharge region.

Electron densities in current tokamaks range from $\sim .1 - 10 \times 10^{13}$ cm^{-3} with temperatures from tens of electron volts to several keV (with lower temperatures and densities at the plasma edge). The plasma itself is not a pure mixture of the working gas (H or He, or D, T in future machines) but is contaminated with a number of impurities. These include light elements ($\sim 10^{12}$ cm^{-3} C or O) originating from outgassing or desorption at the vacuum wall and heavier ions (Fe, W, Mo, etc.) resulting from sputtering or evaporation of the wall or plasma limiter. The length of

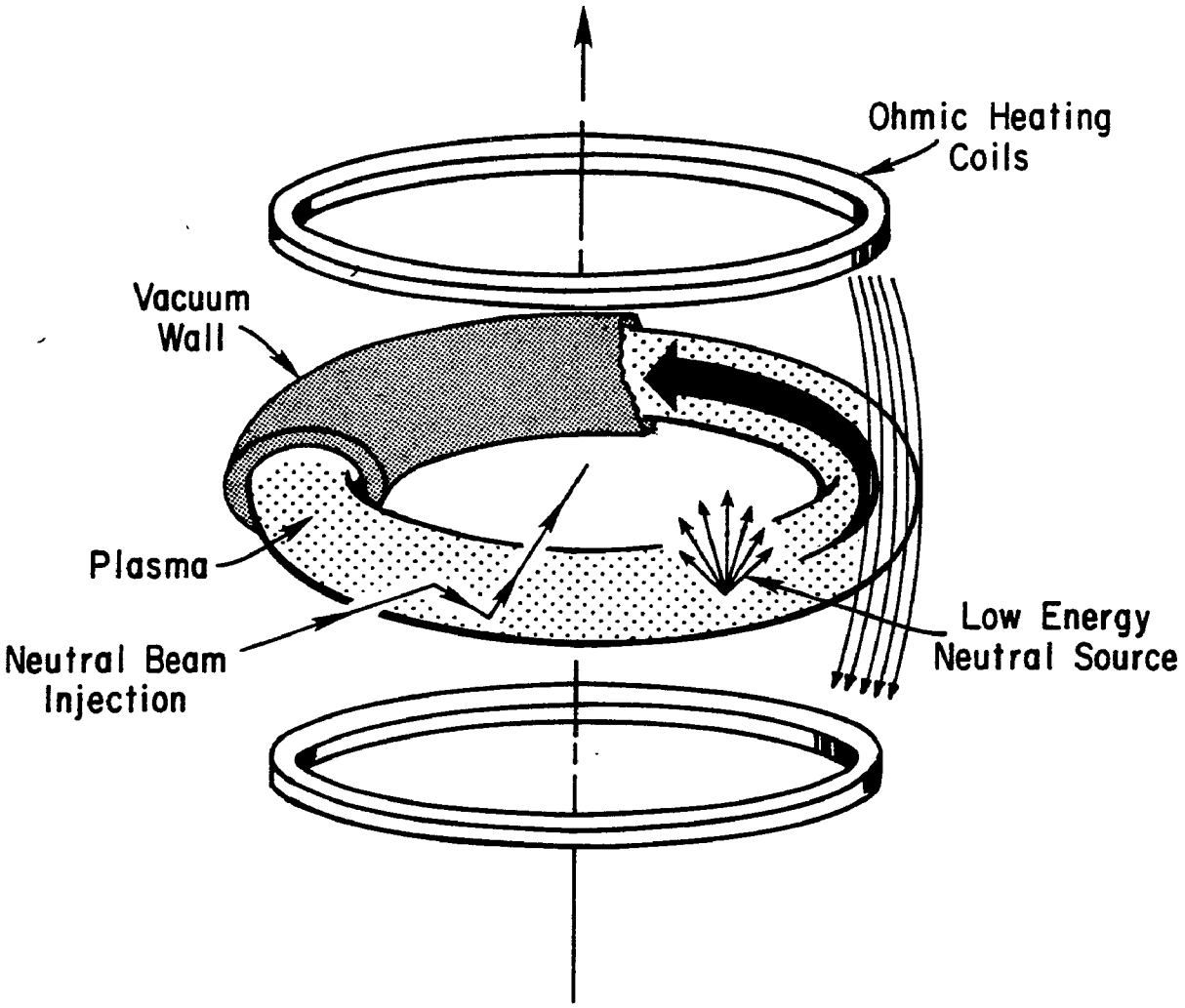

Figure 1.1 The principle parts of a tokamak illustrating neutral particle sources.

current tokamak discharges is on the order of several hundreds of milliseconds.

The size and proportions of tokamaks vary from machine to machine. The vacuum wall radii in current versions are in the range 10 - 45 cm but are envisioned to increase to 75 - 200 cm in future devices. Likewise, the major toroidal radius will increase from 100 - 150 cm in present tokamaks to 300 - 400 cm for machines in the design stages.

A more detailed description of tokamaks and their operation can be obtained in several of the references [11-14].

The Neutral Source

The majority of neutrals present in tokamak systems are not introduced deliberately but arise necessarily because of the particle interchange between the hot plasma and the "cold" (neutral) vacuum wall. This appears as a recycling process at the plasma boundary during the course of the discharge [8,12]. The background neutral population originating from this source has a profound effect on the evolution of the plasma and is the subject of this investigation.

The primary source of background neutrals is the desorption of particles attached to the surface of the vacuum wall. These may be working gas atoms or molecules (we will assume H or H_2 although D and T exhibit the same behavior) adsorbed prior to or during the discharge, or working gas atoms which have diffused out of the wall (the wall temperature increases during the discharge due to

energetic particle and radiation deposition).

The desorption process may involve several mechanisms: particle impact desorption (resulting from the outflux of plasma ions, electrons, and neutrals), photo-desorption (from radiation bombardment) and thermal desorption of loosely bound molecules. The desorbed molecules leave the wall surface with only a small amount of energy, typically < .1 eV. Upon coming in contact with the plasma immediately adjacent to the wall it is most likely that the molecules will undergo dissociative ionization (within centimeters) resulting in the formation of a neutral-ion pair with several volts of energy [15,16]. Since the neutral is not hampered by the electromagnetic forces that effect the charged particles it is now possible for it to stream (on the order of centimeters) into warmer plasma regions before undergoing another interaction. The interaction mean free path for incident neutrals is normally small in comparison to the minor plasma radius (i.e., many collisions occur in the plasma edge region).

As will be shown in Chapter II the primary interaction mechanisms for the incoming 3 eV hydrogen neutral will be ionization by electron impact or charge exchange with a working gas ion (we assume a proton). In general charge exchange is dominant (see Figure 4.2), and the resulting neutral (originally the proton) can be directed in any direction including further into the plasma core or towards the vacuum wall. The ensuing cascade of charge exchange

neutrals allows the penetration of working gas atoms into the hot plasma core and also creates an outflux of charge exchange neutrals at the plasma boundary. The flux of neutrals decreases as the plasma axis is approached owing to ionization and the local neutral energy is determined largely by the local ion temperature.

Outfluxed neutrals* can either be absorbed or reflected, (perhaps with some energy degradation) at the boundary. Energy is transferred by collisions to particles adsorbed on the surface or to the lattice atoms of the vacuum wall metal which may result in sputtering. The effect of the reflective boundary condition (as opposed to complete absorption) is to permit the escaping neutrals to penetrate back into the plasma with a corresponding increase in neutral density [7].

The timescale for neutral transport is on the order of several transit times of an average energy neutral across the plasma (~ 10 μsec). Plasma diffusion and buildup, as well as energy conduction and convection, occurs on a much slower timescale[12] and so fixed plasma conditions can be assumed as the neutrals relax to the steady state.

Impurity neutrals play a negligible role in the transport of working gas neutrals. The impurity atoms (with $Z > 1$) are multiply ionized quickly by electron impact and

*The term "outflux" actually refers to the outward current (cm^{-2} sec^{-1}) of neutrals (primarily due to charge exchange) at the outer plasma boundary.

the cross sections for nonresonant charge exchange with working gas ions are very small in this energy regime. The partially or fully stripped impurity ions do, however, have a dramatic effect on the plasma discharge by increasing plasma resistivity and radiation loss rates (line and bremsstrahlung), and by seriously altering plasma confinement times.

The background neutral population may be additionally fed by three other sources. These are; recombination of plasma ions and electrons, neutral beam injection and neutral gas puffing. Recombination (even in the cool edge region of tokamak plasmas) is unlikely, however, since temperatures are generally greater than 1 eV (the threshold where recombination could be significant). Likewise, the charge exchange neutrals resulting from the deposition of high energy neutral beams in the plasma (for heating purposes) can usually be neglected since their contribution to the total neutral density is small even at projected beam power levels. External gas puffing in recent experiments has successfully raised the plasma density by introducing a volume of working gas during the discharge. The transport of these neutrals is identical to that of desorbed neutrals (provided the source geometry is the same) and therefore this source need not be considered in a separate analysis.

Neutral Effects

Despite the relatively small population of neutral atoms in the tokamak system their presence plays a major role in

the development of the discharge. The incoming neutrals constitute a net source of plasma ions through ionization. In present day tokamaks this is the primary method of replenishing or increasing the plasma ion density. The influx also becomes a way of shaping the plasma density profile since the plasma production rate is greatest near the neutral source. Thus, if the neutral influx is large enough, a plasma density peak can be generated in the region near the vacuum wall (inverted from normal discharges where the peak is on axis). Both steady state neutral gas blankets and gas puffing have been proposed for this purpose [10,17].

The charge exchange neutrals which are outfluxed from present plasma experiments (the ST tokamak) represent a sizable amount (~ 25%) of the total power loss from the tokamak [11]. The bulk of the neutrals have energies less than 300 eV that result from the first several charge exchanges in the outer regions of the plasma. Hence, the bulk of the power loss cools the area near to the vacuum wall. However, later charge exchange generations also remove energy from the plasma core. The energy spectrum of the neutral outflux has a shape characteristic of the edge ion distribution function (normally Maxwellian) with an additional high energy tail indicative of the hot core [4,18].

The background neutral population can also represent an additional significant power loss for a neutral beam heated

plasma [19]. After the initial ionization of the injected neutral the beam ion will be trapped in a confining magnetic field and transfer its energy to the thermal plasma via coulomb collisions. During the slowing down process, however, there is a probability that a charge exchange reaction can take place with a background neutral. In this event it is likely that the new hot charge exchange neutral will escape from the system taking with it all of its energy. As much as 50% of the injected neutral beam power has been reported lost in this way for the ATC tokamak [20].

Perhaps the most deleterious effect background neutrals have on tokamak operation is the introduction of wall impurities (high Z) into the plasma as a result of neutral sputtering. The current of outfluxed neutrals is large - several times greater than that expected for neutrons in a large ignited fusion device ($\sim 3 \times 10^{15}$ neutrals cm^{-2} sec^{-1}). Neutral sputtering yields are also larger than the corresponding neutron values (by nearly two orders of magnitude at appropriate energies) for first wall materials. Sputtering removes atoms from the metal surface (typically stainless steel or a refractory metal) and hence deteriorates the condition of the first wall. More importantly this allows the high Z impurity to contaminate the plasma. It will be recalled that this results in increased radiation and plasma resistivity, and contributes to confinement losses due to the onset of plasma instabilities.

Historical Review

The application of MGDO transport methods to neutral transport is a relatively new approach. There has been activity in background neutral analysis though for some time. In the following section a historical perspective for the major transport studies is given which stresses goals and conclusions. A more detailed summary of the approximations that have gone into each analysis is delayed until Chapter V. We also include a review of concurrent studies using the MGDO method.

Zubarev and Klimov [1] (1959) examined the compatibility of a hot plasma with a "cold" vacuum wall. The allowable temperature jump between the two extremes (plasma and wall) determined the width of an intermediate plasma layer (where the neutral population present is small) which can greatly increase the size of the device. A solution was arrived at that was simultaneously characterized by a large temperature jump (permitting a small intermediate layer) and by comparatively small (technically realizable) values of heat removal from the wall. Despite simplifications in the analysis it was first recognized in this work that neutral and neutron transport could be considered analogous and an analytical neutron solution technique was used for the neutral problem.

Dnestrovski, Kostomarov and Pavlova [4] (1971) investigated the total energy balance of a tokamak system. Including the effect of charge exchange neutrals was not

able to account for experimentally observed energy confinement times which were several times smaller than previous calculations. The kinetic treatment of neutral transport demonstrated that the majority of outfluxed neutrals came from the plasma edge and revealed the outflux spectrum to contain the high energy tail observed in experiments.

Rehker and Wobig [5] (1973) were interested in determining the effect that a more realistic ion distribution function would have on neutral transport. The work of Dnestrovski et al., had approximated this by a δ-distribution ($\delta(v=v_i)$; v_i = thermal velocity of the ions). Several reflection mechanisms for outfluxed neutrals were also taken into account. The δ-distribution results were found to be very close to those of a Maxwellian plasma. Wall reflection increased the neutral density profiles by a factor of 2-4. Quantitive comparison with experimental data was not possible since only homogeneous plasmas were considered.

The analysis of Hogan and Clarke [6] (1974) was concerned with the properties of outfluxed neutrals; especially as the results pertained to neutral sputtering (and the introduction of high Z impurities into the plasma). The calculations for neutral transport were carried out over a broad range of plasma size, temperature and density profiles. The results indicated that the tendency for higher temperature plasmas to produce a greater neutral

outflux was mitigated by an increase in plasma density. Neutral sputtering rates were shown to decrease slightly for machines of future interest because the larger plasma size, which reduced the wall flux, had increased for these designs.

Nearly the same kinetic equation was solved by Clarke and Sigmar [7] (1975) as by Hogan and Clarke but a more detailed source of neutrals was considered and a wall reflection model was included. The reflection mechanism raised neutral densities by a factor of about 4 on axis and slightly increased the average neutral density near the plasma edge.

Molvig [9] (1976) investigated neutral transport as neutral gas was bled into the ALCATOR discharge chamber. An explanation was sought for the observed plasma density rise during the process. In order to circumvent numerical convergence problems associated with the high density regime of ALCATOR[17], a Fourier transform technique was used to solve the transport equation. The curvature effects of cylindrical geometry were included in the analysis. Neutral penetration to the plasma core was found not to be sufficient to account for the observed ion production rates.

The neutral transport scheme of Rutherford and Düchs [8] (1976) is especially worthy of note because of its repeated application in a tokamak plasma simulation code. This represents a strenuous test of the applicability of the method since many plasma conditions are encountered (i.e.,

wide variations in plasma temperature and density profiles during the course of a discharge). An additional constraint is imposed by the need to limit computation time for runs of this order of magnitude. Convergence problems exist in the iterative solution scheme for the high plasma density regime but the effects are relatively minor except near the plasma axis where the neutral density is low. The importance of the neutral module application leads us to examine the approximations that have gone into the Düchs method in special detail in Appendix C. The comparison study of Chapter V is prompted by the same rationale.

Greenspan [2] (1974) introduced the concept of using neutron computational methods for neutral problems. For isotropic ion and electron distributions, current versions of MGDO neutron codes were found to be sufficient. As an initial application, a simplified energy treatment (multispecies), where neutrals charge exchanging in a given spatial interval acquired the local thermal ion velocity, was used. The extension to a full multigroup analysis where the details of energy and angular distributions could be considered was not undertaken. Gilligan, Gralnick, and Price [21] (1974) likewise considered a simplified attenuation problem for neutral oxygen in the edge region of a plasma with a MGDO code.

Marable and Oblow [22] (1975) applied the full multigroup treatment to the hydrogen neutral problem and obtained neutral profiles for the ORMAK tokamak. Similar

studies of the MGDO method were performed by El Derini and Gelbard [23] (1976) using the EPR tokamak and by Gilligan, Gralnick, Price and Kammash [24] (1976) for the TFTR and ST tokamaks. The emphasis in all three investigations was the generation of the appropriate multigroup cross sections and the establishment of operating parameters for the MGDO transport code to assure calculational accuracy. Pfeiffer [25] (1976) has compared MGDO results with a one-dimensional integral equation method and also used a two-dimensional MGDO code in a special application. The conclusion was that for one-dimensional analysis the integral equation method of Burrell [26] (1976) was about a factor of 7 faster than conventional MGDO methods without a significant loss in accuracy. No analytic methods exist for neutral transport analysis in two dimensions where the MGDO code application is much more time consuming.

The specialized neutral transport application of discrete ordinates techniques in two-dimensional toroidal geometry is taken up by Wienke et al., [27] (1977).

CHAPTER II

THE NEUTRON-NEUTRAL ANALOGY

To establish the validity of using neutron transport solution techniques for neutral atom transport in plasmas it is first necessary to demonstrate that the behavior of both species are governed by the same equation. This requisite is of course determined by the forces (interactions) that effect the phase space distribution of the transported particles. If the predominant interactions are analogous then it is likely (although not necessary) that solution techniques will be identical. Additional constraints on the transport equation that must be satisfied are the imposition of boundary conditions and inclusion of proper source functions. In the present chapter the important neutron and neutral interactions are identified. Boundary conditions and source functions are also compared. The result is the formulation of a Boltzmann transport equation which is analagous for both species. A very brief summary of the possible neutron solution techniques that could be applied to the neutral problem is given.

Neutron and Neutral Interactions

Neutron Interactions with Matter

The interactions of neutrons with matter are well known and are adequately described in a number of nuclear reactor

texts [28-30]. A classification can be designed which groups the nuclear reactions according to several basic processes; absorption, scattering, and neutron producing reactions. Absorption effectively consumes neutrons in radiative capture (n,γ), and charged particle events (n,p), (n,α). Thus, in writing a balance equation for the neutron population, absorption is a sink term.

The scattering process changes the velocity vector of the reacting neutron. The incident speed and/or direction of the incident neutron can be altered; however, the number of neutrons remains constant. In an inelastic scattering, some of the initial kinetic energy is transferred to the scattering nucleus in the form of an internal excitation and hence, total kinetic energy is not conserved. An elastic scatter preserves both total momentum and kinetic energy. The dominant trend in neutron fission environs is down scatter where, after its birth at a relatively high energy (~ 2 MeV), the neutron "slows down" in the local diffusing medium. The energy of the neutron is thus transferred to the lattice. Upscattering in energy can also occur for neutrons that have slowed down to the thermal regime (< .1 eV) where energy from the lattice can be given to the neutron by elastic scattering.

The final category of neutron interactions that was alluded to earlier, produces additional neutrons (a number greater than unity) and is extremely important in the operation of any device dependent on a copious supply of

neutrons. The fission event releases a large amount of energy (~ 200 MeV) and usually between 2 and 3 neutrons per reaction. To a much lesser extent in a fission reactor the (γ,n), (n,2n) and (n,3n) reactions also contribute to the neutron balance. The latter two reactions are envisioned to multiply neutrons for tritium breeding in a fusion reactor device. Neutron producing reactions represent a source term in the neutron balance equation.

Several things should be noted about neutron interactions. The first is that no long range (i.e., coulomb electromagnetic) collision forces act on the neutrons because of their neutral charge state. Secondly, interactions between neutrons is neglected because the self collision probability is very low. Thirdly, in the analysis of a fission reactor the balance of neutrons is so crucial that all the aforementioned reactions (with the addition of others) must be taken into account.

Neutral Interactions with Plasma

Whereas the interaction of neutrons with matter is a nuclear process, neutral atoms interact with a plasma on the atomic level. This implies a rearrangement of the electronic structure between two colliding particles. Figure 2.1 is a summary of interactions between atomic hydrogen and the components of a tokamak plasma. Not all the interactions are significant in effecting the neutral hydrogen distribution however.

	Excitation	Ionization	Elastic Scattering	Charge Exchange
Photons	✓	✓		
Light Particles Electrons	✓	✓	✓	
Heavy Particles Protons	✓	✓	✓	✓
Impurity Ions	✓	✓	✓	✓

Figure 2.1 Possible interactions of hydrogen atoms with photons, electrons, and plasma ions.

The interaction of photons with neutrals is an ineffective method of altering the atomic state. In a tokamak plasma there are several sources of radiation; Bremsstrahlung, synchrotron emission and atomic line radiation. The Bremsstrahlung spectrum is primarily centered around the higher temperature ion energies ($T \geq 1$ keV) and the cross sections for photoionization or excitation of a hydrogen atom (ionization potential = 13.6 eV) by photons of this energy are very low. The synchrotron radiation levels are low in present tokamaks and in addition, the dominant spectrum is not hard enough ($E < 1$ eV) to cause appreciable ionization or excitation. Radiation arising from downward transitions in atomic levels within the plasma (line radiation) is the most likely source of photoionization or excitation; but even this contribution can be neglected when compared to electron impact reactions. The flux of photons ($E < 50$ eV) illuminating the vacuum wall region in the ST tokamak during the steady state part of the discharge has been determined by Hinnov [11] to be about 1×10^{17} cm^{-2} sec^{-1}. By way of comparison, the flux of electrons incident on a surface area from an isotropic Maxwellian distribution at a temperature of 10 eV (local density 10^{12} cm^{-3}) is about 4.4×10^{19} cm^{-2} sec^{-1}. The cross section for ionization and excitation by photons are additionally at least an order of magnitude less than their electron impact counterparts.

Of the interactions involving electrons and hydrogen neutrals in Figure 2.1 only the effect of ionization will be

non-negligible. The cross sections for excitation are comparable to those of ionization but the lifetime of allowed downward transition states is very short (10^{-8} sec)[16] in comparison to the time between collisions (10^{-4} sec). Only a small fraction of the bound electrons are excited to long lived metastable states with decay times on the order of 10^{-3} sec. Also, since only the small mass of the electron is involved in the collision process, the initial velocity vector of the neutral atom is unchanged.

The cross section for electron elastic scattering from the hydrogen neutral increases as energy decreases below the ionization potential to relatively large values ($\sim 10^{-16}$ cm^2). However, as in the case of excitation by electrons where little momentum is transferred to the massive neutral, the mechanism has little effect on the transport and can be neglected. Ionization is significant since it terminates the life of the neutral atom and is a source of plasma ions and electrons. In particular, electron impact ionization is important in a tokamak plasma because the ionization frequency ($N\langle\sigma v\rangle$, where N is the electron density and $\langle\sigma v\rangle$ is an averaged reaction rate) is large over the tokamak energy regime 10 eV < E < 10 keV. The energy dependence of the electron impact ionization cross section, σ_{ei}, is shown in Figure 2.2. The plot is drawn from a fit to experimental data given by Riviere [31] as

$$\sigma_{ei} = 3.52 \times 10^{-16} g(x) \ cm^2, \qquad (2.1)$$

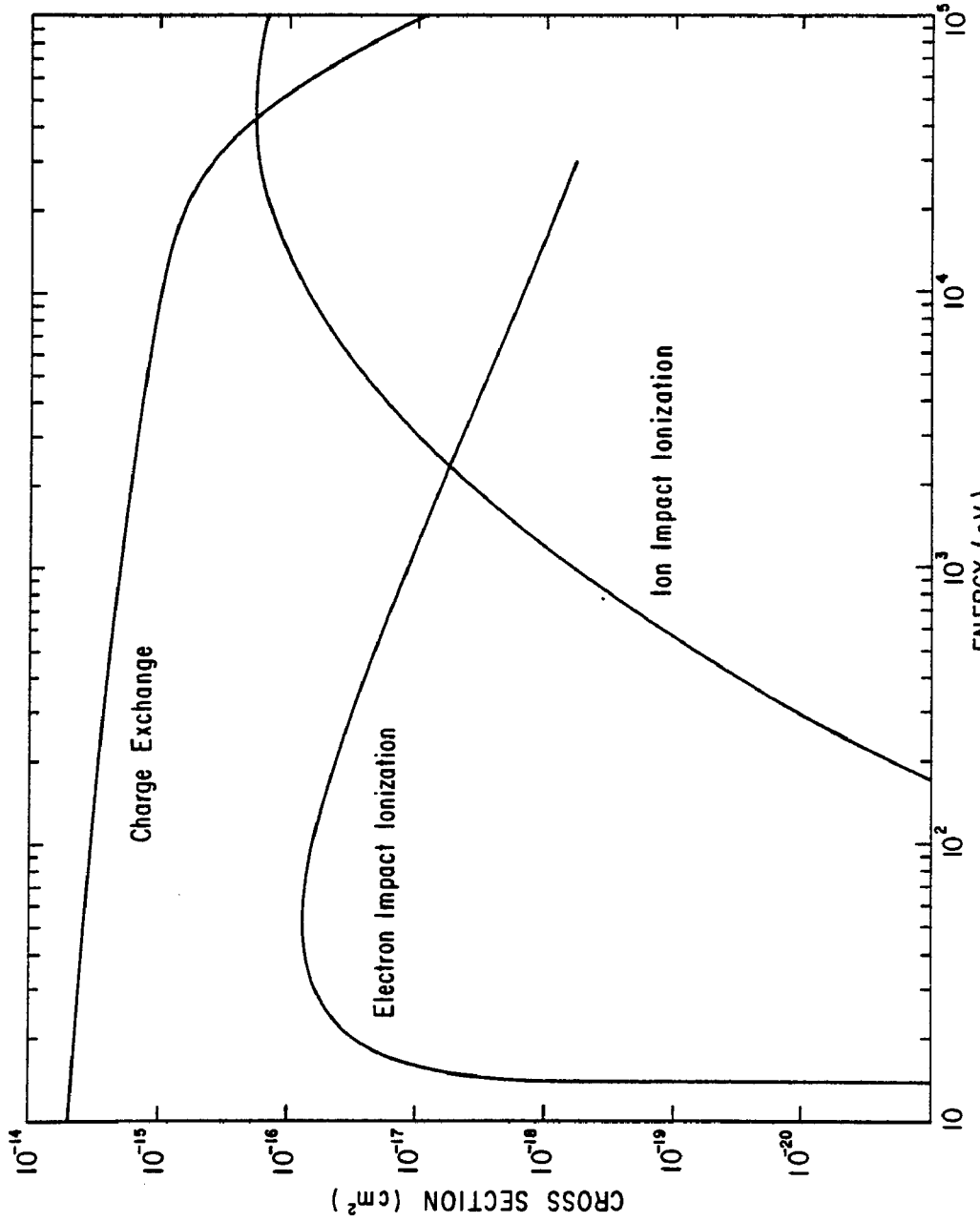

Figure 2.2 The neutral interaction cross sections used in the study as obtained from Riviere [31].

where

$$g(x) = \frac{1}{x}\left(\frac{x-1}{x+1}\right)^{\frac{3}{2}}\left[1 + \frac{2}{3}\left(1 - \frac{1}{2x}\right)\ln\left(2.7 + \sqrt{x-1}\right)\right] .$$

E is the electron energy in eV, and x is the ratio of E to the ionization potential (13.605 eV). Other fits to the same experimental data have been arrived at [32-34], but these differ from equation (2.1) by no more than 10-15% which will have a negligible effect on the transport calculations. The sensitivity to cross section values is discussed more fully in Chapter V.

As with electrons it is possible for the working gas ion component (we assume protons) of the plasma to cause atomic excitation or ionization of neutral hydrogen, or to be elastically scattered as indicated in Figure 2.1. The collision with heavy particles, though, is distinctive in two respects; the angular distribution of scattered projectiles is highly forward peaked and the energy regime where the cross sections are significant is much higher than electrons. The angular distribution of elastically scattered electrons is roughly isotropic (for E < 20 eV), but that of heavy projectiles is highly forward peaked (glancing angles). The result is that very little momentum is transferred to the target despite the large projectile mass. The energy regime where the interaction cross sections rise to a peak is also shifted to a much higher range (~ 50 keV as opposed to ~100 eV (electrons) for impact

ionization). This results from the cross sections being a function of the collision velocity rather than the energy variable. The cross sections for excitation by proton impact are comparable to those of ionization but because the majority of excited states decay quickly, as is the case with electron excitation, the effect can be neglected. The ionization rates due to proton impact are small in tokamak plasmas except for ion temperatures T > 5 keV. This can be seen from the decline of the proton impact ionization cross section (σ_{ii}) below E = 20 keV in Figure 2.2. The analytical fit used to generate σ_{ii} is taken from Riviere[31] as

$$\sigma_{ii} = \frac{3.6 \times 10^{-12}}{E} \log (.1666\, E) \,, \qquad (2.2)$$

$$E > 150 \text{ keV}$$

and

$$\log \sigma_{ii} = -.8712 (\log E)^2 + 8.156 (\log E) - 34.833 \,,$$

$$E < 150 \text{ keV}$$

where E is the proton energy in eV. Elastic scattering cross sections are sizable (~ 10^{-14} cm^2 below E = 100 eV) but the small amount of energy transfer (because of the

forward peaked scattering) minimizes the effect on the neutral transport. For this reason elastic scattering can be disregarded.

The charge exchange reaction can in at least one way be described as a virtual nonreaction, with dynamics similar to heavy particle elastic scattering. In the absence of external electromagnetic fields the incident projectile vector is effectively unchanged after the transfer of the small electron between ion and neutral. Likewise the target continues in its original direction with its initial velocity. Measurable deflection does occur from violent encounters in which a fast projectile passes very close to a target particle but these types of collisions are rare. Because of the change in identity between neutral and ion, however, the charge exchange event can also be regarded as a radical scattering process where the original neutral assumes the angular orientation and energy of the initial ion. Since the transport of the neutral species is of prime interest, the latter interpretation of charge exchange is adopted. The cross section (σ_{cx}) displayed in Figure 2.2 is plotted from the following expression by Riviere [31]:

$$\sigma_{cx} = \frac{.6937 \times 10^{-14} (1 - .155 \log E)^2}{1 + .1112 \times 10^{-14} E^{3.3}} \text{ cm}^2, \quad (2.3)$$

where E is the hydrogen atom energy in electron volts. For charge exchange between like species in consecutive charge states (termed a symmetric resonant reaction, e.g., $H^+ + H$) the cross sections are large and maximum for small impact energies ($E < 100$ eV). For charge charge exchange between unlike systems (asymmetric reactions) the cross sections maximum shifts to much higher energies depending on the difference in ionization potentials between the interacting species [16]. The symmetric charge exchange $H^+ + H \rightarrow H + H^+$ is seen to dominate over the ionization cross sections for $1 \text{ eV} < E < 20 \text{ keV}$ and is the primary means of background neutrals gaining energy and penetrating into a tokamak plasma core.

The impurity population of the plasma can potentially effect the neutral atom transport as indicated in Figure 2.1. The cross sections for ionization and excitation by impurities are predicted to be greater than the proton values by approximately a factor of Z^{+q} at equivalent velocities (Z is the impurity charge state and q=1.2-2.0) [35]. However this effect is minimized because the density of impurity ions is from one to three orders of magnitude less than the working gas ions [11]. This fact diminishes the importance of all impurity interactions on the neutral population and we neglect their effects. Little data exists on elastic scattering of impurity ions from atomic hydrogen but the results are not expected to be appreciably different than for protons. Because of the

asymmetry involved in the charge exchange of highly stripped impurities with the hydrogen neutral, the cross sections are not significantly large until impact energies are high (e.g., for $He^{++} + H \rightarrow He^{+}$ the peak is at approximately 30 keV). In a tokamak plasma therefore, the reaction can be safely neglected for low energy neutral analysis.

Just as in the case of neutron interactions with matter, long range coulomb collisions can be neglected because of the neutral charge state of the hydrogen atoms. Also since the relative population of neutrals in the plasma system is low it is possible to ignore the effect of neutral self collisions.

The dominant neutral-plasma reaction mechanisms can be categorized in a manner analogous to those of neutrons which was done in the previous section. This is summarized in Figure 2.3. The process of ionization removes particles from the neutral state and is in effect an absorber. Charge exchange (i.e., $H^{+} + H \rightarrow H + H^{+}$) effectively changes the directions and speed of the interacting neutral and is thus a scattering mechanism. There is no direct neutral analogue to fission or neutron producing reactions. Apart from source and boundary conditions then, the structure of the equation which governs neutron transport through matter should be equally adaptable to the neutral transport problem in tokamak plasmas.

	ABSORPTION	SCATTERING
NEUTRON (Nuclear Reactions)	Neutron Capture	Elastic and Inelastic Scattering
NEUTRAL (Atomic Reactions)	Electron Impact and Ion Impact Ionization	Charge Exchange

Figure 2.3 The analogous classification of neutron-neutral reactions.

The Neutron Transport Equation

If solution techniques developed for neutron transport are to be applied to neutral transport, the neutron transport equation, boundary conditions and source functions must be identical to those describing neutral behavior. These conditions are examined in the following section.

The Transport Equation

In the first section of this chapter it was demonstrated that the principal atomic reactions effecting neutral transport in a tokamak plasma could be considered analogous to the nuclear reactions effecting neutrons transported through matter. The well known neutron Boltzmann transport equation should therefore be applicable to the neutral transport problem. We have for the time independent case[36]

$$\underline{\Omega}\cdot\nabla\Phi + \sigma_a(\underline{r},E)\,\Phi(\underline{r},\underline{\Omega},E) = Q(\underline{r},\underline{\Omega},E) + \int_{E',\underline{\Omega}'} \Phi(\underline{r},\underline{\Omega}',E')\,\sigma_s(\underline{r},E')\,P(\underline{r};E'\underline{\Omega}'\rightarrow E\underline{\Omega})\,dE'\,d\Omega', \tag{2.4}$$

where $\Phi(\underline{r},\underline{\Omega},E)$ is the angular particle flux (cm^{-2} sec^{-1}), $\sigma_a(\underline{r},E)$ is the total macroscopic absorption cross section (cm^{-1}), $Q(\underline{r},\underline{\Omega},E)$ is the stationary particle source (cm^{-3} sec^{-1}) and the final term is the source due to a scattering process. Here $\sigma_s(\underline{r},E')$ is the macroscopic scattering cross section (cm^{-1}) and $P(\underline{r};E'\underline{\Omega}'\rightarrow E\underline{\Omega})$ is the

scattering probability function. (i.e. $P(\underline{r};E'\underline{\Omega}'\rightarrow E\underline{\Omega})d\Omega dE$ is the probability that if a particle of direction $\underline{\Omega}'$ and energy E' has a scattering collision, there will emerge the scattered particle in the direction interval $d\Omega$ about $\underline{\Omega}$ with energy in dE about E.) For example, in elastic neutron scattering (isotropic in the center of mass) from target atoms at rest (atomic number A), the function P is given by the conservation of momentum and kinetic energy [36] as

(2.5)

$$P(\underline{r};E'\underline{\Omega}'\rightarrow E\underline{\Omega}) = \begin{cases} \dfrac{1}{2\pi(1-\alpha)E'}\,\delta(\mu_0-S) & \alpha E' \le E \le E' \\ 0 & E > E' \text{ or } E < \alpha E', \end{cases}$$

where

$$S = \frac{1}{2}\left[(A+1)\sqrt{\frac{E}{E'}} - (A-1)\sqrt{\frac{E'}{E}}\right],$$

and

$$\alpha = \left[(A-1)/(A+1)\right]^2$$

$$\mu_0 = \underline{\Omega}\cdot\underline{\Omega}' \quad .$$

Equation (2.4) is a balance of particles in the volume of phase space ($\underline{r},\underline{\Omega},E$) of interest. The four terms represent, respectively, particle streaming (geometric losses), the total removal rate of particles from ($\underline{r},\underline{\Omega},E$) due to all reactions, an external source of particles, and the integrated contribution of scattering reactions. The cross sections (and scattering probability functions) appropriate for use in the Boltzmann equation vary from problem to problem. For the specific case of neutral atom transport these will be derived in Chapter III. Equation (2.4) is linear because neutron and neutral self collisions can be neglected. Also, the time dependence has been omitted. In neutron transport problems (e.g., shielding calculations, criticality searches, etc.) the material cross sections change very slowly in time and the steady state solution is of interest. In neutral transport problems significant changes in typical plasma temperature and density profiles (due to particle diffusion, heat conduction, ionization sources, etc.) are slow in comparison to the time required for passage of neutrals across the plasma volume (~ 10 μsec) [12]. In this case it is also sufficient to consider time independent (steady state) transport. Of final note is that in principle, equation (2.4) can be solved in any geometry provided the convective loss term ($\underline{\Omega}\cdot\nabla\Phi$) and the element of solid angle $d\Omega$ are known.

Boundary Conditions

Boundary conditions that determine an unique solution to equation (2.4) are applied at material interfaces. In neutron analysis these may be between solid materials or at the edge of a system where an effective vacuum occurs. The interface condition states that the number of neutrons in a packet is not changed by crossing a physical interface. This means that the neutron angular density must be continuous in $\underline{r}$ as the interface is crossed. If however a neutron source or a strong absorber is to be modelled at a boundary, a suitable "discontinuity" condition can also be derived.

Neutrons are frequently modelled to leave a system and not return; so called vacuum boundary conditions are applied in this case. This simply states that the angular density of incoming neutrons must vanish at the boundary (in the absence of an external source). In actuality a neutron leaving the system (e.g., into the air surrounding a reactor) will have a finite but small probability of returning; hence, the vacuum boundary condition is an idealization.

In a practical MGDO transport code a number of standard boundary conditions are available. The continuity condition between material interfaces is assumed to apply without specification. At the system boundaries the vacuum (nonreentrant flux) condition can be used. Also in the consideration of problems where symmetry can be invoked,

specular reflecting and periodic boundary conditions can conveniently reduce the physical size of the problem to be analyzed. If the reflective properties of a boundary material are known, the material can be replaced with an albedo boundary condition that will return a portion of the outgoing flux into the system isotropically.

The mean free path of absorption for neutral atoms in a plasma is comparable to that of neutrons through some materials. At a material boundary, however, the bulky neutral atoms ($E < 10$ keV) have many collisions in a short distance ($< 10^{-6}$ cm) before either coming to rest in the material lattice or before being backscattered (with a fraction of their original energy) into the plasma again. The latter process is referred to as neutral reflection. Few experimental data exist for the measurement of the fraction of the number of particles reflected (R_N, particle reflection coefficient) or the fraction of the initial energy reflected (R_E, energy reflection coefficient) for materials that are likely to be encountered as vacuum first walls in fusion devices. Computer calculations [37] however show that the reflection coefficients are dependent on the initial energy and angular orientation of the incident neutral. Typical results are shown in Table II.1. Higher energy neutrals penetrate further into the solid and hence have a smaller probability of being reflected. In contrast grazing incidence neutrals have collision paths close to the surface where there is a high probability that a scattering

		50 eV*	500 eV*	5 keV†
R_N , Particle Reflection Coefficient	0°	.56	.36	.10
	60°	.90	.60	
	90°	1	1	
R_E , Energy Reflection Coefficient	0°	.40	.20	.05
	60°	.80	.40	
	90°	1	1	

* Robinson (Calculated on Cu) [37]

† Behrisch (on Fe) [49]

Table II.1 Reflection coefficients for hydrogen atoms incident on metallic surfaces.

will lead to emission from the metal. Because of the randomization involved in the collision process the angular distribution of emerging neutrals is probably not governed by a purely specular law.

The transfer of energy from the impinging neutral to the metal lattice can cause the knock-on atoms to be released from the surface. This process is referred to as sputtering and was seen to be an important result of the neutral population transport in Chapter I. Incident neutrals can also cause the release of atoms and molecules adsorbed on the surface due to the energy transfer process (impact desorption).

The reflection mechanism of neutrals at a material surface becomes a true boundary condition. However, it will be recalled that the options available from a standard MGDO transport code are not detailed enough to model the exact case. Perfectly absorbing and perfectly reflecting boundary conditions are available, though, which will represent the limiting effects on the transport calculation. The need for considering realistic boundary conditions is somewhat debatable as the effects (versus a vacuum case) are expected to be only on the order of ~20-30% [7,38].

Source Conditions

In practical neutron analysis external sources are of two types: boundary or volumetric. Examples of boundary sources include fusion (14 MeV) neutrons incident on a blanket structure, or neutrons from an adjacent fission

region impinging on a shield configuration. If the plasma producing the fusion neutrons were to be included in the analysis, then this would constitute a volumetric source. The neutrons produced from the $Be^{9}(\alpha,n)C^{12}$ startup reaction in a fission reactor must also be modelled in the latter category. The spatial source of fission neutrons is considered separately. What is common to most neutron sources is that they are of high energy in relation to that of the bulk neutron population (neutrons generally slowdown).

It is possible to model both types of neutron sources in present day MGDO codes. In the case of a boundary source the incoming angular flux can be specified at the outer boundary as a function of angle and energy. For a volumetric source the number of neutrons isotropically produced per cm^3 per second as a function of energy and position is given.

The source of background neutral atoms during the steady state operation of a tokamak is situated at the edge region of the plasma. Molecular hydrogen which has been outgassed from the vacuum wall and desorbed surface hydrogen move into the edge plasma with energies on the order of .1 eV. The transition into a fully ionized region is probably gradual (outside the plasma limiter in a tokamak) but the first plasma encountered by incident neutrals is typically at a temperature of 20 eV and density 10^{12} cm^{-3}. Since this is the case, the volumetric recombination of protons and

electrons to the neutral state is highly unlikely. (The temperature below which recombination becomes significant is on the order of 1 eV.)

It is possible for the incoming neutral molecule to experience a number of interaction processes. The principle reaction mechanisms are described below:

(2.6)

$$H_2 + e^- \rightarrow H_2^+ + 2e^- \begin{cases} \rightarrow H^+ + H + 2e^- & \text{Dissociative Ionization} \\ \rightarrow H + H + e^- & \text{Dissociative Recombination} \\ \rightarrow H^+ + H^+ + 3e^- & \end{cases}$$

$$H_2 + e^- \rightarrow H + H + e^- \qquad \text{One Step Dissociation}$$

$$H_2 + e^- \rightarrow H_2^* + e^- \rightarrow H + H + e^- + h\nu \quad .$$

All the reactions are governed by the Franck-Condon Principle [16] which states that in the dissociation of molecules induced by electronic transitions, the excess energy of excitation will be shared between the final reaction products. For the cases cited above, this results in products with kinetic energies on the order of several electron volts. For electron temperatures greater than 5 eV, dissociative ionization is dominant [15]. The mean

free path for production of neutral hydrogen atoms by this process in the first plasma encountered by neutral molecules is on the order of several centimeters. The neutrals have a range of energies but this is centered closely around 3 eV. The source of background neutrals is thus at a low energy relative to the bulk neutrals in the plasma. This is the opposite circumstance from that encountered in typical neutron transport problems.

The concept of puffing hydrogen gas into a tokamak [17] does not change the fundamental process of neutral atom formation. However, the density of initial gas is much higher than that expected from pure desorption. It is also possible that the source geometry may be different (localized as opposed to a uniform desorption source).

The initial background hydrogen atom neutrals in a tokamak can thus be modelled adequately by a volumetric source over a thin region of plasma near the outer edge. We have seen that the source options available in a MGDO transport code are sufficient for this purpose.

Methods for Solution

The neutron and neutral formulations of the transport equation, with associated boundary conditions and sources, have been shown to be analogous in the previous section. We mention here briefly the neutron solution techniques which are therefore applicable to the neutral transport problem.

Many analytic methods have been used to solve specialized cases in neutron transport [36,39]. For

one-speed, one-dimensional problems, separation of variables and spherical harmonics methods are available. If scattering is isotropic and absorption is small, the diffusion approximation becomes valid. Using the solution to a simplified neutron transport problem, Zubarev and Klimov [1] were able to approximate the neutral atom profile in a plasma. The difficulty with all analytic treatments, however, is that not enough detail can be included (particularly for the energy variable) to consider even moderately realistic problems. As a consequence most analysis is given over to the greater scope of the computer.

The numerical approaches [36,40] can be classified as either variable or stochastic. The variable method will either discretize or approximate in modal expansion the variable functions (angular flux, scattering function, etc.) of the Boltzmann equation. A coupled set of algebraic equations usually results which can be solved iteratively. The stochastic method is based on the random walk process where the stored set of particle histories can be used to statistically generate the results of interest (densities, energy spectra, etc.).

For the variable method there is the question of which variables are to be discretized and which are to be treated in modal fashion. A number of combinations have been tried with varying success in a wide range of problems. Notable among these is the multigroup P_L method [36] where the energy range is broken up into finite discrete groups and

the angular flux is expanded in spherical harmonic functions (angular variable). Another extremely versatile approach is to abandon the use of modal functions altogether and to take all variables to be discrete rather than continuous. Multigroup discrete ordinates (MGDO) methods are the result. Instead of an angular expansion the angular distribution of the neutron flux is evaluated in a number of discrete directions. Finite energy groups are again used and the spatial varable can be treated by either finite element or finite difference techniques. The versatility of the MGDO method has led to the development of a stock of transport codes [41] which are both convenient and reliable. One of these, ANISN [3], is used to calculate neutral atom transport in the present study.

Stochastic methods are commonly referred to as Monte Carlo methods [36,40]. The history of individual particles is traced and recorded as collisions are made and boundaries crossed in the medium. Statistical detectors sense the presence of particles and measurable quantities (densities, reaction rates, etc.) can be calculated. Monte Carlo methods can be more time consuming than variable treatments but have the advantage of being able to consider more complex geometries [36]. It is also possible to model non-standard source configurations and boundary conditions.

CHAPTER III

THE MULTIGROUP DISCRETE ORDINATES FORMULATION

The Neutral Transport Equation

It was noted in Chapter II that the linear Boltzmann equation (2.4) could be used for both neutron and neutral transport provided that the appropriate cross sections (and scattering probability function) were considered. These quantities are formulated for neutral transport in the present section.

The Consideration of Target Motion

It is recalled that the general form of the Boltzmann equation for neutron transport is (from equation (2.4))

$$\underline{\Omega}\cdot\nabla\Phi + \sigma_a(\underline{r},E)\,\Phi(\underline{r},\underline{\Omega},E) = Q(\underline{r},\underline{\Omega},E) \qquad (3.1)$$

$$+ \int_{E',\underline{\Omega}'} \Phi(\underline{r},\underline{\Omega}',E')\,\sigma_s(\underline{r},E')\,P(\underline{r};E'\underline{\Omega}'\rightarrow E\,\underline{\Omega})\,dE'\,d\Omega' .$$

In its present form the motion of the target nuclei has been neglected and thus reaction rates are a function of the neutron energy only. This approximation is common when the kinetic energy of the neutrons is much greater than that of the lattice target nuclei. (i.e., for the transport of

fast neutrons slowing down to thermal energies.) Background neutrals, on the other hand, are introduced into the plasma system with energies much less than that of the target plasma ions or electrons, so the target velocities cannot be neglected in the calculation of reaction rates. Due to the dominance of the charge exchange mechanism the neutrals that penetrate into the plasma acquire energies comparable to those of the surrounding ions. Thus, throughout the plasma, it is necessary to consider target (ion or electron) motion in determining neutral interaction rates.

Target motion is taken into account by averaging over the energy and direction variables (equivalent to the velocity vector) of the target distribution functions to define new "effective" interaction cross sections. For the total absorption cross section:

(3.2)

$$v\,\sigma_a^{eff}(\underline{r},\underline{\Omega},E) = \int_{E',\underline{\Omega}'} N_i(\underline{r})\, f_i(\underline{r},\underline{\Omega}',E')\,|\underline{v}-\underline{v}'|\,\sigma_{ii}(|\underline{v}-\underline{v}'|)\,dE'd\Omega'$$

$$+ \int_{E',\underline{\Omega}'} N_e(\underline{r})\, f_e(\underline{r},\underline{\Omega}',E')\,|\underline{v}-\underline{v}'|\,\sigma_{ei}(|\underline{v}-\underline{v}'|)\,dE'd\Omega'$$

$$+ \int_{E',\underline{\Omega}'} N_i(\underline{r})\, f_i(\underline{r},\underline{\Omega}',E')\,|\underline{v}-\underline{v}'|\,\sigma_{ex}(|\underline{v}-\underline{v}'|)\,dE'd\Omega' ,$$

where v is the neutral particle velocity ($v=\sqrt{\frac{2E}{m_n}}$, $m_n \equiv$ neutral mass), $N_i(N_e)$ is the ion (electron) density (cm^{-3}) and $f_i(f_e)$ is the ion (electron) distribution

function. The target velocity v' is calculated as $v' = \sqrt{\frac{2E'}{m_{i,e}}}$ where the mass, $m_{i,e}$, refers to either ions or electrons. The microscopic cross sections σ_{ii}, σ_{ei}, and σ_{cx} (cm^2) represent ion impact ionization, electron impact ionization and charge exchange reactions respectively. We have assumed that f_i and f_e are normalized so that

$$\int_{E',\underline{\Omega}'} f_{i,e}(\underline{\Omega}', E')\, dE'\, d\underline{\Omega}' = 1 \,. \tag{3.3}$$

The integrals on the right hand side of equation (3.2) are seen to be the average reaction rates ($\langle\sigma v\rangle$) between a beam of monoenergetic test particles with a distributed group of targets characterized by the function f. The formal definition of the effective reaction cross section σ_a^{eff} has picked up an angular dependence because of the general anisotropic nature of the target distribution.

For scattering from a moving target an effective scattering kernel K_s^{eff} is defined (similar to equation 3.2) which replaces its no target motion counterpart in equation (3.1):

$$v'\, \sigma_s^{eff}(\underline{r}, \underline{\Omega}', E')\, P^{eff}(\underline{r}; E'\underline{\Omega}' \rightarrow E\underline{\Omega})$$

$$= v'\, K_s^{eff}(\underline{r}; E'\underline{\Omega}' \rightarrow E\underline{\Omega}) \,, \tag{3.4a}$$

$$= \int_{E_T, \Omega_T} N_i(\underline{r})\, f_i(\underline{r}, \underline{\Omega}_T, E_T)\, |\underline{v}' - \underline{v}_T|\, \sigma_{cx}(|\underline{v}' - \underline{v}_T|) \times P_{\underline{v}_T}(\underline{r}; E'\underline{\Omega}' \rightarrow E\underline{\Omega})\, dE_T\, d\Omega_T . \tag{3.4b}$$

Here we have had to introduce the target velocity coordinates* ($v_T = \sqrt{\frac{2E_T}{m_T}}$) as a third set of variables to designate that a target at E_T, $\underline{\Omega}_T$ has scattered an initial neutral with $E', \underline{\Omega}'$ into a final state $E, \underline{\Omega}$. This is characterized by $P_{\underline{v}_T}(\underline{r}; E'\underline{\Omega}' \rightarrow E, \underline{\Omega})$ which is the probability that a neutral with initial energy E' and direction $\underline{\Omega}'$ interacting (by charge exchange) with a target ion with velocity vector $\underline{v}_T$ will be scattered to final coordinates $E, \underline{\Omega}$.

With the effects of target motion included, the Boltzmann equation can be re-written with the aid of the definition in equations (3.2) and (3.4) as

$$\underline{\Omega} \cdot \nabla \Phi + \sigma_a^{eff}(\underline{r}, \underline{\Omega}, E)\, \Phi(\underline{r}, \underline{\Omega}, E) = Q(\underline{r}, \underline{\Omega}, E) + \int_{E', \Omega'} \Phi(\underline{r}, \underline{\Omega}', E')\, K_s^{eff}(\underline{r}; E'\underline{\Omega}' \rightarrow E\underline{\Omega})\, dE'\, d\Omega' . \tag{3.5}$$

*Note that in the previous expression (3.2) the primed variables designated the target species.

The formulation of equation (3.4) is similar to that of Blackshaw and Murray [42]. The authors proceed to derive the scattering probability function for elastic scattering (isotropic in the center of mass) of low energy neutrons in a Maxwellian monatomic gas. An expression for the scattering kernel is then arrived at which is a function of an arbitrary form of the reaction cross section. In the present study it will be necessary to determine the scattering probability $P_{\underline{v}_T}$ for the charge exchange event and evaluate the integral of equation (3.4) in an analogous manner.

Derivation of the Charge Exchange Scattering Probability and Scattering Kernel

The collisional dynamics of charge exchange presents a particularly simple picture. Charge exchange may be viewed as a scattering process with a change of identity between neutral and ion but with no appreciable transfer of energy or momentum [16]. The electron exchanged between neutral and ion does little to alter the original velocity vectors of the incident projectiles. Its effects can therefore be neglected. The "fly by" character of the charge exchange reaction is illustrated in Figure 3.1. For convenience, a monoenergetic beam of neutrals (current in neutrals/sec) is incident on a beam of ions (ions/sec). The initial neutrals have energy E' and orientation $\underline{\Omega}'$ (associated with the vector $\underline{v}'$). A linear density n'(neutrals/cm) is assigned to the current in the

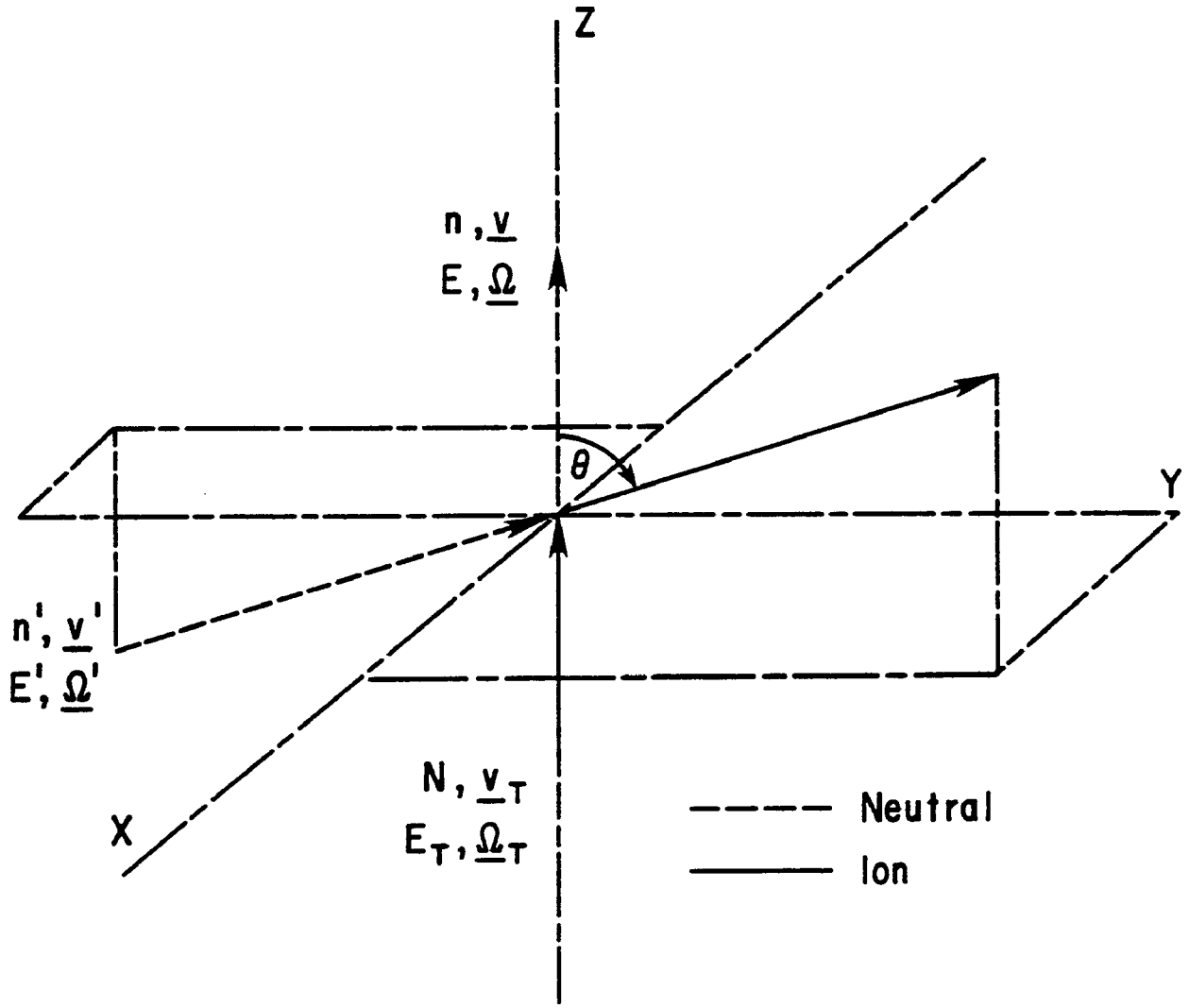

Figure 3.1 Schematic representation of a neutral-ion collision, at the origin of the coordinate system, resulting in charge exchange.

monoenergetic neutral beam (i.e., current = n'v'). The initial colliding ions likewise have velocity vector $\underline{v}_T$ (with energy E_T and orientation $\underline{\Omega}_T$, along the Z axis) and a linear density N. From the collision point of the two beams (at the origin) a beam of charge exchange neutrals is shown to emerge with density n, velocity vector $\underline{v}$, energy E and orientation $\underline{\Omega}$ (along the Z axis). Thus, if a charge exchange event occurs, then the final charge exchange neutral velocity vector $\underline{v}$ must be identical to the initial ion velocity vector $\underline{v}_T$. That is, $\underline{v} = \underline{v}_T$. In terms of the energy variables, the only resulting energy and direction a charge exchange neutral may have in interacting with an ion of energy E_T with direction $\underline{\Omega}_T$ is the same E_T and $\underline{\Omega}_T$. Hence the probability, $P_{\underline{v}_T}(\underline{r}; E'\underline{\Omega}' \rightarrow E\underline{\Omega})dEd\Omega$, that a neutral with initial energy E' and direction $\underline{\Omega}'$ which charge exchange with a target ion with E_T, $\underline{\Omega}_T$ will be scattered into dE about E and $d\Omega$ about $\underline{\Omega}$ is

$$P_{\underline{v}_T}(\underline{r}; E'\underline{\Omega}' \rightarrow E\underline{\Omega})\, dE\, d\Omega = \delta(E-E_T)\, \delta_2(\underline{\Omega}\cdot\underline{\Omega}_T - 1)\, dE\, d\Omega, \quad (3.6)$$

where δ_2 is an angular delta function. The validity of equation (3.6) can be demonstrated by integrating the probability function over a small ΔE and $\Delta\Omega$ giving

$$\int_{\Delta E, \Delta\underline{\Omega}} P_{\underline{v}_T}(\underline{r}; E'\underline{\Omega}' \rightarrow E\underline{\Omega})\, dE\, d\Omega \quad (3.7)$$

$$= \int_{\Delta E, \Delta\underline{\Omega}} \delta(E-E_T)\, \delta_2(\underline{\Omega}\cdot\underline{\Omega}_T - 1)\, dE\, d\Omega = 1,$$

provided that E_T is in ΔE and $\underline{\Omega}_T$ is in $\Delta\Omega$; the integral vanishes for E_T or $\underline{\Omega}_T$ outside of the range of integration. These were the properties of the charge exchange reaction that arose from the original physical model; namely, that a scattering event could occur only if the final interacting neutral velocity $\underline{v}$ was identical to the initial ion vector $\underline{v}_T$. Thus, equation (3.6) can be regarded as an accurate representation of the charge exchange scattering probability function.

Note that although charge exchange neutrals have the same velocity vector as the incident ions, the current of charge exchange neutrals is not equal to the current of the incident ions. (i.e., in Figure 3.1 notation; $\underline{v} = \underline{v}_T$ but $nv \neq N v_T$.) That is, not all ions in the initial beam become neutralized; there will be competing atomic reactions and some ions will not interact at all. The current of charge exchange neutrals will be proportional to the linear density of incident neutrals, the linear density of incident ions, the relative velocity of approach and a conventional collision cross section;

$$nv \propto n' N \, |\underline{v}' - \underline{v}_T| \, \sigma_{ex}(|\underline{v}' - \underline{v}_T|) \tag{3.8}$$

$$\text{where} \quad |\underline{v}' - \underline{v}_T| = \left[v'^2 + v_T^2 - 2 v' v_T \cos\theta \right]^{\frac{1}{2}}.$$

From equation (3.8) it can be seen that for a given set of initial particle densities and speeds, the charge exchange neutral current is a function of the relative orientation of the beams through the relative velocity. This leads to the observation that for ion beams of equal strength intersecting at a common point with a neutral beam, the resulting source of charge exchange neutrals will not be isotropic. The generalization is that a point source of charge exchange neutrals resulting from the interaction of a neutral beam with any isotropic ion distribution will not, in general, be isotropic.

With the formulation of the charge exchange scattering function completed, equation (3.6) can be substituted into equation (3.4(b)) to evaluate the scattering kernel K_s^{eff}. We have

$$K_s^{eff}(\underline{r}; E'\underline{\Omega}' \rightarrow E\underline{\Omega}) \tag{3.9}$$

$$= \frac{1}{v'} \int_{E_T, \underline{\Omega}_T} N_i(\underline{r})\, f_i(\underline{r}, \underline{\Omega}_T, E_T)\, |\underline{v}' - \underline{v}_T|\, \sigma_{cx}(|\underline{v}' - \underline{v}_T|) \times \delta(E - E_T)\, \delta_2(\underline{\Omega} \cdot \underline{\Omega}_T - 1)\, dE_T\, d\Omega_T.$$

The integration over the target variables yields:

$$K_s^{eff}(\underline{r}; E'\underline{\Omega}' \rightarrow E\underline{\Omega}) = \frac{N_i(\underline{r})}{v'} f_i(\underline{r}, \underline{\Omega}, E)\, |\underline{v}' - \underline{v}|\, \sigma_{cx}(|\underline{v}' - \underline{v}|). \tag{3.10}$$

As a check on equation (3.10) it can now be seen that the charge exchange term of σ_a^{eff} (equation (3.2)) can be rewritten using the effective scattering kernel as

$$\sigma_a^{eff}(\underline{r},\underline{\Omega},E) = \frac{1}{v}\int_{E',\underline{\Omega}'} N_i(\underline{r})\, f_i(\underline{r},\underline{\Omega}',E')\,|\underline{v}-\underline{v}'|\,\sigma_{cx}(|\underline{v}-\underline{v}'|)\,dE'\,d\Omega'$$

$$= \int_{E',\underline{\Omega}'} K_s^{eff}(\underline{r};\, E\,\underline{\Omega}\rightarrow E'\underline{\Omega}')\,dE'\,d\Omega' \quad . \tag{3.11}$$

Thus, the derivation of equation (3.10) for the in-scattering charge exchange contribution to the Boltzmann equation, is consistent with the outscattering (absorption) expression arrived at previously.

For the analysis of tokamak systems it is frequently assumed that the plasma ions and electrons are in local thermodynamic equilibrium [43]. This implies that the plasma distribution functions are Maxwellian and are thus isotropic. For the remainder of the study we assume isotropy with the introduction of the distribution functions

$$f_e(\underline{r},\underline{\Omega},E) = \frac{1}{4\pi}\, h_e(\underline{r},E) \quad , \tag{3.12}$$

and

$$f_i(\underline{r},\underline{\Omega},E) = \frac{1}{4\pi} h_i(\underline{r},E) . \qquad (3.12)$$

The normalization is such that

$$\int_0^\infty h_{i,e}(E)\, dE = 1 . \qquad (3.13)$$

The expression for the effective absorption cross section (equation (3.2)) can now be written as

(3.14)

$$\sigma_a^{eff}(\underline{r},E) = \frac{1}{v}\int_{E',\underline{\Omega}'} N_i(\underline{r})\, h_i(\underline{r},E')\, |\underline{v}-\underline{v}'|\, \sigma_{ii}(|\underline{v}-\underline{v}'|)\, \frac{dE'd\Omega'}{4\pi}$$

$$+ \frac{1}{v}\int_{E',\underline{\Omega}'} N_e(\underline{r})\, h_e(\underline{r},E')\, |\underline{v}-\underline{v}'|\, \sigma_{ei}(|\underline{v}-\underline{v}'|)\, \frac{dE'd\Omega'}{4\pi}$$

$$+ \frac{1}{v}\int_{E',\underline{\Omega}'} N_i(\underline{r})\, h_i(\underline{r},E')\, |\underline{v}-\underline{v}'|\, \sigma_{ex}(|\underline{v}-\underline{v}'|)\, \frac{dE'd\Omega'}{4\pi} .$$

The noticeable effect of the restriction to isotropic distribution functions is that σ_a^{eff} is no longer dependent on the angular variable $\underline{\Omega}$. It turns out that this is a necessary constraint for the operation of most present day MGDO transport codes and so is indeed fortuitous. If anisotropic distributions were considered (as must be done

for plasma mirror configurations [44,45]) the effect would be to slightly alter reaction rates and to enhance charge exchange neutral transport in preferential directions along the lines of streaming ions.

Equation (3.10) for the effective scattering kernel can likewise be rewritten giving

(3.15)

$$K_s^{eff}(\underline{r};E'\underline{\Omega}'\rightarrow E\underline{\Omega}) = \frac{N_i(\underline{r})}{4\pi v'} h_i(\underline{r},E)\,|\underline{v}'-\underline{v}|\,\sigma_{cx}(|\underline{v}'-\underline{v}|).$$

It is important to point out that K_s^{eff} is now not dependent explicitly on the vectors $\underline{\Omega}$ and $\underline{\Omega}'$ but only on their relative orientation through the relative velocity term. (i.e.,

$$|\underline{v}'-\underline{v}| = \left[v'^2 + v^2 - 2v'v\mu_0\right]^{\frac{1}{2}}, \qquad (3.16)$$

where

$$\mu_0 = \underline{\Omega}\cdot\underline{\Omega}'.$$

Keeping in mind the definitions of equations (3.14) and (3.15), the neutral Boltzmann equation (3.5) can now be written as

$$\underline{\Omega}\cdot\nabla\Phi + \sigma_a^{eff}(\underline{r},E)\,\Phi(\underline{r},\underline{\Omega},E) = Q(\underline{r},\underline{\Omega},E) \tag{3.17}$$

$$+ \int_{E',\underline{\Omega}'} \Phi(\underline{r},\underline{\Omega}',E')\,K_s^{eff}(\underline{r};E'\underline{\Omega}'\rightarrow E\underline{\Omega})\,dE'd\underline{\Omega}'.$$

The Neutral Multigroup Equations

The Legendre Expansion of the Scattering Kernel

It is known that a MGDO transport code will be used to solve the neutral Boltzmann equation (3.17). In neutron elastic scattering (with stationary targets) the scattering kernel (as seen from equation (2.5)) is a function only of the relative angle of scatter, $\mu_o = \underline{\Omega}\cdot\underline{\Omega}'$, and not of the explicit orientations of $\underline{\Omega}$ and $\underline{\Omega}'$. Traditionally, the MGDO computational solution is simplified with the use of this fact by expansion of the scattering kernel in Legendre polynominals of argument μ_o. The derivation of the charge exchange scattering kernel for isotropic targets (equation (3.15)) has also revealed that it is a function only of the scattering angle μ_o. For its use in a MGDO code, therefore, the charge exchange scattering kernel is expanded in the usual manner. This is done by defining the expansion

$$K_s^{eff}(\underline{r};E'\underline{\Omega}'\rightarrow E\underline{\Omega}) = \sum_{l=0}^{\infty}\frac{1}{4\pi}K_{sl}(\underline{r};E'\rightarrow E)\,P_l(\mu_o), \tag{3.18}$$

where

$$K_{s\ell}(\underline{r};E'\to E) = 2\pi(2\ell+1)\int_{-1}^{1} K_s^{eff}(\underline{r};E'\underline{\Omega}'\to E\underline{\Omega})\,P_\ell(\mu_0)\,d\mu_0 . \tag{3.19}$$

The significance of the expansion technique used by MGDO methods for anisotropic scattering kernels (and in particular for charge exchange) will be discussed in the following section.

The Legendre expansion (equation (3.18)) is substituted into the Boltzmann equation (3.17) to yield

$$\begin{aligned}\underline{\Omega}\cdot\nabla\Phi + \sigma_a^{eff}(\underline{r},E)\,\Phi(\underline{r},\underline{\Omega},E) &= Q(\underline{r},\underline{\Omega},E)\\ &+\sum_{\ell=0}^{\infty}\int_{E'} K_{s\ell}(\underline{r};E'\to E)\,\varphi_\ell(\underline{r},\underline{\Omega},E')\,dE',\end{aligned} \tag{3.20}$$

where

$$\varphi_\ell(\underline{r},\underline{\Omega},E') = \frac{1}{4\pi}\int_{\underline{\Omega}'}\Phi(\underline{r},\underline{\Omega}',E')\,P_\ell(\mu_0)\,d\underline{\Omega}', \tag{3.21}$$

is the Legendre flux moment.

The Multigroup Treatment of the Energy Variable

Attention is now turned to the treatment of the energy variable by conventional multigroup methods. Equation

(3.20) is integrated over a finite band of energies between the group limits $E_{g+1} \leq E \leq E_g$ so that

$$\underline{\Omega} \cdot \int_{E_{g+1}}^{E_g} \nabla \Phi(\underline{r}, \underline{\Omega}, E)\, dE + \int_{E_{g+1}}^{E_g} \sigma_a^{eff}(\underline{r}, E)\, \Phi(\underline{r}, \underline{\Omega}, E)\, dE$$

$$= \int_{E_{g+1}}^{E_g} Q(\underline{r}, \underline{\Omega}, E)\, dE \qquad (3.22)$$

$$+ \sum_{l=0}^{\infty} \int_{E_{g+1}}^{E_g} \sum_{h=1}^{G} \int_{E_{h+1}}^{E_h} K_{s,l}(\underline{r}; E' \to E)\, \Phi_l(\underline{r}, \underline{\Omega}, E')\, dE' dE,$$

where the original integral over E' has been rearranged as

$$\int_{E'} dE' = \sum_{h=1}^{G} \int_{E_{h+1}}^{E_h} dE' . \qquad (3.23)$$

G is the number of groups spanning the energy range E' or E. It is convenient to rewrite equation (3.22) by first defining the following:

$$\Phi_g(\underline{r}, \underline{\Omega}) = \int_{E_{g+1}}^{E_g} \Phi(\underline{r}, \underline{\Omega}, E)\, dE , \qquad (3.24)$$

$$\sigma_{a,g}(\underline{r},\underline{\Omega}) = \int_{E_{g+1}}^{E_g} \sigma_a^{eff}(\underline{r},E)\ \Phi(\underline{r},\underline{\Omega},E)\,dE \Big/ \Phi_g(\underline{r},\underline{\Omega}), \tag{3.25}$$

$$K_{s\ell}^{h\to g}(\underline{r},\underline{\Omega}) = \int_{E_{h+1}}^{E_h} \varphi_\ell(\underline{r},\underline{\Omega},E') \times \int_{E_{g+1}}^{E_g} K_{s\ell}(\underline{r};E'\to E)\,dE'dE \Big/ \varphi_{\ell,h}(\underline{r},\underline{\Omega}), \tag{3.26}$$

$$\varphi_{\ell,h}(\underline{r},\underline{\Omega}) = \int_{E_{h+1}}^{E_h} \varphi_\ell(\underline{r},\underline{\Omega},E')\,dE', \tag{3.27}$$

$$Q_g(\underline{r},\underline{\Omega}) = \int_{E_{g+1}}^{E_g} Q(\underline{r},\underline{\Omega},E)\,dE. \tag{3.28}$$

Equation (3.22) now becomes

$$\underline{\Omega}\cdot\nabla\,\Phi_g(\underline{r},\underline{\Omega}) + \sigma_{a,g}(\underline{r},\underline{\Omega})\,\Phi_g(\underline{r},\underline{\Omega}) = Q_g(\underline{r},\underline{\Omega}) + \sum_{\ell=0}^{\infty}\sum_{h=1}^{G} K_{s\ell}^{h\to g}(\underline{r},\underline{\Omega})\,\varphi_{\ell,h}(\underline{r},\underline{\Omega}), \tag{3.29}$$

which will be known as the neutral multigroup equation. Equation (3.29) is the formal representation of the transport equation that is solved in modern MGDO codes.

Multigroup Discrete Ordinates Methods

The advantage of using MGDO methods for neutral transport analysis will be discussed in Chapter V. For this purpose it is necessary to present additional background information on the solution technique. The use of MGDO methods for neutron transport analysis is well documented [36,46] and so only a cursory discussion is given here.

The MGDO method of solving the Boltzmann transport equation (3.1) is based on the discretization of all the independent variables; space $\underline{r}$, direction $\underline{\Omega}$, and energy E. Differentials are approximated by finite differences and integrals by weighted sums to yield a set of coupled (in energy and angle) algebraic equations suitable for an interative solution on the computer. This widely used and highly successful class of transport equation solvers was designed to yield accurate results for deep neutron penetration problems, even where pronounced anisotropic scattering and energy dependent cross sections were encountered. In principle the only limit on accuracy is the size and speed of the computer which restricts the fineness of the space, angle and energy meshes.

A feature of many MGDO methods is the ability to treat the anisotropic nature of the scattering kernel. This is necessary for neutron elastic scattering (equation (2.5)) as well as for the charge exchange process (equation (3.15)). The charge exchange kernel is anisotropic in the sense that

the product $|\underline{v}-\underline{v}'|\ \sigma_{cx}\ (|\underline{v}-\underline{v}'|)$ depends upon the relative orientation of the initial and final neutral velocity vectors $\underline{v}$ and $\underline{v}'$. For example, when v~v', collisions that are head on occur at a greater frequency than those for which $\underline{v}$ and $\underline{v}'$ are in the same direction. The situation is reversed for relative energies greater than about 10 keV because the charge exchange cross section drops off much more rapidly than $1/|\underline{v}-\underline{v}'|$.

The usual treatment (discussed in the previous section) is to expand the scattering kernel in a series of Legendre polynominals of the angle μ_o (equation (3.18)). In the actual implementation of the expansion, however, an approximation to the infinite series is made by truncating after a finite (L) number of terms (the P_L scattering approximation). Even for highly anisotropic neutron scattering the approximation appears to be accurate with relatively few terms [47]. Qualitatively both $K_{s\ell}$ and ϕ_ℓ of equation (3.20) decrease with increasing ℓ and the product $K_{s\ell}\ \phi_\ell$ diminishes rapidly. Even for v'~v the charge exchange kernel is only weakly anisotropic (for E < 10 keV) and only a few terms are expected to be sufficient. Isotropic scattering corresponds to keeping only the $\ell = 0$ term.

The multigroup treatment of the energy variable involves the integration of the Boltzmann equation (equation (3.17) with the P_L scattering approximation) over the range $E_{g+1} \leq E \leq E_g$, defining the group "g". This leads to the

formal multigroup equation (3.29) in terms of the "group" quantities (3.24) - (3.28). Because of the averaging process used in defining the group absorption cross section (3.25) and the group-to-group scattering cross section (3.26), these quantities are now functions of the angular variable $\underline{\Omega}$. Limitations in computer storage and calculational speed dictate that group cross sections that are independent of $\underline{\Omega}$ be used in present codes, however. A traditional method of going about this is to assume the weighting functions $\Phi(\underline{r},\underline{\Omega},E)$ and $\phi_\ell(r,\underline{\Omega},E')$ are separable functions of space-angle and energy. In other words, the energy spectrum of the flux within a group is unchanging throughout the transport medium. Other more sophisticated techniques that accomplish the same purpose but are more generally applicable are also available [36,48].

In principle the general multigroup formulation of equation (3.29) is an exact treatment of the energy variable provided the weighting functions ϕ_ℓ and Φ are known exactly. This is of course not possible, but a good solution can still be obtained if a sufficient number of appropriately structured groups are used to make up for the uncertainty that a poor weighting function might introduce. Better values for the weighting functions (with the possibility of requiring fewer groups) can be obtained in an iterative manner.

The essential basis of the angular treatment by discrete ordinates methods is that the angular distribution of the particle flux is evaluated in a number of discrete

directions. By considering enough directions an arbitrarily accurate evaluation of the angular component can be obtained. Coupling between discrete angular fluxes occurs in the scattering term (the integral to calculate ϕ_ℓ) and in angular derivative terms for curved geometries (cylindrical, spherical, etc.). A critical choice involved in the discrete ordinates approach is that of angle directions and angle integration weights. That is, Ω_i and w_i must be determined so that an approximation of the type

$$\int_{\Omega'} \Phi(r,\Omega')\, d\Omega' \sim \sum_{i=1}^{N} w_i\, \Phi(r,\Omega_i), \qquad (3.30)$$

is as accurate as possible for a given N. Physical arguments suggest (for one-dimensional symmetric geometries) the use of a Gaussian quadrature set which has proved to be sufficient for most applications [46]. For integration in one-dimensional cylinders, Gaussian quadrature can be combined with Tschebyscheff coefficients to account for directions down the length of the cylinder.

The solution to the coupled algebraic equations generated by MGDO methods is obtained in an iterative manner. The group fluxes computed across the spatial and angular meshes (inner iterations) assume a source function (from scattering and fixed sources) based on previous flux values. The newly generated fluxes are used to calculate a

new source and then the process is repeated (outer iterations). Convergence is usually said to have been reached when the difference between the current value of the flux and the previous solution is less than a specified value. When this criterion has been fullfilled (for both inner and outer iterations) the current fluxes are given as the solution. The time required to reach a solution is of course dependent upon the fineness of the space, angle, and energy meshes as well as the convergence desired.

CHAPTER IV

NUMERICAL SOLUTIONS

The numerical work required to obtain neutral transport solutions is divided into two parts. First, it is necessary to generate the appropriate multigroup cross sections (equations (3.25) and (3.26)) for use in the transport equation solver. In general, this may involve a triple integration for each element of the scattering transfer matrix (number of elements ~ (number of energy groups)^2). The calculation must be repeated for each new plasma temperature region that is considered in the analysis. Secondly, an adequate operating mode must be determined for the transport solver that arrives at accurate solutions within reasonable running times. The underlying presumption is that MGDO methods may eventually replace modules presently used for neutral transport where savings in execution time is at a premium. The organization of the present chapter consists of a section discussing the computer code GIMUXS written to calculate multigroup cross sections and a section describing the practical application of the MGDO transport code ANISN to the neutral transport problem. Included in the latter section is a parameter survey over the ANISN operating variables.

Generation of the Neutral Multigroup Cross Sections

The computer code, GIMUXS, was written in FORTRAN IV to evaluate the group-to-group scattering cross section (equation (3.26)) and the total group absorption cross section (equation (3.25)) using analytical fits to experimental cross section data. Features of the code include the ability to consider an arbitrary group structure and an option which arranges the cross sections in a tape library appropriate for look up use by the MGDO code ANISN. The proton and electron target plasma distribution functions are taken to be Maxwellian, and can be evaluated at an arbitrary temperature.

Several others codes have been developed to generate neutral multigroup cross sections [50,51]. GIMUXS utilizes an approximation similar to that used by Pfeiffer which simplifies the evaluation of the neutral multi-dimensional integrals. Common to all codes is the assumption that at best only an energy-dependent function is available for the cross section averages of equations (3.25) and (3.26). (i.e., the weighting functions Φ and ϕ_ℓ are separable in space-angle and energy.)

Mathematical Model and Assumptions

The mild variation of the charge exchange cross section aids in the evaluation of the group-to-group scattering cross section. We have for $K_{s\ell}^{h\to g}(\underline{r})$ from equation (3.26)

$$K_{s\ell}^{h\to g}(\underline{r}) = \int_{E_{h+1}}^{E_h} \varphi_\ell(E') \int_{E_{g+1}}^{E_g} K_{s\ell}(\underline{r}; E'\to E)\, dE\, dE' \Big/ \varphi_{\ell,h}, \tag{4.1}$$

where

$$\varphi_{\ell,h} = \int_{E_{h+1}}^{E_h} \varphi_\ell(E)\, dE', \tag{4.2}$$

and

$$K_{s\ell}(\underline{r}; E'\to E) = 2\pi(2\ell+1) \int_{-1}^{1} \frac{N_i(\underline{r})}{4\pi v'} h_i(\underline{r}, E) \times |\underline{v}-\underline{v}'|\, \sigma_{cx}(|\underline{v}-\underline{v}'|)\, P_\ell(\mu_o)\, d\mu_o. \tag{4.3}$$

The pertinent part of the integral over μ_o is extracted from equation (4.3) to define the expression

$$I_\ell(E', E) = 2\pi(2\ell+1) \int_{-1}^{1} |\underline{v}-\underline{v}'|\, \sigma_{cx}(|\underline{v}-\underline{v}'|)\, P_\ell(\mu_o)\, d\mu_o, \tag{4.4}$$

so that

$$K_{s\ell}(\underline{r}; E'\to E) = N_i(\underline{r})\, \frac{h_i(\underline{r}, E)}{4\pi v'}\, I_\ell(E', E). \tag{4.5}$$

For charge exchange between particles of equal mass I_ℓ is symmetric in the variables E' and E.

The characteristic behavior of I_ℓ is shown in Figure 4.1. The I_ℓ's are essentially the coefficients of the Legendre expansion of the scattering kernel that characterize charge exchange anisotropy. Under two conditions, however, all but the $\ell=0$ (isotropic) terms of equation (4.4) vanish. First, if the charge exchange cross section can be shown to vary (or to be approximated) as

$$\sigma_{cx}(|\underline{v}-\underline{v}'|) = \frac{C}{|\underline{v}-\underline{v}'|} \quad cm^2, \tag{4.6}$$

where C is a constant (cm^3 sec^{-1}), then equation (4.4) becomes

$$I_\ell(E',E) = 2\pi(2\ell+1)C\int_{-1}^{1} P_\ell(\mu_0)\,d\mu_0$$

$$= \begin{cases} 4\pi C & \ell = 0 \\ 0 & \ell \neq 0 \end{cases} . \tag{4.7}$$

Second, if the charge exchange neutral-ion pair have velocities such that

$$v' >> v \qquad \text{or} \qquad v >> v', \tag{4.8}$$

then

$$|\underline{v}-\underline{v}'|\,\sigma_{cx}(|\underline{v}-\underline{v}'|) \sim v'\,\sigma_{cx}(v'), \tag{4.9a}$$

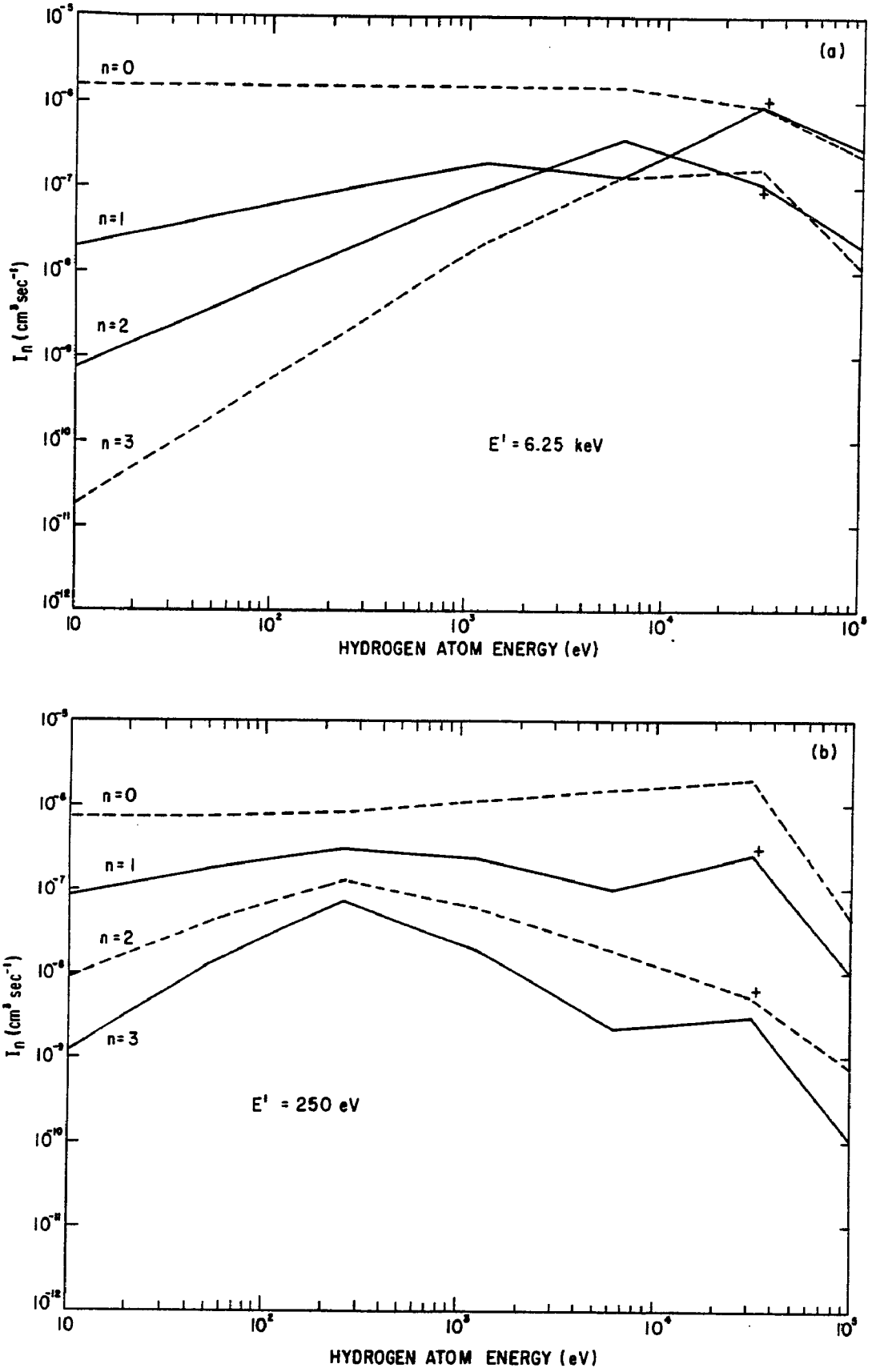

Figure 4.1 Behavior of $I_\ell(=I_n)$ for (a) E'=6.25 keV and (b) E'=250 eV as a function of the energy variable E. All the values of I_ℓ for $\ell>0$ are negative below E~20 keV. At higher energies I_ℓ is positive for $\ell=1,2$.

or

$$|\underline{v}-\underline{v}'|\,\sigma_{cx}(|\underline{v}-\underline{v}'|) \sim v\,\sigma_{cx}(v)\,, \quad (4.9b)$$

so that in either case the $\ell \neq 0$ terms of equation (4.4) vanish, and

$$I_\ell(E',E) = 2\pi(2\ell+1)\,v\,\sigma_{cx}(v)\int_{-1}^{1} P_\ell(\mu_o)\,d\mu_o$$

$$= \begin{cases} 4\pi\, v\,\sigma_{cx}(v) & \ell = 0 \\ 0 & \ell \neq 0 \end{cases} . \quad (4.10)$$

As seen in Figure 2.2 the charge exchange cross section decreases as a function of energy but not as quickly as 1/v below about 10 keV. It is expected therefore that the terms $\ell \neq 0$ in the Legendre series will not vanish but will become increasingly small as ℓ increases (i.e., the deviation from 1/v behavior is not pronounced). This is seen in Figure 4.1. The maximum contribution from $\ell \neq 0$ scattering terms comes when $E' \sim E$. When both the colliding neutral and ion have approximately the same speed, the relative velocity can range from nearly zero to twice the particles velocity depending upon the orientation of the incident particle vectors ($\underline{\Omega}\cdot\underline{\Omega}' = \mu_o$). The cross section may thus have a very large variance when evaluated at these extremes.

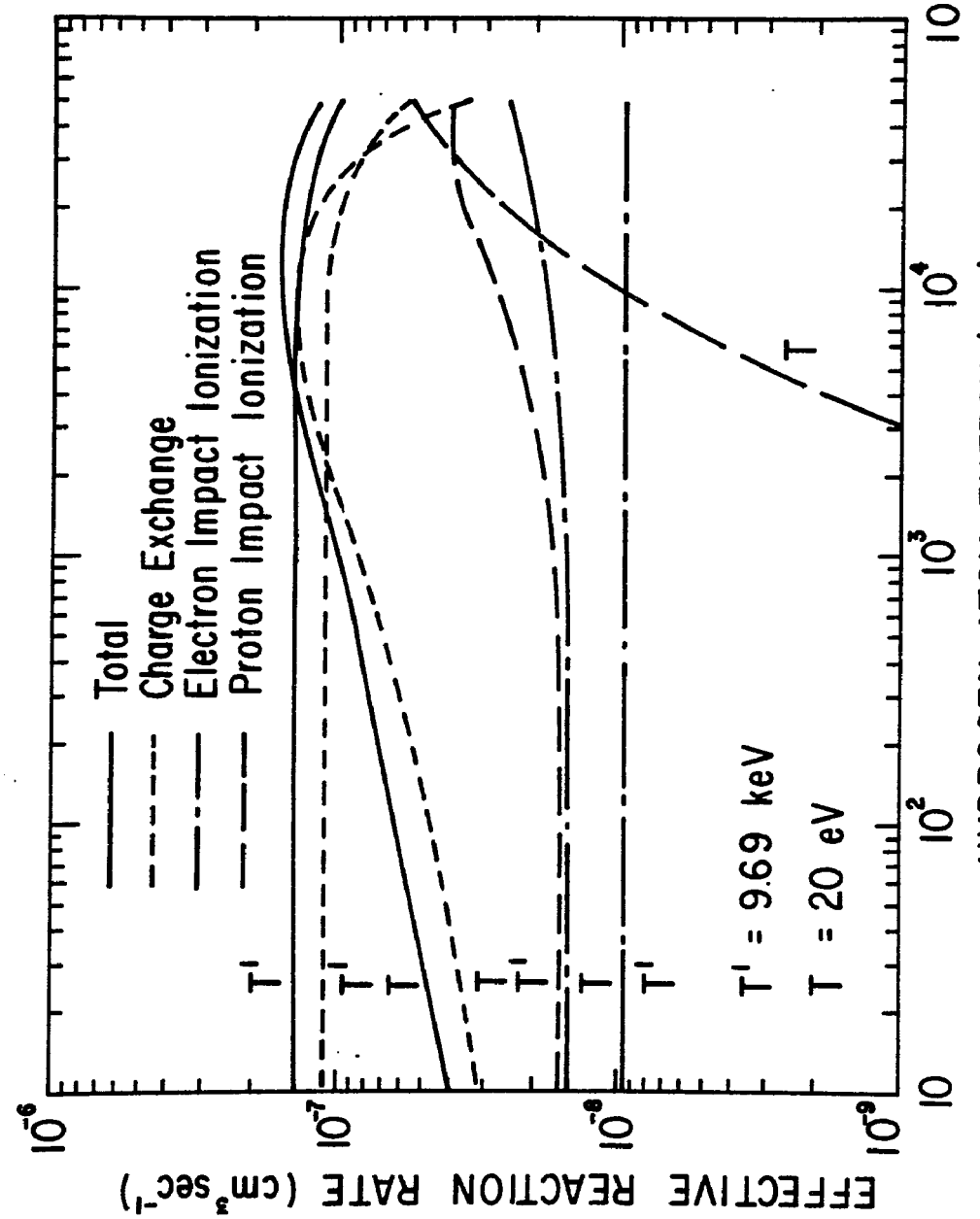

Figure 4.2 The effective interaction rates of hydrogen atoms incident on Maxwellian target distributions versus particle energy for various reactions.

This dependence on the scattering angle is reflected in the larger values of the expansion coefficients. In the case where the cross section itself is a sensitive function of energy, the higher order scattering coefficients can be significant even if the particle speeds are not close. Above 20 keV the charge exchange cross section drops off precipitously as $E^{-3.3}$ (see equation (2.3)). The Legendre coefficients I_ℓ (for $\ell > 0$) not only tend to gain strength in this region as seen in Figure 4.1 but for $\ell=1$ and $\ell=2$ also change sign (forward instead of backward scattering is preferred).

Earlier it was stated that the mild variation of the charge exchange cross section would aid in the evaluation of $K_{s\ell}^{h\to g}$. This is accomplished by noticing that below 20 keV I_ℓ is either a slowly varying function in E for all E' or that the higher order coefficients are small enough to neglect in comparison to the dominant $\ell=0$ term. It is claimed that a suitable group structure can be chosen such that I_ℓ can be considered constant within the defined group limits. It is the intention that a large enough number of groups can be considered in the analysis to offset the possibility of any inaccuracy generated in the approximation. A discussion of the energy group structure will be deferred to a later section in this chapter.

Assuming that I_ℓ can be evaluated at suitable group midpoints the group-to-group scattering cross section $K_{s\ell}^{h\to g}$ (equation (4.1) with equation (4.5)) can be written as

$$K_{s\ell}^{h\to g}(\underline{r}) = I_\ell(\bar{E}_h, \bar{E}_g)\, N_i(\underline{r}) \int_{E_{h+1}}^{E_h} \frac{\Phi_\ell(E')}{v'}\, dE' \times \int_{E_{g+1}}^{E_g} \frac{h_i(\underline{r}, E)}{4\pi}\, dE \Big/ \Phi_{\ell,h}. \tag{4.11}$$

It is noteworthy that the implicit triple integration of equation (4.1) has been replaced by the product of two single dimensional integrals in equation (4.11).

The evaluation of the group absorption cross section (equation (3.25)) presents a similar potential for simplification, as did equation (4.1). The average beam-Maxwellian interaction rate ($v\,\sigma_a^{eff}$, equation (3.14)) is divided into its components and displayed for T = 20 eV and T = 9.69 keV in Figure 4.2. Over the wide range of beam energies E < 20 keV, $v\,\sigma_a^{eff}$ is a slowly varying function both at a low plasma temperature (20 eV) and at a maximum ~ 10 keV. The deviation from a constant value is comparable to that observed for I_ℓ which prompts the utilization of the same approximation for the calculation of $\sigma_{a,g}$. The constraint on a proposed group structure is evidently not effected because of the similarity of the integrand in both instances. The total group absorption cross section is given by

$$\sigma_{a,g}(\underline{r}) = \int_{E_{g+1}}^{E_g} \sigma_a^{eff}(\underline{r},E)\ \Phi(E)\,dE \Big/ \Phi_g \qquad (4.12)$$

$$\text{where} \qquad \Phi_g = \int_{E_{g+1}}^{E_g} \Phi(E)\,dE \ ,$$

and $\sigma_a^{eff}(\underline{r},E)$ is defined in equation (3.14). With the approximation that the average reaction rate for absorption is a constant within the group limits equation (4.12) can be rewritten as (4.13)

$$\sigma_{a,g}(\underline{r}) = v_{\bar{E}_g}\,\sigma_a^{eff}(\underline{r},\bar{E}_g) \int_{E_{g+1}}^{E_g} \frac{1}{v}\,\Phi(E)\,dE \Big/ \Phi_g \ ,$$

where

$$v_{\bar{E}_g} = \sqrt{\frac{2\,\bar{E}_g}{m_n}} \ ,$$

and $\bar{E}_g$ is chosen as the arithmetic mean $\bar{E}_g = \frac{E_g + E_{g+1}}{2}$.

Equations (4.11) and (4.13) are used to evaluate the group-to-group scattering cross section and the total absorption cross section respectively in the code GIMUXS. In the present version of the code the weighting functions ϕ_ℓ and Φ are assumed to be piecewise constant within each set of group limits. It is known that if charge exchange is

dominant in the plasma then the energy distribution of the neutrals will approximately resemble the local ion distribution (for $E < 20$ keV). Near the neutral source (plasma edge), however, not enough charge exchanges have occurred for this to take place and the energy distribution is peaked near the source energy. This demonstrates the difficulty of specifying reasonable weighting functions for the integrals of equations (4.11) and (4.13) for specific plasma conditions. Because of the slowly varying nature of the reaction cross sections, however ($E < 20$ keV), the choice is not expected to be critical.

Method of Solution

The analytical and numerical methods used to evaluate $K_{s\ell}^{h\to g}$ and $\sigma_{a,g}$ are now described. With the assumption of piecewise constant weighting functions equations (4.11) and (4.13) reduce to

$$K_{s\ell}^{h\to g}(\underline{r}) = I_{\ell}(\bar{E}_h, \bar{E}_g)\, N_i(\underline{r})\, H_i^g(\underline{r}) \times \frac{1}{E_h - E_{h+1}} \int_{E_{g+1}}^{E_g} \frac{1}{v'}\, dE', \tag{4.14}$$

and

$$\sigma_{a,g}(\underline{r}) = v_{\bar{E}_g}\, \sigma_a^{eff}(\underline{r}, \bar{E}_g)\, \frac{1}{E_g - E_{g+1}} \int_{E_{g+1}}^{E_g} \frac{1}{v}\, dE, \tag{4.15}$$

where

$$H_i^g(r) = \int_{E_{g+1}}^{E_g} \frac{h_i(r,E)}{4\pi}\, dE .$$

Since Maxwellian target ion distribution functions are considered for h_i, H_i^g can be evaluated analytically. We have

$$\frac{h_i(E)}{4\pi} = \frac{1}{2\pi^{3/2}} \sqrt{E}\ \frac{1}{T^{3/2}}\ e^{-E/T}, \qquad (4.16)$$

so that

$$H_i^g = \frac{1}{2}\left(\frac{1}{\pi T}\right)^{3/2} \int_{E_{g+1}}^{E_g} \sqrt{E}\ e^{-E/T}\, dE. \qquad (4.17)$$

By defining the change of variables $x = \sqrt{E/T}$ and integrating by parts, some algebraic manipulation yields

$$H_i^g = \frac{1}{2}\left(\frac{1}{\pi}\right)^{3/2} \qquad (4.18)$$

$$\times \left\{ \left[x_{g+1} e^{-x_{g+1}^2} - \frac{\sqrt{\pi}}{2} \operatorname{erf}(x_{g+1}) \right] \right.$$

$$\left. - \left[x_g\, e^{-x_g^2} - \frac{\sqrt{\pi}}{2} \operatorname{erf}(x_g) \right] \right\},$$

where

$$x_{g+1} = \sqrt{\frac{E_{g+1}}{T}}$$

$$x_g = \sqrt{\frac{E_g}{T}} \quad ,$$

and the error function is

$$erf(x) = \frac{2}{\sqrt{\pi}} \int_0^x e^{-u^2} du \quad . \qquad (4.19)$$

The integrals over energy can likewise be evaluated analytically in equations (4.14) and (4.15) giving

$$K_{s\ell}^{h \to g}(r) = I_\ell(\bar{E}_h, \bar{E}_g)\, N_i(r)\, H_i^g(r)\, \frac{2}{B\left(\sqrt{E_h} + \sqrt{E_{h+1}}\right)} \quad , \qquad (4.20)$$

and

$$\sigma_{a,g}(r) = v_{\bar{E}_g}\, \sigma_a^{eff}(r, \bar{E}_g)\, \frac{2}{B\left(\sqrt{E_g} + \sqrt{E_{g+1}}\right)} \quad , \qquad (4.21)$$

where $B = 1.39 \times 10^6$ cm sec^{-1} is a constant that relates E in eV and particle speed in cm sec^{-1} ($B = c\sqrt{\frac{2}{m_n c^2}}$, c = the speed of light in cm sec^{-1}). The components of equations (4.20) and (4.21) are calculated and assembled in GIMUXS to compute the group-to-group scattering ($K_{s\ell}^{h \to g}$) and total group

absorption ($\sigma_{a,g}$) cross sections.

The evaluation of the double integral (over E' and ') for σ_a^{eff} can potentially be time consuming but for isotropic target distributions a reduction to a one-dimensional integral (over the relative speed) is possible [52]. Thus, for example, the ionization rate due to electron impact assuming a Maxwellian electron distribution is transformed as

$$\int_{E',\underline{\Omega}'} \frac{h_e(E')}{4\pi} |\underline{v}-\underline{v}'| \; \sigma_{e;}(|\underline{v}-\underline{v}'|)\, dE'\, d\Omega' \qquad (4.22)$$

$$= \frac{v}{\pi^{\frac{1}{2}} x^2} \int_0^\infty dy \; y^2 \, \sigma_{e;}\left(\frac{y}{\beta}\right) \left[e^{-|x-y|^2} - e^{-(x+y)^2} \right],$$

where

$$y = \beta |\underline{v}-\underline{v}'|$$

$$x = \beta v$$

$$\beta^2 = \frac{m_e}{2kT} \quad .$$

An adaptive Romberg [53] integration routine was chosen to evaluate the one-dimensional integrals of equations (4.20) and (4.21) in GIMUXS. Several other integrals of the same nature had previously been calculated with the scheme and its extension to this application was a natural one.

Program Description

GIMUXS is the first version of a code designed to efficiently generate neutral multigroup cross sections for use with standard neutron transport codes. GIMUXS consists of ~375 source cards subdivided into a main program and 9 function subroutines. Because of its small size no attempt has been made to compile a library load module of the code. Compilation time is minimal (~ 4 sec, IBM 360/91) at its present level of usage.

The flow of the calculation is shown in Figure 4.3 The main program reads the input data, generates the cross sections and writes and/or stores them on tape files. It is the exclusive duty of the function subroutines to perform the integrations and supply the cross section data. Subroutine function RINT1, which controls the Romberg itegration procedure is first called from MAIN to directly integrate I_ℓ. The integrand functions P0, P1, P2, or P3 are passed at the same time which provide the appropriate Legendre polynominals and charge exchange cross sections. Subroutine ABSXS sets up the integration for the total absorption cross section and calls RINT1 as a consequence. The integrand is provided through the subroutine function F and the cross section functions FIXSEC (ion impact ionization) and FEXSEC (electron impact ionization). If the cross sections are printed out the subroutine AWRITE is called.

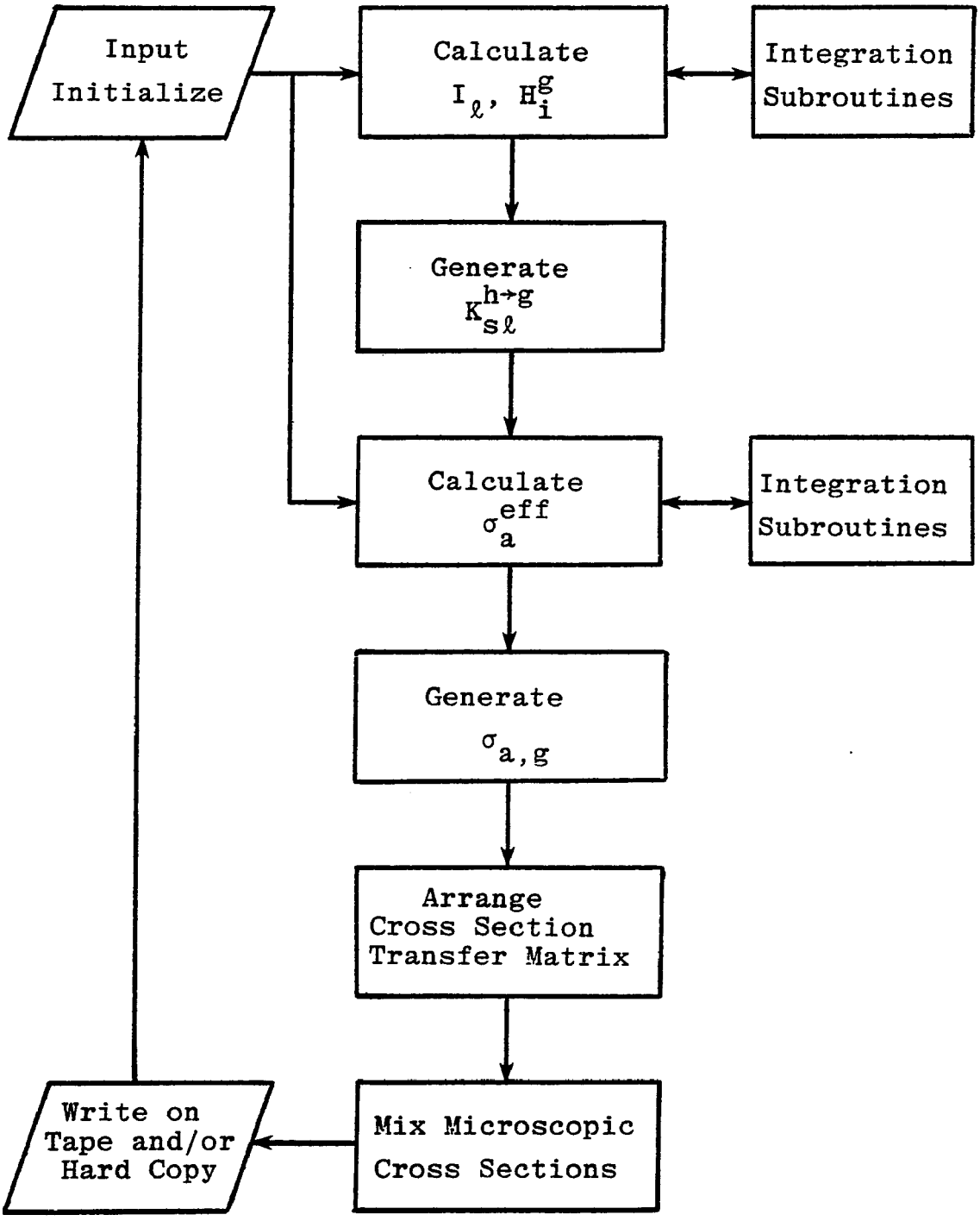

Figure 4.3 Flow of the calculations done in the code GIMUXS.

GIMUXS currently runs with a core storage requirement of approximately 210 K bytes on the IBM 360/91. All calculations are done in the Real*8 (Double Precision) mode. Current limitations of the code are to P_3 order of scattering and a maximum of 50 energy groups. The latter restriction can be relaxed easily with minor changes in storage allocation. Appendix A contains the input data description, output options and labeled COMMON variables used in GIMUXS.

Transport Code Utilization

Now that suitable neutral multigroup cross sections have been generated, it is possible to solve the transport equation by a conventional MGDO code. In this section the model of neutral-plasma interaction used by the MGDO transport code ANISN is described. The operation of a large versatile transport code depends on the specification of many input variables designed to meet the needs of a particular problem. The question must be asked: Does one particular code configuration (spatial mesh size, material zone configuration, group structure, order of scattering approximation, etc.) represent an adequate analysis (does it converge to the correct solution?). The analysis and results of a parameter survey considering the ANISN variables likely to effect the calculated neutral distributions is included in this section.

The Plasma-Neutral Model and ANISN Operation Guidelines

The scenario for background neutral transport in a tokamak plasma was presented in Chapter I, and details of the interactions in Chapter II. It was also demonstrated that neutron transport and neutral transport were analogous (analogous interactions, boundary conditions and sources) and that similar solution techniques could be used. The actual model for neutral transport employed by the MGDO neutron transport code ANISN is now presented.

Hydrogen source atoms are assumed to be incident on a proton and electron plasma. It is possible to consider transport in one-dimensional geometries that are planar, cylindrical or spherical; the cylinder option most nearly models the actual toroidal geometry of a tokamak. The calculations are therefore performed in infinite cylindrical geometry. The plasma temperatures and densities are specified on a set of concentric shells each characterized by an isotropic Maxwellian distribution function; the plasma properties are homogeneous in each shell. The modelling of continuously changing plasma temperature and density profiles is slightly different than in neutron analysis where to first order the zones characterized by different cross section sets are distinct physical regions (cladding, moderator, fissionable material, etc.).

The incident source neutrals are assumed to result from the immediate dissociative ionization of hydrogen gas (H_2) desorbed from the outer material wall. In reality the

disassociation process takes place over a finite volume, (discussed in Chapter II) frequently small in comparison to the plasma dimensions; this effect will be neglected here. The resulting Franck-Condon neutrals have energies of about 3 eV. The inward neutral current at the boundary is therefore assumed to originate from an isotropic uniform flux distribution in the 3 eV energy group (using the shell source option). The results of the calculations can be scaled to a neutral edge density equivalent to this flux value since the transport equation is linear.

Standard use is made of the ANISN code in solving the neutral multigroup equations. A revised version [54] of the original code[3] aids in the reading of input variables and allows the dump of principal results to an external file. The variables specifically designed to describe neutron transport (particle flux, reaction activation, etc.) can also be used to interpret neutral atom transport. However, other calculated quantities are necessary and more convenient (average neutral energies and densities, sputtering rates, etc.) for neutral analysis. For this purpose an external analysis program accepts the binary dump results from ANISN and performs appropriate calculations. A more thorough description of the neutral analysis package is given in Appendix B.

ANISN Parameter Survey

The operating configuration in which ANISN runs largely determines the accuracy of its solutions. The results of a parameter survey, directed at attaining reliable solutions for neutral transport analysis, are presented in this section. First, the variables of the operating structure are defined.

The energy group structure is chosen to minimize errors associated with approximations in the group cross sections and to give sufficient resolution to calculated results that are critically dependent on energy. Both the positioning of the energy intervals and the fineness of their mesh must be specified. A greater number of energy groups implies that more calculations must be performed to solve the individual group equations and hence more computer running time is required.

A spatial interval structure must be specified in ANISN which determines the step size over which finite differences are taken to calculate derivative terms and transport from neighboring points. A smaller step size implies a more accurate finite difference approximation but consumes a proportionately greater amount of calculation time.

It is possible with the code ANISN to consider an arbitrary number of terms in the Legendre expansion of the particle scattering kernel provided the cross sections are available. The inclusion of the higher order scattering terms may be necessary depending on the nature of the kernel

to assure an accurate treatment of the transport. The consideration of a greater number of terms will use up additional computer time.

The order of angular quadrature is related to the number of discrete rays used to treat the angular variable in the transport equation. A greater number of discrete ordinates permits a more accurate evaluation of the angle integral in the scattering source term. It is expected that enough rays must be considered to sufficiently resolve the higher order terms in the Legendre scattering approximation. As the number of discrete angles increases so does the code execution time.

The problem with modeling a continuous plasma profile is that the material (cross section) zones cannot be as readily discerned as when dealing with solid media (neutron analysis). The selection of homogeneous zones will depend on the variation of cross sections as a function of position. A finer zone mesh will contribute to a greater calculation time in two ways; first, by increasing the number of cross section sets manipulated in ANISN, and secondly, by increasing the number of cross section sets that must be calculated in GIMUXS.

A convergence criteria is inputted to ANISN that is proportional to the tolerance allowed between consecutive inner iteration fluxes and consecutive outer iteration solutions. A smaller allowed error results in greater accuracy but more time consuming iterations are required.

For the purposes of the parameter survey a nominal plasma is considered: TFTR [55] characteristics with equal ion and electron temperatures (T) and densities (N). The plasma profiles are shown in Figure 4.4(b). They are generated by the fits

$$T = T_o \left[1 - \left(\frac{r}{r_o}\right)^{\alpha} \right] + T_B$$

$$N = N_o \left[1 - \left(\frac{r}{r_o}\right)^{\beta} \right] + N_B \qquad (4.23)$$

where the constants are taken from Table IV.1. The parameter r_o is the tokamak plasma minor radius in centimeters. The TFTR plasma is felt to be a good test case since it represents a plasma with a maximum ion temperature at the limit where the approximation of equation (4.11) is valid. It is recalled that at energies much greater than 20 keV I_ℓ can no longer be considered a constant. The TFTR plasma is also of moderate size and density so that magnification of effects of the approximation due to a larger number of collisions in the design analysis of a larger device (e.g., EPR r_o = 210 cm [56]) will be minimal. It is judged that the conceptual results using TFTR will be valid for all devices in current operation or for next generation beam driven machines. Vacuum boundary conditions are assumed to exist for all cases. The source of

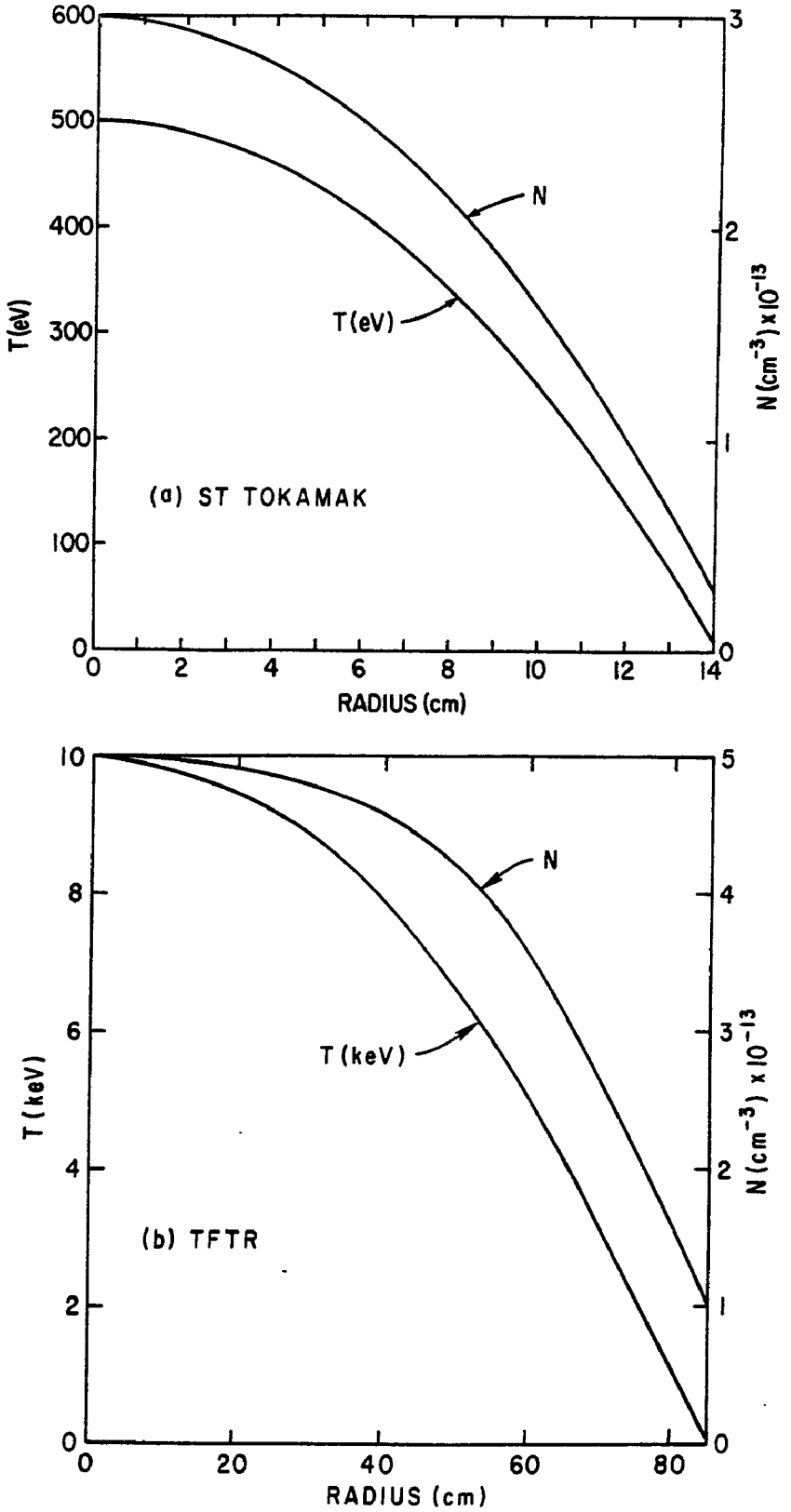

Figure 4.4 Plasma temperature ($T=T_i=T_e$) and density ($N=N_i=N_e$) profiles for the (a) ST and (b) TFTR tokamaks.

	ST	TFTR
r_0 (cm)	14	85
T_0 (eV)	490	9950
T_B (eV)	10	50
α	2	2
N_0 (cm^{-3})	2.7×10^{13}	4.0×10^{13}
N_B (cm^{-3})	3.0×10^{12}	1.0×10^{13}
β	2	3

Table IV.1 Parameters for the fits used to determine plasma densities and temperatures in equation (4.23).

background neutrals is at the outer boundary (vacuum wall) with an incident isotropic flux at 3 eV.

Group Structure

It is recalled that to make the approximation that I_ℓ was constant within an energy group, it was assumed that a suitable group structure existed. This restriction along with other considerations are used to construct a working structure. The effects of the fineness of the energy mesh is tested on the TFTR model.

The Figure 4.1 shows I_ℓ to be a relatively slowly varying function in log E. This suggests that if the energy structure is chosen to contain equal increments in log E, that the conditions for use of the approximation will be satisfied. Where the higher orders of I_ℓ do change rapidly their contribution to the total scattering process is negligible.

Another desirable quality of the energy structure would be to resolve the neutral spectrum at each point in the plasma. It is known that after several charge exchange events the neutral population will take on the characteristics of the target ions. These will be Maxwellian energy distributions ranging from low temperatures ($T \sim 20$ eV) at the plasma edge to high temperatures at the plasma core ($T \sim 10$ keV). The tendency for Maxwellian distributions to be more skewed for low temperatures and the need to cover a wide range in energy suggests that the energy groups be narrower in the low

energy regime and wider as energy is increased. Equal increments in log E fulfill these criteria. In addition, a rough quantitative estimate is now available for the energy mesh and minimum energies to be considered. That is, it will be necessary to resolve the spectrum of outfluxed neutrals that originate predominantly in the low temperature plasma boundary region.

In multigroup analysis it is advantageous to arrange the energy group structure so that the particle flux is distributed evenly between groups. Thus, the transport in one particular group does not overshadow the entire analysis (if this were the case the other groups would not be needed). Since we know that the neutral flux will be approximately Maxwellian in the volume of the plasma an estimate can be made of the amount of flux as a function of an energy interval. The total fraction of particles in a flux distribution up to an energy ϵ is given by A, where

$$A = \int_0^{\epsilon} \Phi(E)\, dE \,. \tag{4.24}$$

If the flux ϕ is a normalized Maxwellian, (Temperature = T), then

$$A = \int_0^{\epsilon} \left(\frac{E}{T}\right) \exp\left(-\frac{E}{T}\right) \frac{dE}{T}$$

$$= 1 - e^{-x}(x+1) \,, \tag{4.25}$$

where

$$x = \frac{\epsilon}{T} .$$

A is plotted as a function of x in Figure 4.5. The abscissa has a logarithmic scale and it is seen that for the range $.6 < x < 5$, A is approximately linear in log x (compare to the dashed line). The particles in this range represent about 80% of those in the entire distribution. In the linear region then, energy groups formed by equal increments in $\log \frac{\epsilon}{T}$ will contain approximately equal fractions of the particle flux.

For the reasons considered above an energy structure which is based on a uniform mesh in log E is chosen. Thus,

$$\log E_g - \log E_{g+1} = k , \qquad (4.26)$$

where k is a constant or

$$E_g = (10^k) E_{g+1} . \qquad (4.27)$$

For a fixed energy range that must be covered, a smaller value of k implies the use of a larger number of energy groups. In investigating a Maxwellian plasma it is necessary to consider energies up to several times the maximum ion temperature because of the long energy tail.

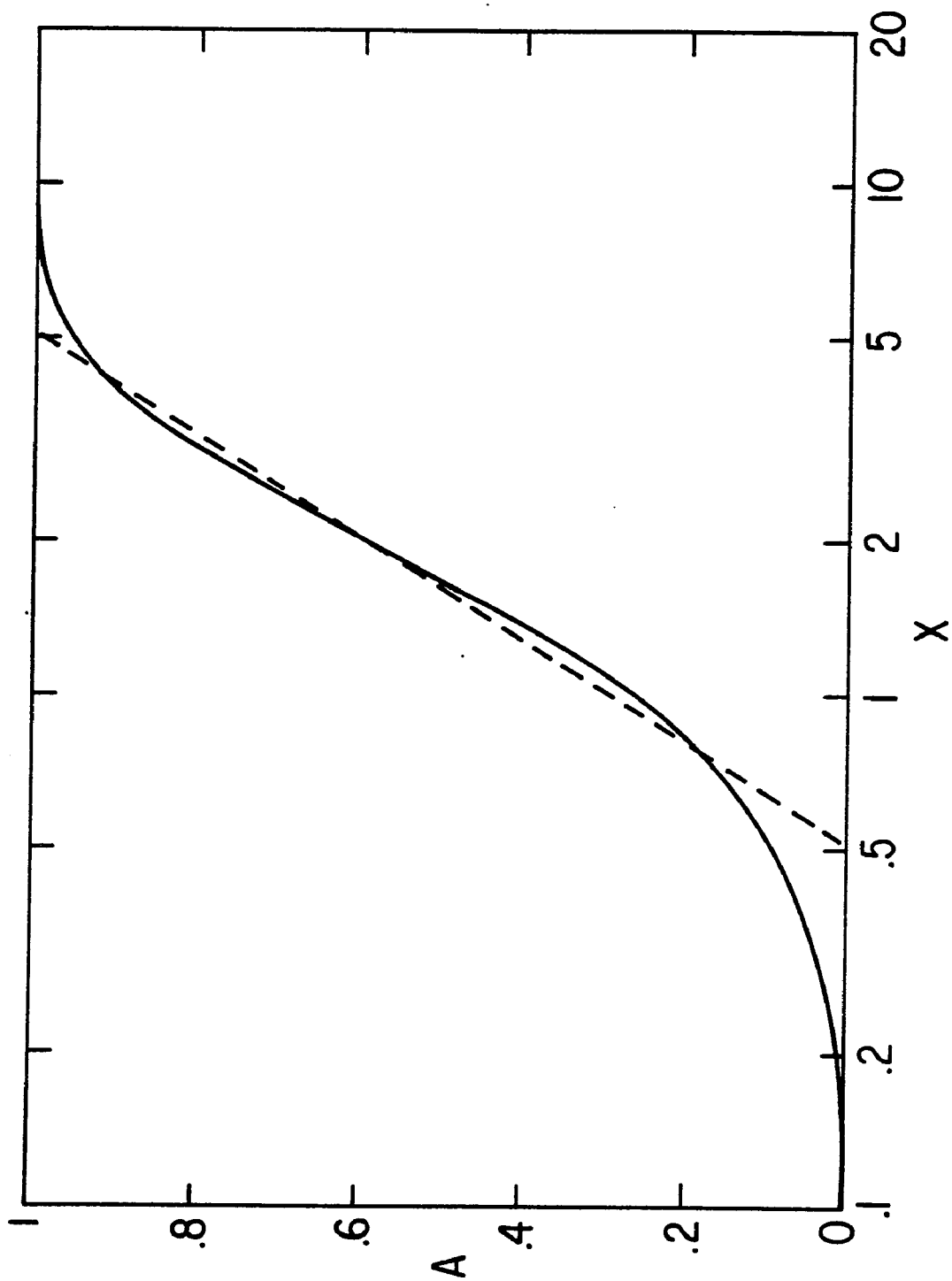

Figure 4.5 Semi-logarithmic plot of the fraction of total particles in a Maxwellian flux distribution (A) with a normalized energy less than $x = \varepsilon/T$.

Since in this analysis the maximum ion temperature will be about 10 keV the energy range considered is 0-55 keV. Figure 4.6 shows a plot of energy versus group number for three values of the parameter k. For the 31 group set the group limits were picked as whole numbers only approximately corresponding to the dashed line shown. The exact value of k or the precise positioning of the points is not critical to the calculations, however. For all group structures the source group was centered about 3 eV.

Shown in Figure 4.7 are the hydrogen neutral density profiles calculated for the TFTR plasma with the 11, 31, and 50 group structures of Figure 4.6. The ANISN runs are made with "conservative" operating parameters: S_8 angular quadrature, isotropic (P_o) scattering, a convergence tolerance (EPS) of 10^{-3} and 60 spatial intervals with 8 material zones fitted nonuniformly closer to the outer boundary. The neutral atom population is normalized to an edge density of 1×10^{10} cm^{-3} (equivalent to a neutral gas (H_2) pressure of $\sim 1.5 \times 10^{-3}$ Torr at T = .025 eV) which is fairly typical of present day discharges. The difference in the neutral density profiles of Figure 4.7 is negligible. The other important area of concern in the neutral calculation is the neutral outflux at the plasma boundary. Table IV.2 summarizes these results and the outflux spectra are compared in Figure 4.8. The 11 group calculation requires much less computation time but the outflux resolution is not adequate. This could be important where

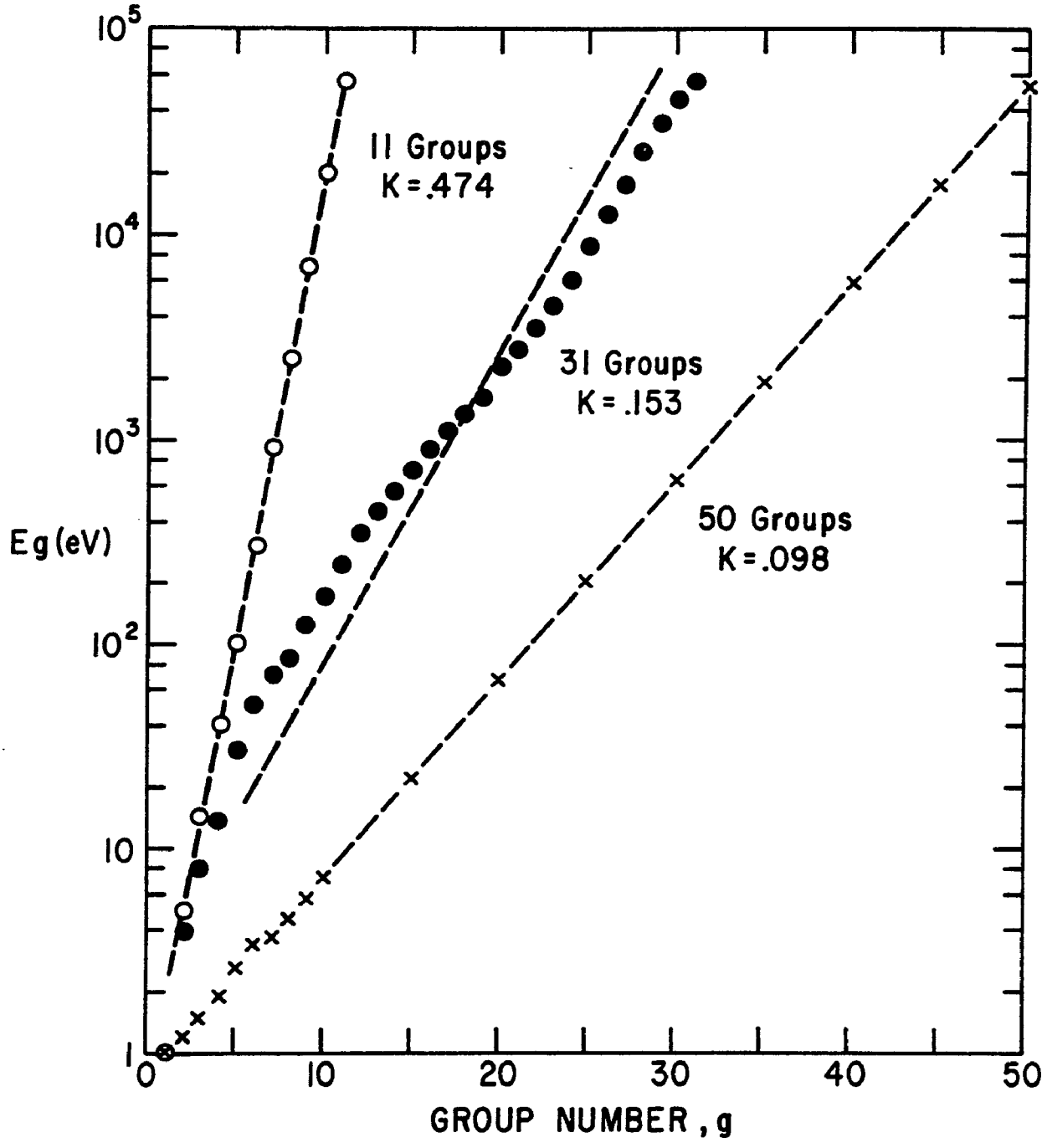

Figure 4.6 The energy group limits formed for various values of the parameter k. For the middle structure the group limits were chosen to only approximately conform to the given fit.

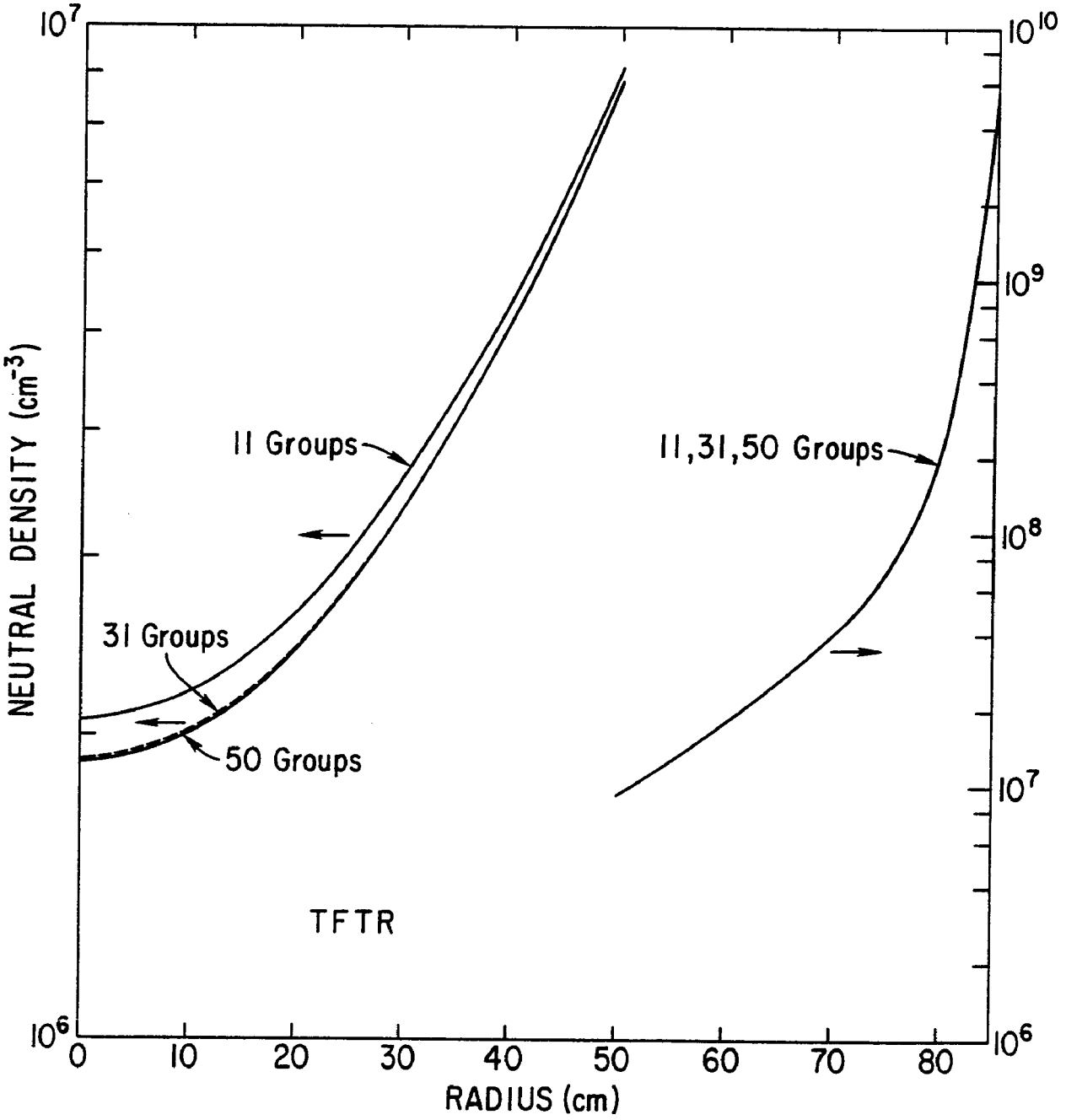

Figure 4.7 Hydrogen atom densities for the TFTR tokamak calculated using different total numbers of groups. The results are normalized to a neutral edge density of 1×10^{10} cm^{-3}.

	Relative Density Attenuation	Average Energy of Outflux (eV)	Outflux Current (cm^{-2} sec^{-1})	Execution Time (sec) IBM 360/91
11 Groups	4.84×10^3	2185	3.15×10^{15}	16.08
31 Groups	5.28×10^3	1854	3.10×10^{15}	75.24
50 Groups	5.32×10^3	1836	3.10×10^{15}	113.9
120 Intervals	5.32×10^3	1858	3.10×10^{15}	145.9
60 Intervals	5.30×10^3	1854	3.11×10^{15}	81.24
29 Intervals	5.64×10^3	1836	3.09×10^{15}	42.18

Table IV.2 Comparison of results for different total numbers of energy groups and spatial intervals for the TFTR plasma.

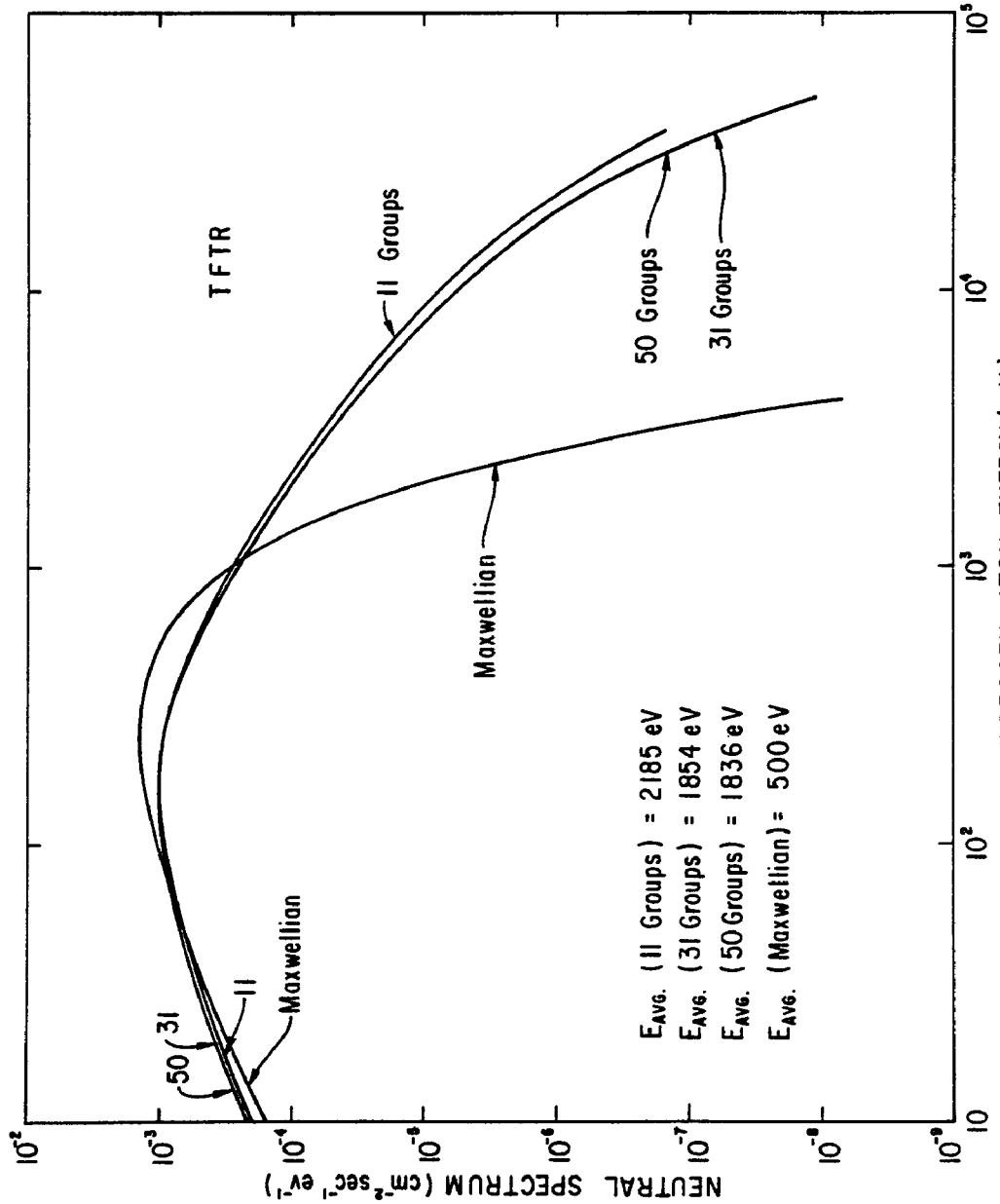

Figure 4.8 The spectrum of outfluxed charge exchange neutrals at the outer boundary of the TFTR tokamak using different total numbers of groups. The total outflux is normalized to 1 cm^{-2} sec^{-1}.

sputtering yields for wall materials are heavily energy dependent. The 31 group results are not significantly different than those of the 50 group set and hence are chosen as a nominal standard. The relatively few number of energy groups in neutral analysis (over 100 groups are required in some neutron studies) is accounted for by the smoothness of the cross sections (lack of energy resonances).

Spatial Interval Structure

Guidelines exist for the selection of spatial mesh points for ANISN based on neutron transport experience. The question is, do these represent valid criteria for neutral transport? The objective is to avoid the negative angular and/or scalar fluxes that result from too wide an interval structure. The neutron criteria for the radial mesh size (ΔR) is approximated by the following relationship [3]:

$$\Delta R \leq \frac{1 + \Sigma_{g-g}^{S_o} / \Sigma_g^t}{4 \Sigma_g^t} \quad , \tag{4.28}$$

where Σ_g^t is the largest total group cross section in a region and $\Sigma_{g-g}^{S_o}$ is the corresponding within group scattering cross section. For neutrals interacting with the TFTR boundary plasma, that has the characteristics $T \sim 200$ eV, $N = 10^{13}$ cm^{-3}, we have

$$\Sigma_g^{+} = .63 \ cm^{-1} \qquad \Sigma_{g-g}^{S_o} = .81 \ cm^{-1} \ , \quad (4.29)$$

so that

$$\Delta R \leq .40 \ cm \ .$$

The same criteria yields smaller (up to a factor of 2) values for ΔR as the center of the plasma is approached. The implied number of spatial intervals (~ 200) is impractically large for normal calculations. Indeed, the relationship (4.28) is recognized as stringent and so there is a considerable amount of intuitive judgement involved in its application. Equation (4.28) is therefore applied near the outer boundary where the cross sections for attenuation of the nearby source neutrals is high and the flux will change rapidly. The mesh size is expanded after several attenuation mean free paths but is not varied more than a factor of two between adjacent intervals as recommended [3]. The cross sections for neutral attenuation decrease as the neutrals gain energy by charge exchange.

The effects of several non-uniform interval structures were investigated. These range from equal increments of separation in log r starting from the boundary to simpler structures described in Table IV.3. These mesh structures are used to calculate the results displayed Table IV.2. We use 31 energy groups, P_o scattering, S_8 angular quadrature, 8 material zones and EPS = 10^{-3}. It is sufficient to

Interval Range	Interval Mesh Size (cm)		
0 - 60 cm	5	2	1
60 - 80 cm	2	1	.5
80 - 85 cm	1	.5	.25
Total Number of Intervals	29	60	120

Table IV.3 Spatial mesh structure for the TFTR plasma. Distance is measured from the cylindrical axis.

display the results in tabular form since the plots of neutral densities and the outflux spectra are nearly identical to those of Figures 4.7 and 4.8. It is somewhat surprising to note that the 29 interval structure, which halves the stringent criteria rule, has results that are not significantly different than the other two sets and is hence adequate for the analysis. The execution time is seen to be directly proportional to the number of spatial intervals. In a realistic application it will probably be sufficient to use linear interpolation to calculate quantities of interest at intermediate points.

Order of Scatter

The charge exchange scattering kernel (equation (3.16)) is only slightly anisotropic and so only a few terms are expected to be significant in the scattering expansion. This can be seen from the relative magnitudes of I_ℓ (essentially the coefficients in the expansion) in Figure 4.1. It is recalled form earlier discussions that the scattering anisotropy is enhanced when $v' \sim v$ and that backward scattering is slightly favored when $E \lesssim 20$ keV. To determine the maximum effect that the higher order scattering terms have on transport we consider a TFTR size device with a one temperature (homogeneous) plasma that will promote collisions between ions and neutrals with the same velocity. Table IV.4 presents results for low (20 eV) and high (9.69 keV) temperatures and also low ($.5 \times 10^{13}$ cm^{-3}) and high (1×10^{14} cm^{-3}) density cases. As expected the

		Relative Density Attenuation	Average Energy of Outflux (eV)	Outflux Current ($cm^{-2}sec^{-1}$)	Execution Time (sec)
T = 20 eV, N = 5×10^{12}	P_0	9.67×10^{1}	39.5	2.04×10^{15}	18.91
	P_1	1.10×10^{2}	39.0	2.13×10^{15}	27.42
	P_3	1.10×10^{2}	39.0	2.13×10^{15}	47.70
T = 20 eV, N = 1×10^{14}	P_0	3.27×10^{18}	39.6	1.98×10^{15}	23.70
	P_1	3.86×10^{18}	39.2	2.07×10^{15}	32.78
	P_3	3.89×10^{18}	39.2	2.07×10^{15}	52.85
T = 9.69 keV, N = 5×10^{12}	P_0	1.88×10^{2}	14.1×10^{3}	4.16×10^{15}	17.04
	P_1	1.87×10^{2}	14.1×10^{3}	4.16×10^{15}	25.57
	P_3	1.87×10^{2}	14.1×10^{3}	4.16×10^{15}	46.32
T = 9.69 keV, N = 1×10^{14}	P_0	8.78×10^{4}	13.6×10^{3}	3.27×10^{15}	20.37
	P_1	6.17×10^{4}	13.4×10^{3}	3.21×10^{15}	29.28
	P_3	6.17×10^{4}	13.4×10^{3}	3.21×10^{15}	49.51

Table IV.4 Comparison of P_0, P_1, and P_3 scattering results in a homogeneous plasma slab (half width = 85 cm) for various temperatures and densities.

differences between P_o and P_1 results are not large and the inclusion of higher orders (P_3) present virtually no change. It is interesting to note that at low energies (T = 20 eV), where backward scattering is preferred, that the outflux is slightly greater and penetration into the plasma is less than when the effect of the anisotropic P_1 and P_3 scattering is included. The preference is to backscatter the neutrals out of the plasma. At the higher energies (T = 9.69 keV) where the drop in the charge exchange cross section favors forward scattering the effect is reversed.

The effect of the higher order scattering approximations are considered on a more realistic plasma in Table IV.5. Here the runs are for TFTR with 31 groups, 60 spatial intervals, S_8 angular quadrature, EPS = 10^{-3} and 8 material zones. There is essentially no discrepancy between the results in these cases. For an inhomogeneous plasma the probability that a neutral will charge exchange with an ion with close to the same velocity is even less then in the homogeneous case. It is concluded that for plasmas of current interest (T < 10 keV) that the P_o (isotropic) scattering approximation is sufficient. Only for plasmas with temperatures much above 10 keV (ignited thermonuclear machines) will this not be the case.

Order of Angular Quadrature

The order of angular quadrature is related to the number of discrete rays along which the angular flux is calculated across the spatial mesh. In cylindrical geometry it is

possible to have more than one ray with a particular cosine to the surface normal, since additional ordinates are required to "look down" the cylindrical axis. For anisotropic scattering, which can be sensitively dependent on the relative scattering angle, it will be necessary to resolve the scattering function with many rays. The discrete ordinates are chosen to satisfy certain physical arguments such as symmetry and yielding positive fluxes.

The results of calculations with various orders of angular quadrature (number of discrete rays) are presented in Table IV.5. The TFTR plasma is investigated with 31 groups, P_o scattering, 60 spatial intervals, 8 material zones and convergence 10^{-3}. The S_2 results (which consider only a single ray in and out of the plasma) are the only set not in sufficient agreement. Another problem with low order quadrature is that the important angular dependence in the calculation for neutral sputtering rates cannot be considered in enough detail. For this reason, also, it is advisable that at least S_4 quadrature be used in most neutral studies.

ANISN Convergence

The specification of the parameter EPS, inputted to ANISN, controls a number of convergence criteria [3]. The inner iterations are considered converged when both the integral self-scatter error and the integral removal error are less than $\frac{EPS \cdot S}{IGM}$ or when the maximum flux deviation is less than EPS. S is the total source (fixed + fission) and

	Relative Density Attenuation	Average Energy of Outflux (eV)	Outflux Current (cm^{-2} sec^{-1})	Execution Time (sec) IBM 360/91
P_0 Scattering	5.28×10^3	1854	3.10×10^{15}	75.24
P_1 Scattering	5.27×10^3	1805	3.13×10^{15}	84.84
P_3 Scattering	5.27×10^3	1805	3.13×10^{15}	143.6
S_2 Quadrature	5.37×10^3	1918	3.19×10^{15}	37.62
S_4 Quadrature	5.54×10^3	1853	3.13×10^{15}	46.56
S_8 Quadrature	5.28×10^3	1854	3.10×10^{15}	75.24
S_{12} Quadrature	5.20×10^3	1860	3.09×10^{15}	114.7

Table IV.5 Comparison of results for different orders of scattering and angular quadrature for the TFTR plasma.

IGM is the number of groups. Since the integral tests are sometimes easily satisfied, a point flux convergence can also be specified. When this is done the inner iterations are not considered converged until the maximum pointwise flux deviation is less than 2·EPS. The outer iteration is considered converged when the total source ratio between successive iterations differs from 1.0 by less than EPS, the total scatter ratio differs from 1.0 by less than 2·EPS and the upscatter ratio differs from 1.0 by less than 2·EPS.

Runs for various values of EPS are reported in Table IV.7. We consider the TFTR plasma with 31 groups, P_o-S_8, 60 spatial intervals and 8 material zones. The smaller the value of EPS, the more inner and outer iterations that must be performed to satisfy the more stringent criteria. Execution time is notably increased. The additional outer iterations provide an opportunity for more neutral penetration into the plasma but the effect is small after over three orders of magnitude attenuation. It is judged, therefore, that values of EPS as great as 10^{-2} and possibly 10^{-1} are sufficient for ANISN neutral transport.

Material Zone Structure

In breaking up the continuous plasma profile into regions of homogeneous plasma the implicit assumption is that the overall magnitude of the cross sections do not change drastically between contiguous zones (which may occur in neutron analysis). This is also to say that the regions should not be larger than the local mean free path for

interaction derived from local plasma conditions. If this were the case, the zone mesh would be too coarse to sufficiently resolve the cross section evolution.

The mean free path to a collision of type k for a neutral with speed v_n in a homogeneous plasma medium with density N is

$$\lambda_k = \frac{v_n}{N \langle \sigma v \rangle_k} \quad , \tag{4.30}$$

where $\langle \sigma v \rangle_k$ denotes the usual average of the reaction rate over the target velocity distribution function. To estimate the variation of the neutral mean free paths in the body of the plasma we notice the following: charge exchange and electron impact ionization are the dominant interaction mechanisms, charge exchange is sufficient so that $v_n \sim v_i$ where v_i is the ion velocity, and for the energy regime of interest (20 eV < $T_{i,e}$ < 10 keV), $\langle \sigma v \rangle_{ei}$ ~ constant and $\langle \sigma v \rangle_{cx}$ ~ constant (see Figure 4.2). Then

$$\lambda \sim \frac{v_i}{NC} \quad , \tag{4.31}$$

where C is a constant ($cm^3\ sec^{-1}$) equal to the total average reaction rate. To construct a zone mesh we constrain the total mean free path not to change by more than a constant (a_n)between adjacent zones or

$$\lambda_1 = a_1 \lambda_2 \quad . \tag{4.32}$$

The radial zone divisions corresponding to equation (4.32) are calculated by supplying information as to the ion velocity and electron density profiles from equation (4.23). The density variation, however, can usually be chosen much finer than the zone regions in MGDO codes so it is only necessary to consider changes in λ due to the ion velocity (temperature profile). Choosing $a_n = .95$ (5% change allowed in between each zone) equation (4.32) gives for TFTR

(4.33)

$$\left[T_o\left(1-\left(\frac{r_2}{r_o}\right)^2\right)+T_e\right]^{\frac{1}{2}} = .95\left[T_o\left(1-\left(\frac{r_1}{r_o}\right)^2\right)+T_e\right]^{\frac{1}{2}},$$

where T_o = 9950 eV, T_e = 50 eV, r_o = 85 cm and $r_2 > r_1$, (measured from the cylindrical axis). Algebraic manipulation of equation (4.33) yields

(4.34)

$$r_2 = \left[.9025\, r_1^2 + .0975\, r_o^2\left(1+\frac{T_e}{T_o}\right)\right]^{\frac{1}{2}} .$$

Starting with $r_1 = 0$ the iterative application of equation (4.34) provides the radii of a material zone structure. The temperature of the plasma to be placed in each homogeneous zone is then determined by an averaging process:

r_1 (cm)	T (eV)
0	8986
47.2	5923
61.8	4111
69.5	2905
74.7	1947
78.0	1213
81.6	847
82.4	647
83.3	447
84.1	249
85.0	

Table IV.6 The plasma zone structure generated from equation (4.34) for a_n = .95 in the TFTR plasma.

	Relative Density Attenuation	Average Energy of Outflux (eV)	Outflux Current (cm^{-2} sec^{-1})	Execution Time (sec) IBM 360/91
Convergence$_1$				
EPS = 10^{-1}	6.35×10^3	1832	3.09×10^{15}	35.58
EPS = 10^{-2}	5.46×10^3	1850	3.10×10^{15}	53.94
EPS = 10^{-3}	5.28×10^3	1854	3.10×10^{15}	75.24
EPS = 10^{-4}	5.25×10^3	1854	3.10×10^{15}	106.9
Zone Structure				
99 Uniform	5.17×10^3	1866	3.20×10^{15}	167.7
24 a_n = .95	5.14×10^3	1869	3.20×10^{15}	109.8
17 a_n = .90	5.12×10^3	1875	3.20×10^{15}	101.5
10 a_n = .85	4.99×10^3	1906	3.20×10^{15}	97.9

Table IV.7 Comparison of results for different convergence criteria and plasma zone structures for the TFTR plasma.

$$T_{21} = \int_{r_1}^{r_2} T(r)\, dr \Big/ (r_2 - r_1). \qquad (4.35)$$

For example, the zone structure generated with $a_n = .95$ (displayed in Table IV.6) is seen to contain 10 zones. The zone density is high near the outer plasma edge where the plasma temperature is low (i.e., the effective cross sections are large, see Figure 4.2). Close to the outer boundary uniform zones are used in all cases (a_n=.95,.90,.85) to avoid letting the zones become too small.

The result of using zone structures generated by equation (4.32) for values of a = .95, .90 and .85 are compared with the results of a uniform structure (99 zones in 85 cm) for TFTR in Table IV.7. The cases are run with 99 uniform spatial intervals, 31 groups, P_0-S_8, and EPS = 10^{-3} . The agreement in the results seems to indicate that the algorithm of equation (4.32) is a good one for choosing a zone structure. It is also seen that only about 10 material zones are required for a typical problem.

CHAPTER V

THE USEFULNESS OF MGDO NEUTRAL SOLUTIONS

The More Rigorous MGDO Method

From the discussion of Chapter III it is seen that the neutron MGDO methods can treat fully all aspects of the transport process (i.e., curved geometries, anisotropic scattering, detailed energy dependences, large attenuations, etc.). Even the effect of approximate weighting functions in the calculation of the multigroup cross sections can be mitigated by using a large enough number of energy groups. This is in contrast to the numerous simplifying approximations that have been introduced in previous neutral analyses to arrive at tractable solutions. These approximations are reviewed in the present section. Special attention is focused on the neutral transport module of the Düchs plasma code[8]. The effect of selected individual approximations on the MGDO method is also investigated.

Approximations Used in Previous Methods

The neutral transport equation (3.17) is not a trivial equation to solve. For realistic geometries with plasma temperature and density profiles the problem is even more complex. For determining gross descriptions of neutral atom behavior in plasmas, the rigor of most analyses (both

analytic and numeric) has been sacrificed for the convenience of a more managable solution technique. The common approximations are delineated in Table V.I for the neutral studies described in the first chapter. The approximations are discussed below.

It is recalled that the neutral transport equation (3.17) is given as

$$\underline{\Omega}\cdot\nabla\,\Phi + \sigma_a^{eff}(\underline{r},E)\,\Phi(\underline{r},\underline{\Omega},E) = Q(\underline{r},\underline{\Omega},E) + \int_{E',\underline{\Omega}'} \Phi(\underline{r},\underline{\Omega}',E')\,K_s^{eff}(\underline{r};E'\underline{\Omega}'\rightarrow E\underline{\Omega})\,dE'\,d\Omega', \tag{5.1}$$

where σ_a^{eff} is defined in equation (3.14) and K_s^{eff} from Equation (3.15) is

$$K_s^{eff} = N_i(\underline{r})\,\frac{h_i(\underline{r},E)}{4\pi v'}\,|\underline{v}'-\underline{v}|\,\sigma_{cx}(|\underline{v}'-\underline{v}|). \tag{5.2}$$

The transport equation can be written in any coordinate geometry for which the term $\underline{\Omega}\cdot\nabla\Phi$ and the element of solid angle $d\Omega$ are known [57], but the solution can be extremely complex. The slab approximation (planar geometry) provides the greatest simplification and is used by a majority of the authors cited in Table V.I. For analysis in tokamaks however, curvature effects can be significant [58,59]. The poloidal curvature can be taken into account by considering infinite cylindrical (one-dimensional) geometry which is

	Zubarev, et. al. [1]	Dnestrovskii, et. al. [4]	Rehker, et. al. [5]	Hogan, et. al. [6]	Clarke, et. al. [7]	Molvig [9]	Düchs, et. al. [8]
SIMPLIFIED GEOMETRY							
Slab Approximation	X	X	X	X	X		
Homogeneous Plasma			X		X	X	
ISOTROPIC SCATTERING	X	X	X	X	X	X	X
CROSS SECTION APPROXIMATION							
Charge Exchange	X	X	X	X	X	X	X
Ionization		X	X			X	X
APPROXIMATE ION DISTRIBUTION FUNCTION		X			X		X

Table V.1 A summary of approximations used in neutral transport studies.

done by Molvig [9]. This effect is partially included by the disk geometry of Düchs [8] (see Appendix C). It is possible to consider cylindrical geometry with standard MGDO codes and an application to full two-dimensional toroidal coordinates is proposed [59].

The isotropic scattering approximation of Table V.I used in all studies refers to the charge exchange scattering source term of equation (5.1). Given the form of the scattering kernel in equation (5.2) the integral (after the integration over $\underline{\Omega}'$) will, in general, still be a function of $\underline{\Omega}$. The solution of the transport equation can be greatly simplified, however, by effectively removing the $\underline{\Omega}$ dependence (i.e., leaving the source term isotropic in $\underline{\Omega}$). It is recalled that a physical condition that would justify the assumption of isotropy is that the charge exchange cross section be approximated as in equation (4.6). The use of equation (4.6) by the authors referenced in Table V.I is the basis of the isotropic scattering approximation. Equation (4.6) also introduces inaccuracy into the energy distribution of charge exchange neutrals since it is only an approximation (seen from the plot of the cross section in Figure 2.2). Common in MGDO codes (explained in Chapter III) is the technique of expanding the anisotropic scattering source in a Legendre series and retaining the important terms. In this way the angular dependence in scattering as well as the exact energy dependence of the charge exchange cross section is preserved. The

approximations utilized by the authors cited in Table V.I for the electron impact ionization rates are not as serious as those made for the charge exchange cross section and are therefore not detailed here.

The ion distribution function, h_i, appears explicitly in the expression for the charge exchange scattering kernel (equation (5.2)). It contains the majority of information as to the energy spectra of charge exchange neutrals. If the charge exchange cross section varied strictly as 1/v, the source neutrals would assume the distribution h_i. The potentially complex energy treatment of the transport equation can be reduced by choosing h_i so that the energy variable can be conveniently integrated out of equation (5.1). This is done by the references indicated in Table V.I by approximating h_i as a delta function, $\delta(E-kT_i)$, at the local plasma temperature. The advantage of MGDO methods is that an arbitrary isotropic distribution function can be considered.

Because of its important repetitive application in the widely used plasma simulation code, the Düchs neutral transport procedure is now described in more detail. We later judge the seriousness of the combined approximations by a comparison with the more exact MGDO method. Appendix C starts with the integral form of the Boltzmann equation and derives, through a consideration of geometry, energy and angle variables, the approximate Düchs neutral transport equation. Only a summary of the various approximations and

their expected effects are given here.

As indicated in Table V.I isotropic scattering is assumed (equation (C.9)), however, its precise justification is not given. The charge exchange cross section is approximated, but not as "1/v" which has given rise to isotropy in other analyses. Below ion energies of about 10 keV, therefore, the tendency to backscatter slightly will be nullified.

The treatment of the energy variable assumes that the ion distribution function h_i is monoenergetic (equation (C.11)) at the local ion temperature (kT_i). The energy distribution of neutrals is also assumed to be monoenergetic given by an average over the energy of the neutrals that arrive at the point in question (equation (C.14)). This modal approach is convenient but implies that the character of all aspects of energy transfer (charge exchange and ionization) can be approximated with averaged Maxwellian parameters.

In an attempt to include poloidal curvature effects the Düchs analysis is done in a one-dimensional disk (the geometry formed by a perpendicular slice from an infinite cylinder). Fixed and scattering sources originating from the third dimension (in the toroidal or axial direction) are only approximated. We show in Appendix C however that it is possible to include the axial dimension in cylindrical geometry exactly by a simple integration over the axial variable. This leads to only a minor modification in the

transport attenuation term but the effects are significant.

The numerical solution technique of the Düchs module introduces another source of error. The integral transport equation is solved iteratively (Appendix C) for "generations" of charge exchange neutrals (actually successive scattering sources). For this reason the Düchs treatment is referred to as the generation method. If not enough generations are included in a run then the neutrals are not able to distribute themselves sufficiently in the plasma. The truncated solution does not represent a true solution for an optically thick plasma. The effects of this approximation are noted later in this chapter.

Effects of Approximations

It is worthwhile to discuss the kinds of effects that can be expected from the approximations in Table V.I. Because of the versatility of the MGDO method it is possible to employ some of the approximations and then treat the same problems in a more exact manner. This is done for isotropic scattering, a "1/v" dependence for the charge exchange cross section and the slab geometry assumption.

The effect of the anisotropic charge exchange scattering source has been explored fully in Chapter IV. The restriction to isotropic scattering was found not to be serious in tokamak plasmas for temperatures less than 10 keV (Figure 4.1). This is due to the combination of several factors. First, σ_{cx} is a slightly decreasing function of

velocity which counteracts the increasing $|\underline{v}-\underline{v}'|$ in equation (4.6). Secondly, charge exchange (scattering) is the dominant reaction mechanism in tokamak plasmas (E < 20 keV), and not ionization, which would yield an anisotropic flux distribution far from a localized source. Thirdly, for an inhomogeneous Maxwellian plasma the majority of charge exchange collisions occur between particles that have much different velocities (v'>>v or v>>v') which minimizes the anisotropic effect (see equation (4.10)).

The charge exchange cross section has often been approximated as

$$\sigma_{cx} \sim \frac{C}{|\underline{v}'-\underline{v}|} \quad cm^2$$

in the references cited in Table V.I, where C is a constant ($cm^3\ sec^{-1}$). The actual reaction product (σv) (where $v = |\underline{v}'-\underline{v}|$), is plotted in Figure 5.1 and is seen not to be uniform in energy. We examine the effect of the approximation by choosing several different values of the constant C and comparing the results for neutral transport in the TFTR plasma described in Chapter IV. As seen in Table V.2 increasing the charge exchange strength (from a low value $C = 4 \times 10^{-8}\ cm^3\ sec^{-1}$ to $C = 14 \times 10^{-8}\ cm^3\ sec^{-1}$) increases the neutral outflux. Since the reactions will tend to occur closer to the source (edge of the plasma where

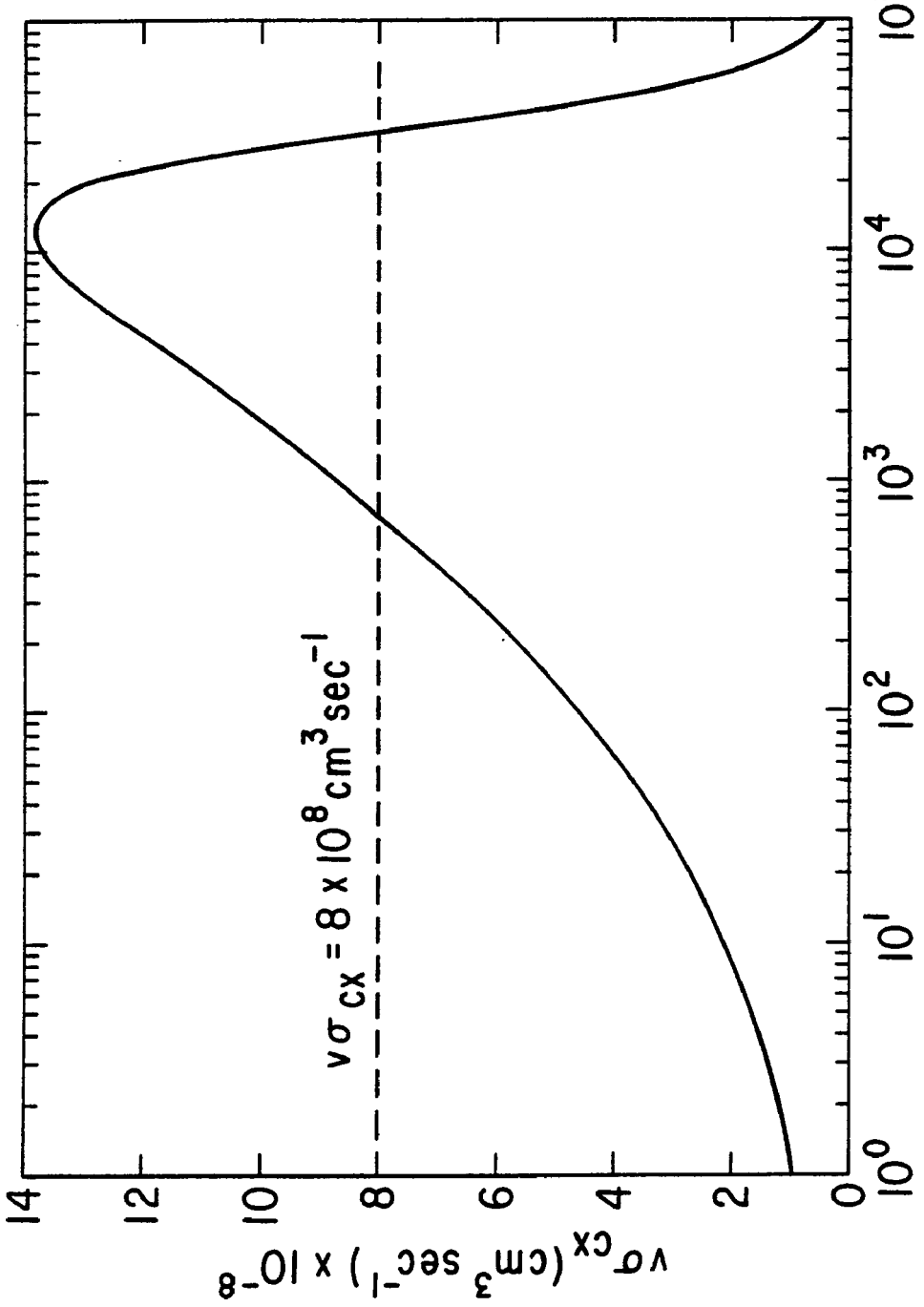

Figure 5.1 The charge exchange reaction product ($v\sigma_{cx}$ cm^3 sec^{-1}) vs. hydrogen atom energy.

	Relative Density Attenuation	Average Energy of Outflux (eV)	Outflux Current (cm^{-2} sec^{-1})	Execution Time (sec)
Rate (cm^3 sec^{-1})				
$v_{rel}\sigma_{cx}(v_{rel})$	5.29×10^3	1854	3.10×10^{15}	75.24
$C = 14 \times 10^{-8}$	4.27×10^3	1678	3.06×10^{15}	49.32
$C = 8 \times 10^{-8}$	3.55×10^3	1802	2.42×10^{15}	38.76
$C = 4 \times 10^{-8}$	3.40×10^3	1856	1.67×10^{15}	30.84
$v_{rms}\sigma_{cx}(v_{rms})$	5.50×10^3	1845	3.11×10^{15}	55.20
Geometry				
$N_i = 1\text{-}5 \times 10^{12}$ Slab	1.69×10^2	6110	4.00×10^{15}	26.88
Cylinder	1.59×10^2	4501	4.44×10^{15}	47.22
$N_i = 1\text{-}5 \times 10^{13}$ Slab	1.07×10^4	1877	2.93×10^{15}	47.70
Cylinder	5.29×10^3	1854	3.10×10^{15}	75.24
$N_i = 1\text{-}5 \times 10^{14}$ Slab	5.13×10^{13}	435	2.19×10^{15}	79.32
Cylinder	1.30×10^{13}	435	2.20×10^{15}	108.8

Table V.2 (Upper block) Effects of approximations for the charge exchange reaction product on neutral transport in the TFTR plasma. Line 1 results are generated with no approximations. (Lower block) Comparison of results using slab geometry for the TFTR plasma.

the ion temperatures is lower) the outflux energy is also lower. The deviations from the exact case (line one in Table V.2) are significant, especially since the neutral sputtering rate is directly proportional to the outflux and is a function of the outflux spectra. As a special case, the exact reaction rate is approximated as

(5.3)

$$|\underline{v}' - \underline{v}|\, \sigma_{cx}(|\underline{v}' - \underline{v}|)\, d\mu_o \sim 2\, v_{rms}\, \sigma_{cx}(v_{rms}),$$

where $v_{rms} = \left[v'^2 + v^2\right]^{1/2}$ is the average root-mean-square velocity between two isotropic monoenergetic distributions. The results are seen to be in good agreement with line 1 which confirms that σ_{cx} is a slowly varying function (mean velocities can be used).

Most one-dimensional MGDO neutron transport codes allow the options of several solution geometries. The effect of geometry in modeling neutral transport is judged by comparing the slab and cylindrical cases in Table V.2. Three plasma density profile regimes are considered for the TFTR plasma. At low densities the geometry effect is more pronounced for the outflux characteristics (energy and current) while at high densities the greatest difference is in the neutral attenuation (~ factor of five). This corroborates the prediction of Dnestrovskii [4] that for optically thick plasma differences between cylindrical and slab calculations will only be large on the plasma axis

where the neutral density is low. At realistic densities (N_i = 1-5 x 10^{13} cm^{-3}) agreement is relatively good for the outflux parameters but the factor of two difference in attenuation is significant in this case. It is recommended then that at least cylindrical geometry be used for tokamak neutral transport. The effects of additional toroidal curvature should not be as great as that seen for poloidal curvature [58].

A Benchmark Problem

From the discussion of the previous section MGDO methods should provide a more accurate neutral transport solution than obtained earlier in other analyses; fewer approximations are utilized. It is natural then that the MGDO method can be used as a reference benchmark to determine the effect of these approximations. This was done for individual cases in the previous section but the outcome of their collective application has yet to be investigated. This can only be done by a direct comparison between complete methods. The present section therefore presents the results of a comparison between the MGDO method and the widely used Düchs neutral transport module (generation method). The sources and implications of the observed discrepancies are also given.

Comparison Study

The MGDO neutral-plasma model that will be used for the comparison study was presented in Chapter IV. It is recalled that Franck-Condon neutral hydrogen atoms (~ 3 eV) are incident isotropically at the plasma boundary. The generation method models the plasma as being confined by a physical limiter at which point isotropic source neutrals (~ 3 eV) are incident. The source conditions are therefore the same. The generation method also assumes that all outfluxed neutrals and ions are collected at the boundary so that in the next iterative time step a recycling balance may be maintained by allowing an appropriate number of neutrals (at the source energy) to return [8]. This is equivalent to imposing a vacuum boundary condition in determining the steady state neutral profile. The MGDO runs for the comparison study therefore also assume vacuum boundary conditions.

As a basis for comparison, two test cases are chosen. Shown in Figure 4.4(a) and (b) are "snapshot" plasma profiles of the ST and TFTR tokamaks. The profiles are of the form given in equation (4.23) with the constants (displayed in Table IV.I) chosen to typify experimental and design data for the ST and TFTR machines respectively. The choices are made to determine if the effects of plasma temperature, density and size will modify the relative performance of the two methods. A good indication of the difference in quality of the plasma is given by the

parameter ρ (the number of neutral collision mean free paths in the plasma, defined in Appendix C, equation (C.4)). For ST we calculate (using average values) $\rho \sim .8$ while for TFTR $\rho \sim 3$.

The selection of an MGDO (ANISN) operating mode was guided by the parameter sruvey results of Chapter IV. To ensure the accuracy of the ANISN runs in providing the benchmark solutions "conservative" parameters are chosen: 31 energy groups (equal logarithmic spacing), P_o (isotropic) scattering expansion, S_8 angular quadrature and a convergence criteria of EPS = 10^{-3}. Throughout the study it was observed that neutral transport was highly sensitive to plasma conditions near the neutral source (the plasma edge in this case), since the first charge exchange neutrals originate in this region. To eliminate the possibility of discrepancies arising from this effect in the comparison runs, the plasma zone (temperature and density) structure used for ANISN was chosen to be the same as that determined by the standard Düchs code. This is a uniform 99 spatial interval structure with a corresponding 99 material zones. From the parameter survey 60 spatial intervals and 10 material zones were found to be sufficient so the present choice of structure is more than adequate. A summary of MGDO and generation method operating parameters is given in Tables V.3 and V.4.

Neutral densities as a function of plasma radius are displayed in Figure 5.2 for the ST and TFTR machines. The

	ST	TFTR
Geometry	Infinite Cylinder	Infinite Cylinder
Minor Radius (cm)	14	85
Spatial Intervals	99	99
Temperature Zones	99	99
Plasma Temp. $T_e = T_i$ (eV) [On axis	4.99×10^2	9.99×10^3
Plasma Temp. $T_e = T_i$ (eV) [At edge	2.08×10^1	2.49×10^2
Plasma Density $N_e = N_i$ (cm^{-3}) [On axis	3.00×10^{13}	4.99×10^{13}
Plasma Density $N_e = N_i$ (cm^{-3}) [At edge	3.56×10^{12}	1.12×10^{13}
Nominal Energy of Source Neutrals (eV)	3	3
Order of Scattering Expansion	0 (Isotropic)	0 (Isotropic)
Order of Angular Quadrature	8	8
Energy Groups	31	31

Table V.3 Summary of parameters for the MGDO code ANISN in the comparison study.

		ST	TFTR
Geometry		Planar Disk	Planar Disk
Minor Radius (cm)		14	85
Spatial Intervals		99	99
Temperature Zones		99	99
Plasma Temp. $T_e = T_i$ (eV)	On axis	4.99×10^2	9.99×10^3
	At edge	2.08×10^1	2.49×10^2
Plasma Density $N_e = N_i$ (cm^{-3})	On axis	3.00×10^{13}	5.00×10^{13}
	At edge	3.56×10^{12}	1.12×10^{13}
Nominal Energy of Source Neutrals		3	3
Charge Exchange Generations		10	10
Reporting Energies		10	10

Table V.4 Summary of parameters for the generation method in the comparison study.

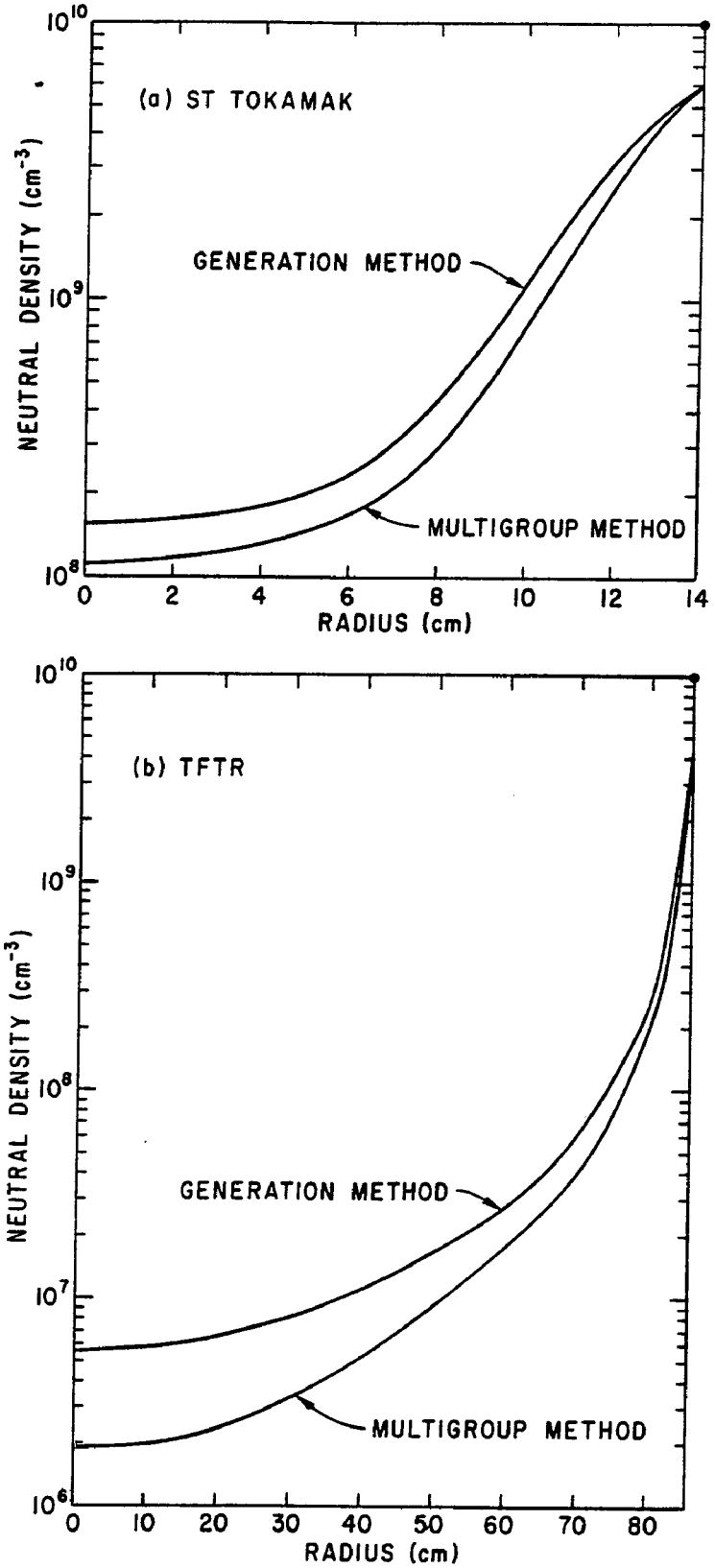

Figure 5.2 Calculated hydrogen atom densities for the (a) ST and (b) TFTR tokamaks vs. distance from the cylindrical axis. The results are normalized to a neutral edge density of 1×10^{10} cm^{-3}.

MGDO results are seen to be consistently lower than the generation method, reaching a maximum discrepancy of about a factor of three on the TFTR axis. The ST densities differ by no more than 50%. We have chosen as the normalization a neutral atom edge density of 1×10^{10} cm^{-3} (equivalent to a neutral gas (H_2) pressure of $\sim 1.5 \times 10^{-7}$ Torr at T = .025 eV) which is fairly typical of present day discharges. The density in the plasma drops almost immediately to about one half that value, since only ~50% of the isotropic distribution has a velocity component directed into the plasma. Both neutral density profiles are predominantly concave upward. This results from an increase in ionization mean free path as the average velocity of the neutrals rises (from charge exchange collisions with more energetic ions) faster than the plasma density increases. Below 100 eV, however, the electron impact ionization rate increases with electron temperature, reducing the previous trend and explaining the roll over (concave downward) of the neutral density near the ST edge. No such inflection is seen for the TFTR case where the plasma edge is above 200 eV.

The lack of agreement between the two methods can be partially accounted for in at least two ways. The generation method converges poorly for the TFTR case. A significant number of neutrals (~ 1/2 the total present at the axis) are found to build up in the tenth and final charge exchange generation. The code implementation does

not permit these neutrals to charge exchange further. The effect may be to enhance the actual neutral density by shortening the lifetime a neutral may have to undergo ionization in the plasma. For the ST case the plasma was optically thin enough so that only a few charge exchange generations were required to reach a converged solution. It will be recalled (Appendix C) that Molvig [9] has pointed out that there may be difficulty in arriving at sufficiently converged solutions for $\rho >> 1$. The solutions we have seen for TFTR ($\rho \sim 3$) and ST ($\rho \sim .8$) seem to bear this out. The MGDO method exhibits good convergence for all cases considered.

Another factor that contributes to the observed discrepancies is the exponential approximation to the Ki_1 function (as the cylindrical integral attenuation term) employed in the generation method (see Appendix C). For $\rho > .7$ the exponential approximation increasingly underestimates the attenuation. This would eventually lead to an overestimate of the neutral density which is consistent with the results we present here.

A summary of neutral results appears in Table V.5 where G refers to the generation method and M to multigroup. We see that the outfluxes (currents) of charge exchange neutrals at the boundary differ by as much as 40% while the average energies of the corresponding spectra are in reasonable agreement. That this is so can be seen from plots of the actual spectra in Figures 5.3 and 5.4. We

		ST	TFTR
Neutral Density at Edge (cm^{-3})		1.0×10^{10}	1.0×10^{10}
Neutral Density on Axis (cm^{-3})	G	1.57×10^{8}	5.59×10^{6}
	M	1.10×10^{8}	1.93×10^{6}
Outflux Current of Neutrals (cm^{-2} sec^{-1})	G	4.10×10^{15}	4.53×10^{15}
	M	3.12×10^{15}	3.25×10^{15}
Average Energy of Outflux (eV)	G	321	1879
	M	302	1865
Power of Outfluxed Neutrals (kW)	G	11.9	1211
	M	8.46	864
Total Sputtering Rate (cm^{-2} sec^{-1}) Normal Incidence	G	1.47×10^{12}	1.04×10^{13}
	M	1.04×10^{12}	$.69 \times 10^{13}$
Total Sputtering Rate (cm^{-2} sec^{-1}) Angular Incidence	G	1.73×10^{12}	1.67×10^{13}
	M	1.79×10^{12}	1.49×10^{13}
Execution Time IBM 360/91 (sec)	G	~ 6	~ 6
	M	~ 120	~ 170

Table V.5 Summary of neutral transport results for the comparison study. (G = generation method, M = multigroup method). The calculations are normalized to a neutral edge density of 1×10^{10} cm^{-3}.

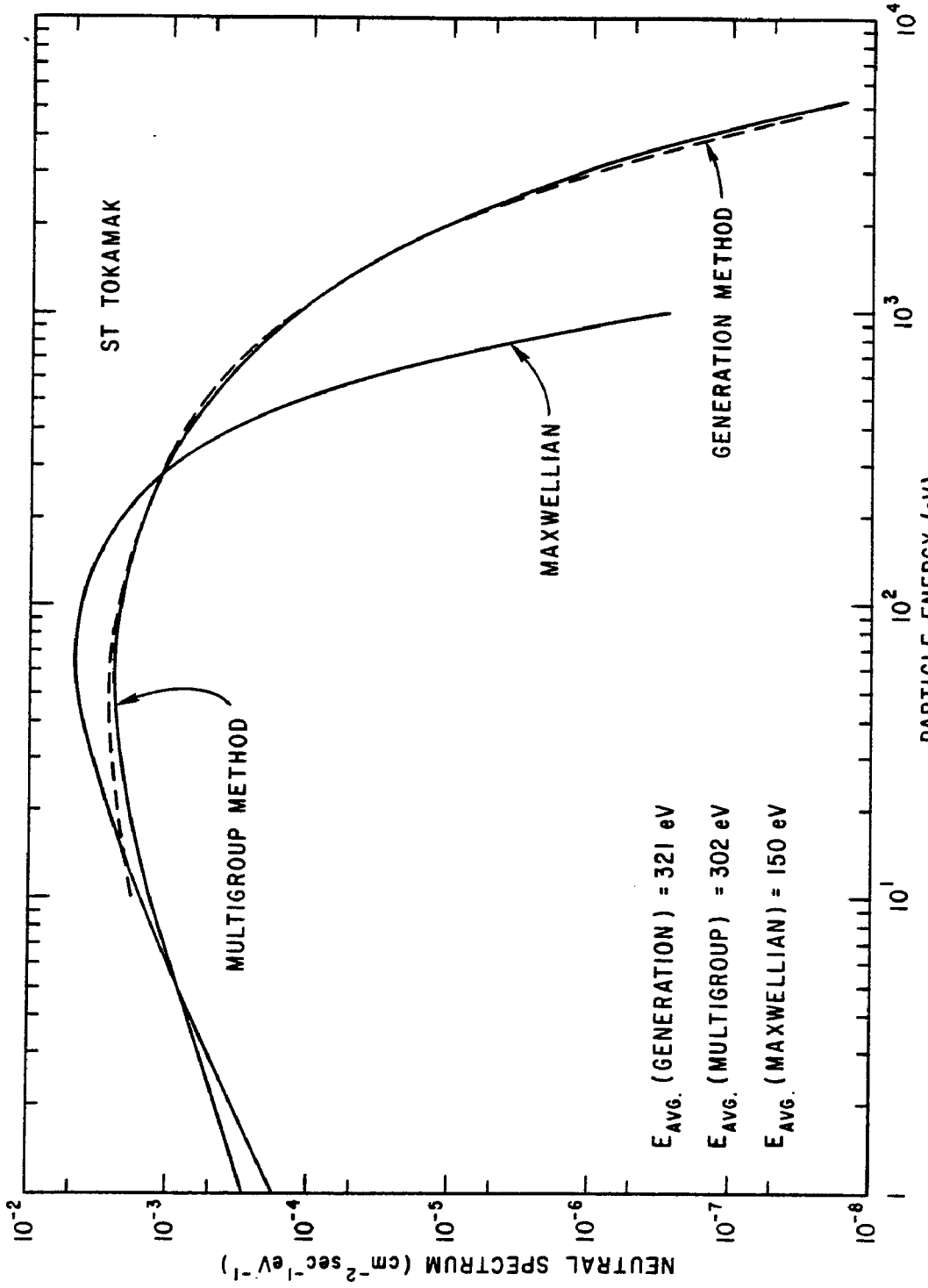

Figure 5.3 The spectrum of outfluxed charge exchange neutrals at the outer boundary (r=14 cm) of the ST tokamak vs. hydrogen atom energy. The total outflux is normalized to 1 $cm^{-2}sec^{-1}$.

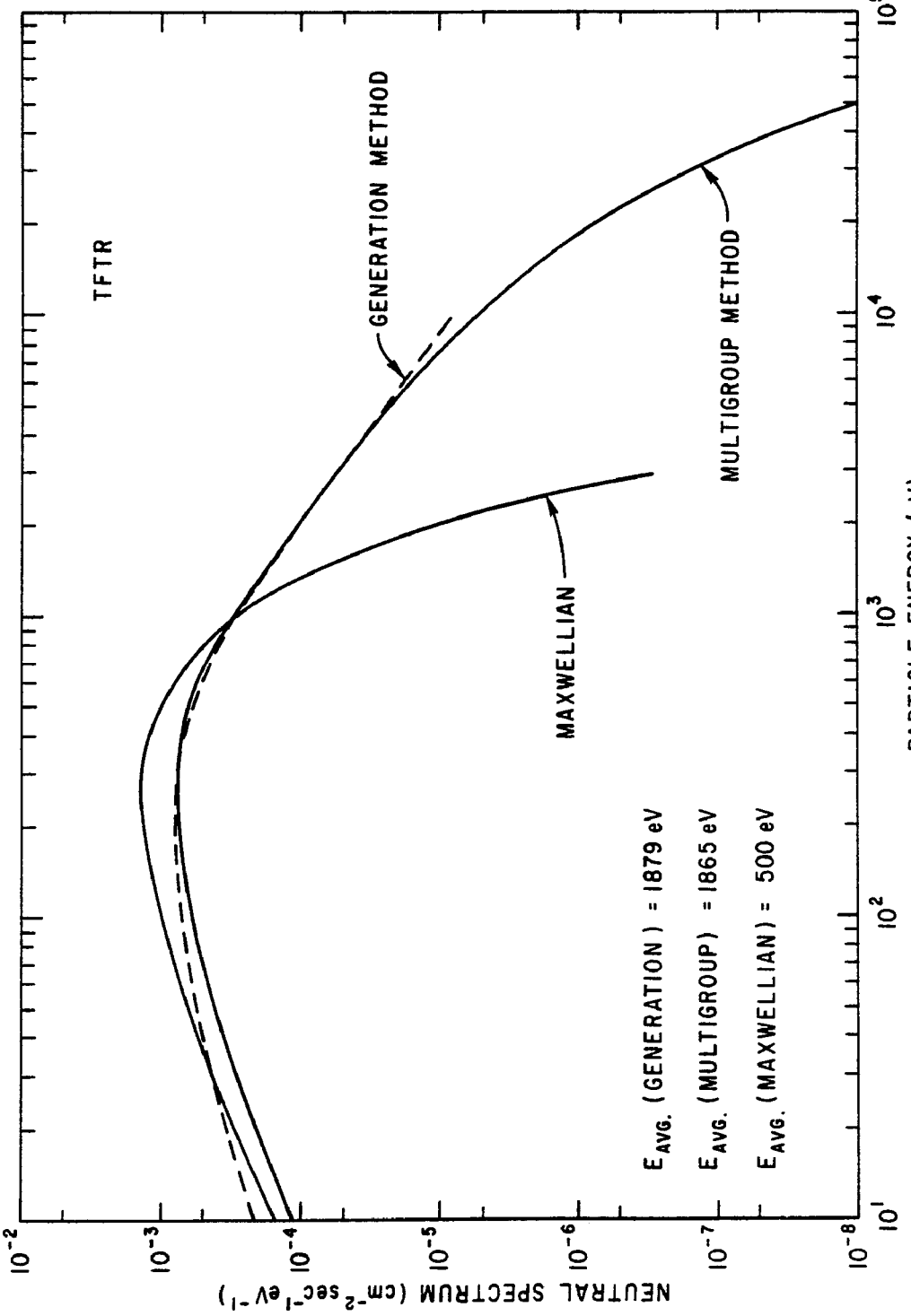

Figure 5.4 The spectrum of outfluxed charge exchange neutrals at the outer boundary (r=85 cm) of the TFTR tokamak vs. hydrogen atom energy. The total outflux is normalized to 1 $cm^{-2}sec^{-1}$.

superimpose a Maxwellian flux distribution peaking at about the same energy as that of the spectra to gauge relative shape. The outfluxes are obviously not Maxwellian, exhibiting a lower energy component characteristic of the plasma edge temperature (close to the actual Maxwellians drawn) and a higher energy tail indicative of the ion distribution in the plasma interior. The high energy tail neutrals have been observed experimentally and constitute a means of measuring plasma ion temperatures [18]. The same general spectral shapes have been noted by other authors [6,11].

The CPU times on an IBM 360/91 for the test cases are displayed in Table V.5. This aspect of neutral module performance is relatively important. For example, for a plasma simulation run by the Duchs code, about 80% of the total run time is devoted to calculating the evolving neutral density [60]. It is recalled, however, that the ANISN runs for the comparison cases were made with "conservative" operating parameters and an overspecified spatial interval and material zone structure. Relaxation of these conditions along with the application of several other techniques will be shown later in this chapter to greatly reduce the MGDO execution times.

Implications of Results

The primary purpose of the generation treatment is to calculate steady state neutral atom profiles as an integral part of a larger plasma simulation code. The neutral

calculation is done every few time steps as the plasma distribution evolves. We therefore discuss the significance of the results we have seen with this purpose in mind.

The duration of a present day tokamak discharge is typically several times that of the average particle confinement time. For example, for the ST experiment, particle confinement times reaching a maximum of 13-14 msec were reported for discharges lasting at least 50 msec [12]. Since the plasma density remains roughly constant for a large portion of the discharge, the implication is that the plasma outflux is recycled at the boundary, presumably as "cold" neutral hydrogen. The same recycling behavior is expected to be seen in future machines. In the computer modeling of this process, the rule is usually chosen that the cold neutral influx should match the total particle outflow at the plasma edge. Due to problems in implementing the balance, however, the total number of plasma particles is not held constant to better than about 10% in a computer run, which is considered adequate [8]. For a typical ST discharge the total particle outflux is divided about equally between charged particles and neutrals [11]. The 30% greater neutral outflux level (see Table VI.5) predicted by the generation method will therefore overestimate the total particle outflux by a factor of 15%.

The total outfluxed power carried by neutrals, shown in Table V.5, shows a similar trend. Charge exchange losses in ST are comparable to those of radiation (each about 25% of

the total losses) [18]. Therefore the additional 40% neutral power loss given by the generation method represents an increase in total power outflux by about 10%. Experimentally determined typical charge exchange power losses for the ST tokamak are estimated by Hinnov [11]. If both the generation and multigroup results are scaled separately to neutral source densities that yield his reported outflux level (2.4×10^{16} cm^{-2} sec^{-1}) then Table V.6 is derived. Both methods are seen to agree well with this experimental observation.

It will be recalled that the greatest deviations between the generation and MGDO methods occurred for the calculation of the neutral density (see Figure 5.2). The discrepancy will have a pronounced effect for a beam heated system (see Chapter I). The probability of charge exchange of a hot beam ion is directly proportional to the background neutral density. The ensuing hot neutral, if it escapes from the system, takes with it nearly all the energy of the original beam neutral. In the case of the ATC tokamak [61] calculations show that the surface energy loss due to this mechanism is an order of magnitude greater than that due to escaping background neutrals [20] . More importantly this represents ~50% of the original beam injected power and over 30% of the total input power. ATC plasma characteristics are not unlike those of the ST tokamak (e.g., a ~ 17 cm, T_{imax} = 420 eV for the beam injection phase). For a computer simulation of ATC therefore, a 30% overestimation

	ST, Outfluxed Power (kW)
Hinnov (Experimental Observation)	70
Generation	69.6
Multigroup	64.9

Table V.6 Charge exchange power loss for the ST tokamak (kW), with both calculations normalized to an outflux level (experimentally observed, Hinnov [11]) of 2.4×10^{16} cm^{-2} sec^{-1}.

of the beam charge exchange outflux due to an increased neutral population throughout the plasma (as implied from the results of Figure 5.2(a)) would be significant.

Perhaps that most deleterious effects neutrals have on tokamak operation are the first wall sputtering caused by the fast charge exchange neutral outflux and the resulting introduction of the sputtered impurities into the plasma. The fitted energy-dependent sputtering yield curve of Meade [62] is multiplied by the calculated neutral outflux to obtain the sputtering rates presented in Table V.5. The neutrals are incident on a stainless steel vacuum wall located at the outer boundary. In general the MGDO sputtering rates are lower, with most of the difference accounted for by lower outflux levels.

An interesting trend is seen when the entries labelled Normal Incidence are compared with those labeled Angular Incidence. The former assume the sputtering yield is independent of angle, and are calculated using Meade's normal incidence curve for all angles. However, the theory of Sigmund [63] predicts that the sputtering yield should be approximately proportional to $1/\cos\theta$ where θ is the angle from the surface normal. (This theory is supported by measurements by Summer [64] of sputtering by 12 keV D+ on niobium.) When this angular dependence is included in the calculation there are pronounced effects on sputtering rates. If the calculated angular distributions of neutrals at the wall were identical a uniform increase would be

expected. As it is, MGDO results increase by ~ 70% and ~ 115% for the ST and TFTR cases respectively while there are ~ 18% and ~ 61% increases given by the generation method. The effect is greater for the MGDO method because the $1/\cos\theta$ term increases the weights of neutrals with angles closer to a grazing incidence; these are present in greater proportion in the MGDO solution. This is because many neutrals originate from directions down the length of the cylinder and from volumes close to the surface (from first generation charge exchange) that are not considered explicitly in the 2-D disk geometry of the Düchs code. The angular sputtering effect is larger for the TFTR plasma than for the ST, because the increased density and temperature leads to enhanced formation rates of charge exchange neutrals close to the wall surface. Of final note is the increase in the sputtering rates, with or without the angular term, from the ST to TFTR machines. Although the neutral outfluxes are comparable, the harder TFTR spectrum is distributed closer to the sputtering yield peak (~ 4 keV), which accounts for the order of magnitude difference.

The conclusion that we draw from the benchmark comparison study is that the approximations used in the generation method introduce a large enough error in the neutral transport calculation as to have a significant effect for a neutral module application.

Neutral Module Application

The use of the MGDO method as a comparison benchmark has provided useful information as to the magnitude of errors associated with the neutral module of the Düchs plasma simulation code (generation method). A further and more significant application, though, would involve the use of the MGDO method as a neutral module itself. In this type of application an important consideration is execution time, since about 80% of the total Düchs code run time is taken up by the neutral calculation. The MGDO runs for the comparison study were "conservative" in their operating parameters to assure an accurate and meaningful benchmark; this led to run times at least a factor of 20 longer than the generation method. The present section explores the possibility of reducing these run times while maintaining calculational accuracy to a point where the MGDO method might be attractive as a neutral module. This is first done by relaxing MGDO operating parameters and then introducing several auxiliary time reducing techniques.

Reduction in Operating Parameters

With the equal logarithmic energy structure, 31 groups resulted in no perceptable change from the 50 group results (see Table IV.2), and the 11 group case gave a 15% discrepancy. It was also discovered that as few as 29 spatial intervals could be used for TFTR analysis, provided that a small enough mesh was chosen near the boundary. The effect of the higher order scattering approximations were

found to be negligible (Table IV.5) and S_4 angular quadrature was thought to be sufficient for most applications (Table IV.5). The only exception to this would be when detailed resolution of the angular flux is necessary (e.g., sensitive angular dependent sputtering yields or particle reflection coefficients). The relaxation of the ANISN convergence criteria up to values of EPS = 10^{-1} were found not to have a strong effect on calculated results (Table IV.6). Finally, if the material (plasma) zone structure was constructed according to the collision mean free path criteria then as few as 10 zones were required for the TFTR cases.*

The results of the 10 temperature zone case are first compared with the benchmark TFTR in Table V.7 and then a full relaxed operating parameter case is considered (in line 3). Here we use 10 temperature zones, 28 spatial intervals, 11 energy groups, and choose P_o scattering, S_4 angular quadrature and EPS = 10^{-2}. The relaxed case thus follows the recommendations of the parameter survey for limiting execution time. The reduction is seen to be dramatic (by close to two orders in magnitude). The agreement with the benchmark is to within ~ 20% but more importantly the relaxed ANISN case introduces less error than the generation

*An advantage of the MGDO method is that the plasma zone and spatial mesh structures can be chosen separately.

	Relative Density Attenuation	Average Energy of Outflux (eV)	Outflux Current (cm^{-2} sec^{-1})	Sput. Rate Normal Inc. (cm^{-2} sec^{-1})	Outflux Power (kW)	Execution Time (sec)
Benchmark	5.17×10^3	1866	3.20×10^{15}	6.82×10^{12}	853	167.7
10 Plasma Zones	4.98×10^3	1906	3.21×10^{15}	6.87×10^{12}	875	97.9
Relaxed Operating Parameters	4.78×10^3	2255	3.27×10^{15}	7.71×10^{12}	1054	2.28
Line 3 with Restart and Limit = 1	4.71×10^3	2257	3.27×10^{15}	7.71×10^{12}	1053	1.14
Generation	1.79×10^3	1879	4.51×10^{15}	10.3×10^{12}	1212	~ 6

Table V.7 Comparison of time reduction runs for the TFTR plasma performed with ANISN.

method (line 5). This is especially true (and significant) for the relative neutral attenuation and the calculated sputtering rates. At its present level the MGDO method is a factor of 3 faster than the generation method. The limitation of operating variables in ANISN has thus been shown to maintain the accuracy of the MGDO method while allowing its competitiveness (in execution time) as a neutral module.

Supplemental Time Reduction Techniques

Several "artificial" techniques allow further significant time reduction.

A reverse labeling scheme for the energy group structure accelerates code convergence. The conventional (neutron analysis) description gives the highest energy group the label "1". In neutron transport the predominant energy transition is downscatter and the MGDO codes make use of this fact in sweeping from high to low energy groups during an outer iteration to maximize the efficiency. The transport of edge source neutral atoms into a plasma on the other hand is dominated by upscattering (i.e., charge exchange with more energetic plasma ions) and therefore the advantage is lost. If the group labeling is reversed, however, scattering is once more from low to high group number, and a savings in iteration time can be realized. Shown in Table V.8 are the results of forward and reverse structure runs for the TFTR plasma. At a "loose" convergence level (EPS = 10^{-1}) not only are the time savings

	Relative Density Attenuation	Average Energy of Outflux (eV)	Outflux Current (cm^{-2} sec^{-1})	Execution Time (sec)
EPS = 10^{-2}				
Foward	5.66×10^{3}	1850	3.09×10^{15}	65.9
Reverse	5.46×10^{3}	1850	3.09×10^{15}	53.9
EPS = 10^{-1}				
Foward	7.87×10^{3}	1797	3.17×10^{15}	65.7
Reverse	6.33×10^{3}	1832	3.09×10^{15}	35.6
Normal Run	5.28×10^{3}	1854	3.10×10^{15}	75.2
Restart from Different Case	5.31×10^{3}	1854	3.10×10^{15}	64.4
Normal Run	4.90×10^{3}	1953	3.24×10^{15}	82.9
Restart from Close Case	4.90×10^{3}	1953	3.24×10^{15}	44.4
Normal Run	5.30×10^{3}	1854	3.10×10^{15}	81.2
Restart from Same Case	5.25×10^{3}	1854	3.10×10^{15}	25.4
31 Groups				
Unlimited	5.28×10^{3}	1854	3.10×10^{15}	75.2
Limit = 1	5.28×10^{3}	1854	3.10×10^{15}	51.3
11 Groups				
Unlimited	4.85×10^{3}	2185	3.15×10^{15}	16.9
Limit = 1	4.83×10^{3}	2186	3.14×10^{15}	8.9

Table V.8 Comparison of foward and reverse group structure results, cases started with various flux approximations, and the effect of the inner iteration limit on neutral transport in the TFTR plasma.

significant (~ 50%) but the reverse structure also provides results that are closer to the tighter convergence runs (EPS = 10^{-2}). As more outer iterations are used (for EPS = 10^{-2}), and thus a greater number of scattering collisions are accounted for, the discrepancy in results between the two structures decreases, as does the difference in execution times. The reverse group structure has already been incorporated into the benchmark and time reduction runs of the previous section and will be used implicitly for the remainder of this investigation.

Time to a converged solution can also be decreased by starting the ANISN iteration procedure with a good initial flux guess (see Chapter III). A minimum amount of time should be required, for example, when iteration is started with an "exact" answer and conversely a much longer time needed when the initial guess is arbitrary (e.g., usually chosen as zeroes). This is seen in the sample runs displayed in Table V.8. The lines labelled "Normal Run" start with a standard zero flux guess and the same case restarted from various flux guesses follow. The first restart (line 6) is made from the flux solution to a problem where the plasma temperatures are about 50% of those of the test case and is thus a relatively poor guess. Nonetheless, there is a significant savings in execution time of ~15%. A good flux guess (from a similar case, where only the edge temperatures are different) leads to a calculational savings of close to 50% in line 8. A restart from the already

converged solution (line 10) represents a maximum in computation time to be expected from this technique (~ 65%). In a neutral module application the neutral transport calculation is done every few plasma time steps. Thus, a neutral flux solution is available from a previous case that will have very similar plasma conditions to the one currently being considered. In this situation it is expected that the reduction in execution time will be somewhere between the first two cases considered in Table V.8 (20 - 50%).

Another method that has proved successful in reducing run times is that of artificially limiting the number of inner ANISN iterations. It is recalled (Chapter III) that the inner iteration process continues until consecutive self-scatter collision sources agree to within a specified tolerance. This normally requires only 2-3 passes. Self-scatter (within group scattering) in the neutral system requires that charge exchange take place between ions and neutrals with approximately the same velocities. However, the likelihood of this event in an inhomogeneous Maxwellian plasma has been shown to be small (Chapter IV). The contribution of self-scatter to the total scatter process is therefore minimal. Additional inner iterations beyond an initial pass have proved to to have negligible effect on the outcome of results except for a drastic reduction in the convergence time. Table V.8 displays two cases where this is exemplified. In a 31 energy group analysis for the TFTR

plasma the savings is seen to be 33% (line 12) while for an 11 group case it is close to 50% (line 14). Virtually no change is noted in the results. The limitation of iterations in early convergence loops in neutron analysis is a common practice.

The two additional time reduction techniques (an initial flux guess and the inner iteration limit) are applied to the ANISN relaxed parameter case (TFTR) of the previous section and the results are shown in Table V.7 (line 4). The starting flux guess comes from a case where the plasma temperatures have been reduced by 20%. Changes in temperatures $\leq$ 20% are expected between consecutive calculations of neutral transport in a module application. The total time savings is seen to be 50% while the results are unchanged and thus they still represent a more accurate neutral transport description than the generation method (line 5). The MGDO run is now a factor of ~6 faster than the generation method and has been reduced by over two orders of magnitude from the original benchmark problem. An additional consideration that must be made is the time required to generate the multigroup cross sections (using the code GIMUXS, Chapter IV). For the relaxed operating parameter problem (10 material zones, 11 energy groups), this ranges from 3-5 seconds, making the total MGDO run about 4-6 seconds. In a neutral module application it should be possible to maintain a large material (plasma temperature) library that could provide many previously

generated cross section sets for the current use. This would thus lower the time needed for the total MGDO run.

From the above discussion it can be concluded that the MGDO method (ANISN) represents a viable alternative to a present neutral module technique (the Düchs generation method). The accuracy of the calculation is improved and the computation time is competitive. The specialization of the MGDO method for this purpose is not expected to present any serious problems.

CHAPTER VI

CONCLUDING REMARKS

The feasibility, practicality and usefulness of MGDO neutron transport methods for the analysis of neutral atom transport in a tokamak plasma have been investigated.

Through a detailed consideration of neutron and neutral behavior it was determined that interactions, sources and boundary conditions for the respective species could be regarded as analogous. A straightforward derivation of the neutral transport equation followed which verified the similarity of the two transport processes. The techniques developed for the solution of the neutron Boltzmann transport equation were therefore determined to be applicable to the neutral transport problem. A convenient and reliable MGDO numerical method (ANISN) was chosen to test this hypothesis.

A computer code, GIMUXS, was developed to efficiently generate the appropriate neutral multigroup cross sections. The code features the ability to consider arbitrary plasma temperatures and includes both ion and electron ionization mechanisms and the charge exchange "scattering" reaction. The cross sections were utilitzed by the MGDO neutron transport code ANISN to model the transport of low energy

neutrals in a tokamak plasma. ANISN was found to adequately treat all aspects of the neutral transport process (e.g., geometry, cross section energy behavior, angular scattering effects, large attenuations, etc.). A parameter survey (over code variables) revealed a standard operating mode for ANISN neutral transport problems that would maintain calculational accuracy at a minimum in cost.

The advantage of the MGDO method is that fewer approximations and simplifications are used than in previous neutral analyses. These are pointed out in a variety of cases and their effects determined. In particular, the approximations that have gone into the widely used neutral transport module (generation method) of the Düchs plasma code were derived. The greater rigor of the MGDO method allowed its use as a benchmark in determining the accuracy of the generation method; and, it was found that the observed discrepancies were large enough so as to have a significant effect in the neutral module application. The origin of the disagreement was traced, in part, to several initial generation method approximations. Several time reduction techniques were further found to allow the MGDO method to be competitive (in execution time) with the generation method while maintaining calculational accuracy. It is determined, then, that the MGDO method is attractive as a neutral transport module and no serious problems can be foreseen in this implementation.

APPENDIX A

THE NEUTRAL MULTIGROUP CROSS SECTION CODE - GIMUXS

Input and Output Options

In the current version of GIMUXS input data is specified in the source deck and also read in on data cards. GIMUXS reads one input card for each set of material cross sections that are desired. Electron and ion processes are considered as separate cross section sets even though they may have the same temperature. Mixing of the materials with appropriate densities can be done in the transport code ANISN. The advantage of this system is that a permanent cross section library can be created from which ANISN can choose unequal temperature (and density) plasma components for a particular region.

The following is a listing of the variables supplied in the source deck which are necessary to generate cross sections for a particular library (it is assumed that a library contains sets with the same number of energy groups).

NLIB	0 No writing of cross sections on library data set. 1 Cross sections are being written at the beginning of a data set (library), unit 4. 2 Cross sections are being appended to an already existing data set, unit 4.
EPS	The relative error convergence criteria for the integration routines.
IGM	The number of energy groups.
IHM	The length of the cross section tables = 2*IGM + 2.
GLMTS(IGM+1)	The values of the energy group limits (eV).

The data card input is given below with the columns to be used by each variable, the variable name, and variable options or description.

Input Card (4I5, G10.4, 12A4)

Cols.	Name	Description
1-5	IT	1 $\leq$ Electron target 2 = Proton target 3 $\geq$ Mixed target ($N_i = N_e$, $T_i = T_e$)
6-10	IO	0 = P_o scattering component 1 = P_1 scattering component 2 = P_2 scattering component 3 = P_3 scattering component
11-15	K	7 = Library termination header. 1 = Print cross sections in ANISN format, unit 6.
16-20	ID	Material identification number.
21-30	TEMP	Material target temperature in eV.
31-78	LABEL	Vector containing a 48-character label.

It is advisable to have higher order scattering cross sections ($\ell>0$) for a particular material (e.g. T=100 eV protons) following one another in the input deck (order is arbitrary). GIMUXS will save the previous values of H_i^g (see Figure 4.3) so they may be used over again if the target temperature is close (or identical) to the previous temperature. GIMUXS writes the "material" cross section set into the special binary library (unit 4) with the following two unformatted write statements (standard ANISN format).

```
WRITE (4)  IGM,IHM,K,ID,LABEL
WRITE (4)  ((XSEC(I,J),I=1,IHM,J=1,IGM)
```

where XSEC = cross section matrix. The library is terminated by a header record with K=7 (supplied as the last card in the data input deck). ANISN will look through the entire library for each material requested, rewinding once if necessary.

Labelled COMMON Variables

GIMUXS uses labelled COMMON to transmit information between subroutines. The following is a listing of the variables in labelled COMMON.

COMMON/CHRGX1

- EP - E', the initial neutral energy (eV).
- E - The final neutral energy (eV) after charge exchange.
- A - Parameter constant for the charge exchange cross section fit.
- B - Parameter constant for the charge exchange cross section fit.
- TJAC - The Jacobian when transforming to the relative energy variable for integration.
- D - Conversion constant.

COMMON/ABSRB/

PMEV - Proton rest mass (eV).

EMEV - Electron rest mass (eV).

VCOEF - Conversion coefficient from $(\text{Energy (eV)})^{\frac{1}{2}}$ to speed (cm/sec).

ECOEF - Conversion coefficient from $(\text{speed (cm/sec)})^2$ to energy.

PI - π

XO, VMIN, VO - Parameters defined for integrating the absorption reaction rate.

COMMON/ITRGT

ITR - Target identification integer.

APPENDIX B

THE NEUTRAL ANALYSIS PROGRAM - NEUTER

The displayed output of the transport calculation performed by the MGDO code ANISN is limited in its application for neutral analysis. It is common for the nuclear engineer to be interested in the flux of neutrons at a point in order to calculate volumetric reaction rates (activities) while the plasma physicist is traditionally interested in the neutral density. A detailed accounting of the neutral outflux is also required. For these reasons the standard output of an ANISN neutral run is dumped into an external file and the results are reformulated by the program NEUTER. Most of the data needed is read directly from the external file but additional input may be required (e.g. energy group structure, sputtering yields). The quantities described below are used or calculated by NEUTER.

Read from the external file:

$\phi(x_i, \bar{E}_g, \Omega_j)$ ≡ The angular flux solution as a function of energy and position (cm^{-2} sec^{-1}).

$\phi_{Bound}(\bar{E}_g, \Omega_j)$ ≡ The angular flux solution at the outer boundary (cm^{-2} sec^{-1}).

A_{Bound} ≡ The boundary surface area.

w_j, μ_j ≡ The angular quadrature weights and cosines.

Inputted to NEUTER:

E_g ≡ The energy group limits (eV).

$S(\bar{E}_g, \Omega_j)$ ≡ Neutral sputtering yields as a function of energy and angle cosine to the normal (atoms/atom).

Calculated by NEUTER:

$\bar{E}_g$ ≡ The centered group energy
$= (E_g + E_{g+1})/2$ (eV).

$\bar{v}_g$ ≡ The centered group velocity (cm sec^{-1}).

$\phi(x_i, \bar{E}_g)$ ≡ The scalar flux as a function of position and energy
$= \sum_j \phi(x, \bar{E}_g, \Omega_j) w_j$ (cm^{-2} sec^{-1}).

$n(x_i, \bar{E}_g)$ ≡ The scalar density as a function of position and energy
$= \frac{\phi(x_i, \bar{E}_g)}{\bar{v}_g}$ (cm^{-3}).

$n(x_i)$ ≡ The total density as a function of position
$= \sum_g n(x_i, \bar{E}_g)$ (cm).

$SPEC(x_i,\bar{E}_g)$ ≡ The density spectrum as a function of position and energy

$$= \frac{n(x_i,\bar{E}_g)}{n(x_i)} \times \frac{1}{\bar{E}_g - \bar{E}_{g+1}} \ (cm^{-2}\ sec^{-1}eV^{-1}).$$

$E_{Avg}(x_i)$ ≡ The average energy of the density spectrum as a function of position

$$= \sum_g \bar{E}_g\ n(x_i,\bar{E}_g)/n(x_i) \qquad (eV).$$

J_{Bound} ≡ The total outward boundary current

$$= \sum_g \sum_j^{out} Q_{Bound}(\bar{E}_g,\Omega_j)w_j\mu_j \qquad (cm^{-2}\ sec^{-1}).$$

$SPEC_{Bound}(\bar{E}_g)$ ≡ The outward boundary current spectrum

$$= \frac{\sum_j^{out} \phi_{Bound}(\bar{E}_g,\Omega_j)w_j\mu_j\left(\frac{1}{\bar{E}_g - \bar{E}_{g+1}}\right)}{J_{Bound}}$$

$(cm^{-2}\ sec^{-1}\ eV^{-1})$.

E_{Avg}^{Bound} ≡ The average energy of the outward boundary boundary current (eV).

$$= \frac{1}{J_{Bound}} \sum_g \sum_j^{out} \bar{E}_g\ \phi_{Bound}(\bar{E}_g,\Omega_j)w_j\mu_j.$$

GAMMA ≡ The plasma albedo

$$= \frac{J_{Bound} \cdot A_{Bound}}{J_{in} = 1} .$$

SPUT ≡ The effective sputtering yield of the outflux (atoms/atom)

$$= \frac{1}{J_{Bound}} \sum_g \sum_j^{out} \phi_{Bound}(\bar{E}_g,\Omega_j)w_j\Omega_j \times S(\bar{E}_g,\Omega_j) .$$

APPENDIX C

GENERATION METHOD NEUTRAL TRANSPORT

In this appendix the approximate neutral transport equation used by the Düchs generation method is derived.

The Düchs treatment is based upon the integral form of the transport equation (C.1) [36].

$$\Phi(\underline{r},\underline{\Omega},E) = \int_0^{\infty} \exp\left[-\int_0^{s'} \sigma_a^{eff}(\underline{r}-s''\underline{\Omega},E)\,ds''\right] \times \left(\int_{E',\underline{\Omega}'} \Phi(\underline{r},\underline{\Omega}',E')\, K_s^{eff}(\underline{r};E'\underline{\Omega}'\rightarrow E\underline{\Omega})\,dE'd\Omega' + Q(\underline{r}-s'\underline{\Omega},\underline{\Omega},E) \right) ds' \quad , \tag{C.1}$$

where the symbols are defined for neutral transport in equation (3.17). An iterative solution technique for the neutral density leads to the identification of the resulting series as representing "generations" of charge exchange neutrals. (We therefore refer to the Düchs neutral treatment as the generation method.) We see this by examining equation (C.1) with the following series generated for the flux:

$$\Phi = \sum_{i=1}^{n} L^{i} \Phi + \Phi_{o} , \qquad (C.2)$$

where L is the integral transport operator and Φ_o is the uncollided neutral flux. The sum of the terms in equation (C.2) represents the solution, provided the series converges. The presence of ionization (absorption) of neutrals guarantees this [5,9] since the effective expansion parameter of the series, β, is given as

$$\beta = \frac{\langle \sigma v \rangle_{cx}}{\langle \sigma v \rangle_{cx} + \langle \sigma v \rangle_{ei}} < 1 , \qquad (C.3)$$

where $\langle \sigma v \rangle_{cx}$ and $\langle \sigma v \rangle_{ei}$ are average reaction rates for charge exchange and electron impact ionization. What is not known though, is the number of terms required for an accurate solution, since β does not solely gauge the relative size of the terms in the series [9]. If the optical depth of the plasma is defined as

$$\rho = \int_{o}^{r_o} dr' \left(\frac{N_i \langle \sigma v \rangle_{cx}}{v_n} + \frac{N_e \langle \sigma v \rangle_{ei}}{v_n} \right) , \qquad (C.4)$$

where r_o is the minor radius and v_n is a characteristic neutral velocity, then for plasmas with $\rho >> 1$, many more terms are required in the series solution to account for the high collisionality. Ten generations of charge exchange

neutrals have usually been used, but it has been pointed out that this may not be adequate for higher density plasmas [1,9].

To follow the approximations introduced by the generation method in treating the exact problem we substitute equations (3.14) and (3.15) into equation (C.1) and solve for the angular neutral density in dE about E and dΩ about $\underline{\Omega}$ as

$$n(\underline{r},\underline{\Omega},E)\,d\Omega\,dE \tag{C.5}$$

$$= \int_0^\infty ds'\ \exp\left[-\int_0^{s'} ds''\left(\frac{N_i(\underline{r}-s''\underline{\Omega})\langle\sigma v\rangle_{cx}(\underline{r}-s''\underline{\Omega},E)}{v} + \frac{N_e(\underline{r}-s''\underline{\Omega})\langle\sigma v\rangle_{ei}(\underline{r}-s''\underline{\Omega},E)}{v}\right)\right]$$

$$\times \frac{N_i(\underline{r}-s'\underline{\Omega})}{4\pi v}\, h_i(\underline{r}-s'\underline{\Omega},E) \int_{E',\underline{\Omega}'} n(\underline{r}-s'\underline{\Omega},\underline{\Omega}',E')\,|\underline{v}-\underline{v}'|$$

$$\times \sigma_{cx}(|\underline{v}-\underline{v}'|)\,dE'\,d\Omega'\,dE\,d\Omega,$$

where we have neglected ion impact ionization, (a good approximation for E < 10 keV), and have identified

$$\langle\sigma v\rangle_{cx}(\underline{r},E) = \int_{E',\underline{\Omega}'} h_i(\underline{r},E')\,|\underline{v}-\underline{v}'|\,\sigma_{cx}(|\underline{v}-\underline{v}'|)\,\frac{dE'\,d\Omega'}{4\pi}, \tag{C.6}$$

(C.7)

$$\langle \sigma v \rangle_{e;}(\underline{r},E) = \int_{E',\underline{\Omega}'} h_e(\underline{r},E')\,|\underline{v}-\underline{v}'|\,\sigma_{e;}(|\underline{v}-\underline{v}'|)\,\frac{dE'\,d\Omega'}{4\pi}.$$

The iterative solution scheme leads to identifying the angular density in the integrand of equation (C.5) as that of the current "generation". We write for the next generation (n^{g+1}), then

(C.8)

$$n^{g+1}(\underline{r},\underline{\Omega},E)\,dE\,d\Omega$$

$$= \int_0^{\bar{s}} ds' \quad exp\left[-\int_0^{s'} ds''\left(\frac{N_i(\underline{r}-s''\underline{\Omega})\langle\sigma v\rangle_{cx}}{v} + \frac{N_e(\underline{r}-s''\underline{\Omega})\langle\sigma v\rangle_{ei}}{v}\right)\right]$$

$$\times \frac{N_i}{4\pi v}\; h_i \int_{E',\underline{\Omega}'} n^g(\underline{r}-s'\underline{\Omega},\underline{\Omega}',E')\,|\underline{v}-\underline{v}'|$$

$$\times \sigma_{cx}(|\underline{v}-\underline{v}'|)\,dE'\,d\Omega'\,dE\,d\Omega.$$

The third line of equation (C.8) represents the source of charge exchange neutrals for the g + 1 generation. The source is a function of the angle $\underline{\Omega}$ because of the coupling between $\underline{\Omega}$ and $\underline{\Omega}'$ in the relative velocity $|\underline{v} - \underline{v}'|$ and the general angular dependence of $n_g(\underline{\Omega}')$ (the angular density of the current generation). A great deal of simplification can

be realized, however, by effectively eliminating the dependence. There are several physical situations that may justify this assumption. These have been mentioned before (Chapter 4) namely; that the charge exchange cross section can be approximated as in equation (4.6), it can be assumed that the energies of the neutrals are either much greater than or much less than those of the target ions (which will occur in certain regions of the plasma), or the angular density of the previous generation of neutrals is isotropic (independent of $\underline{\Omega}'$, this would be the case in an infinite homogeneous medium problem). Any of the assumptions allow the decoupling of the angular integral in the source function which leads to an approximation for the new charge exchange source as

(C.9)

$$\frac{N_i(\underline{r}-s'\underline{\Omega})}{4\pi V} h_i(\underline{r}-s'\underline{\Omega}, E) \int_{E',\underline{\Omega}'} n^g(\underline{r}-s'\underline{\Omega}, \underline{\Omega}', E') \times |\underline{v}-\underline{v}'| \sigma_{cx}(|\underline{v}-\underline{v}'|) dE' d\Omega' dE d\Omega$$

$$= \frac{N_i}{4\pi V} h_i \int_{E'} n^g(\underline{r}-s'\underline{\Omega}, E') \times \int_{\underline{\Omega}'} |\underline{v}-\underline{v}'| \sigma_{cx}(|\underline{v}-\underline{v}'|) \frac{d\Omega'}{4\pi} dE' dE d\Omega ,$$

where $n^g(\underline{r}-s'\underline{\Omega},E') = \int n^g(\underline{r}-s'\underline{\Omega},\underline{\Omega}',E')d\Omega'$. With this approximation, equation (C.8) can be rewritten as

$$n^{g+1}(\underline{r},\underline{\Omega},E)\,dE\,d\Omega$$

$$= \int_0^\infty ds' \exp\left[-\int_0^{s'} ds'' \left(\frac{N_i(\underline{r}-s''\underline{\Omega})\langle\sigma v\rangle_{cx}}{v} + \frac{N_e(\underline{r}-s''\underline{\Omega})\langle\sigma v\rangle_{ei}}{v}\right)\right] \tag{C.10}$$

$$\times \frac{N_i(\underline{r}-s'\underline{\Omega})}{4\pi v}\, h_i \int_{E'} n^g(r-s'\underline{\Omega},E') \times \int_{\underline{\Omega}'} |\underline{v}-\underline{v}'|\,\sigma_{cx}(|\underline{v}-\underline{v}'|)\,\frac{d\Omega'dE'}{4\pi}\,dE\,d\Omega.$$

The Düchs treatment additionally assumes that the just born neutrals are monoenergetic with a kinetic energy related to the local ion temperature at the point of creation. This specification implies that the ion distribution function is approximated as

$$h_i(\underline{r}-s'\underline{\Omega},E) = \delta(E - kT_i(\underline{r}-s'\underline{\Omega})). \tag{C.11}$$

Substituting equation (C.11) into equation (C.10) and performing the integration over energy yields

$$n^{g+1}(\underline{r},\underline{\Omega})\,d\Omega = \int_0^\infty n^{g+1}(\underline{r},\underline{\Omega},E)\,dE\,d\Omega$$

$$= \int_0^\infty ds' \exp\left[-\int_0^{s'} ds''\left(\frac{N_i(\underline{r}-s''\underline{\Omega})\langle\sigma v\rangle_{cx}(T_i)}{V_i} + \frac{N_e(\underline{r}-s''\underline{\Omega})\langle\sigma v\rangle_{ei}(T_i)}{V_i}\right)\right] \tag{C.12}$$

$$\times \frac{N_i(\underline{r}-s'\underline{\Omega})}{4\pi V_i}\int_{E'} n^g(\underline{r}-s'\underline{\Omega},E')$$

$$\times \int_{\underline{\Omega}'} |\underline{V}_i-\underline{V}'|\,\sigma_{cx}(|\underline{V}_i-\underline{V}'|)\,\frac{d\Omega'\,dE'\,d\Omega}{4\pi},$$

where

$$V_i(\underline{r}-s'\underline{\Omega}) = \left(\frac{2kT_i(\underline{r}-s'\underline{\Omega})}{m_i}\right)^{\frac{1}{2}}. \tag{C.13}$$

The energy distribution of the current generation (n^g) is now specified, assumed monoenergetic and represented by

$$n^g(\underline{r}-s'\underline{\Omega},E') = n^g(\underline{r}-s'\underline{\Omega})\,\delta(E'-kT^g(\underline{r}-s'\underline{\Omega})). \tag{C.14}$$

The "temperature" at the radial position $\underline{r}$ is given by averaging over the temperatures of the neutrals that reach the point $\underline{r}$. i.e.

$$T^{g+1}(\underline{r}) = \int T_i(\underline{r}-s'\underline{\Omega})\,dn^g(\underline{r}-s'\underline{\Omega}) \Big/ n^{g+1}(\underline{r}). \tag{C.15}$$

Equation (C.14) is substituted into equation (C.12) to give

$$n^{g+1}(\underline{r},\underline{\Omega})\,d\Omega = \int_0^{\infty} ds'\,d\Omega\, \frac{N_i(\underline{r}-s'\underline{\Omega})}{4\pi V_i}\, n^{g}(\underline{r}-s'\underline{\Omega})\,\overline{\langle\sigma v\rangle}_{cx}(\underline{r}-s'\underline{\Omega}) \tag{C.16}$$

$$\times \exp\left[-\int_0^{s'} ds''\left(\frac{N_i(\underline{r}-s''\underline{\Omega})\langle\sigma v\rangle_{cx}(T_i)}{V_i} + \frac{N_e(\underline{r}-s''\underline{\Omega})\langle\sigma v\rangle_{ei}(T_i)}{V_i}\right)\right],$$

where

$$\overline{\langle\sigma v\rangle}_{cx}(\underline{r}-s'\underline{\Omega}) = \int_{E',\underline{\Omega}'} \delta\left(E'-kT^{g}(\underline{r}-s'\underline{\Omega})\right) \times |\underline{V}_i-\underline{V}'|\,\sigma_{cx}(|\underline{V}_i-\underline{V}'|)\,dE'\,\frac{d\Omega'}{4\pi}. \tag{C.17}$$

Attention is now brought to the evaluation of the angle integrals of equation (C.16). Since the calculation will be carried out in infinite cylindrical geometry (one space dimension) the solid angle is given by

$$\int_{\underline{\Omega}} d\Omega = \int_0^{2\pi} d\theta \int_{-1}^{1} d\mu, \tag{C.18}$$

where

$$\cos\theta = \frac{\hat{\underline{\Omega}}\cdot\underline{r}}{|\underline{r}|}, \qquad \mu = \frac{\underline{\Omega}\cdot\underline{z}}{|\underline{z}|} = \cos\phi. \tag{C.19}$$

The orientation of the angles is shown in Figure (C.1). The unit vector $\hat{\underline{\Omega}}$ is assumed to lie in the x-y plane. When the integration over $\underline{\Omega}$ is performed for equation (C.16), s' and s" refer to the line integrals along the direction $\underline{\Omega}$. The line integrals can be simplified to in-plane distances ($\hat{s}'$ and $\hat{s}''$ in the x-y plane of Figure C.1(a)) by noticing that

$$ds' = \frac{d\hat{s}'}{\sqrt{1-\mu^2}} \tag{C.20}$$

and

$$ds'' = \frac{d\hat{s}''}{\sqrt{1-\mu^2}} \, .$$

Using equations (C.20) and integrating over $\underline{\Omega}$, equation (C.16) becomes

$$n^{g+1}(\underline{r}) = \int_0^{2\pi}\int_{-1}^{1} n^{g+1}(\underline{r},\underline{\Omega})\, d\mu\, d\theta \tag{C.21}$$

$$= \int_0^{2\pi} \frac{d\theta}{4\pi} \int_{-1}^{1} d\mu \int_{P''(\underline{r})}^{P(\underline{r},\theta)} \frac{d\hat{s}'}{\sqrt{1-\mu^2}} \; \frac{N_i(\underline{r}-\hat{s}'\hat{\underline{\Omega}})}{v_i} n^g(\underline{r}-\hat{s}'\hat{\underline{\Omega}}) \langle \overline{\sigma v} \rangle_{ex}$$

$$\times \exp\left[- \int_{P'(\hat{s}')}^{P''(\underline{r})} \frac{d\hat{s}''}{\sqrt{1-\mu^2}} \left(\frac{N_i(\underline{r}-\hat{s}''\hat{\underline{\Omega}}) \langle \sigma v \rangle_{ex}(T_i)}{v_i} \right.\right.$$

$$\left.\left. + \frac{N_e(\underline{r}-\hat{s}''\hat{\underline{\Omega}}) \langle \sigma v \rangle_{ei}(T_i)}{v_i} \right) \right] ,$$

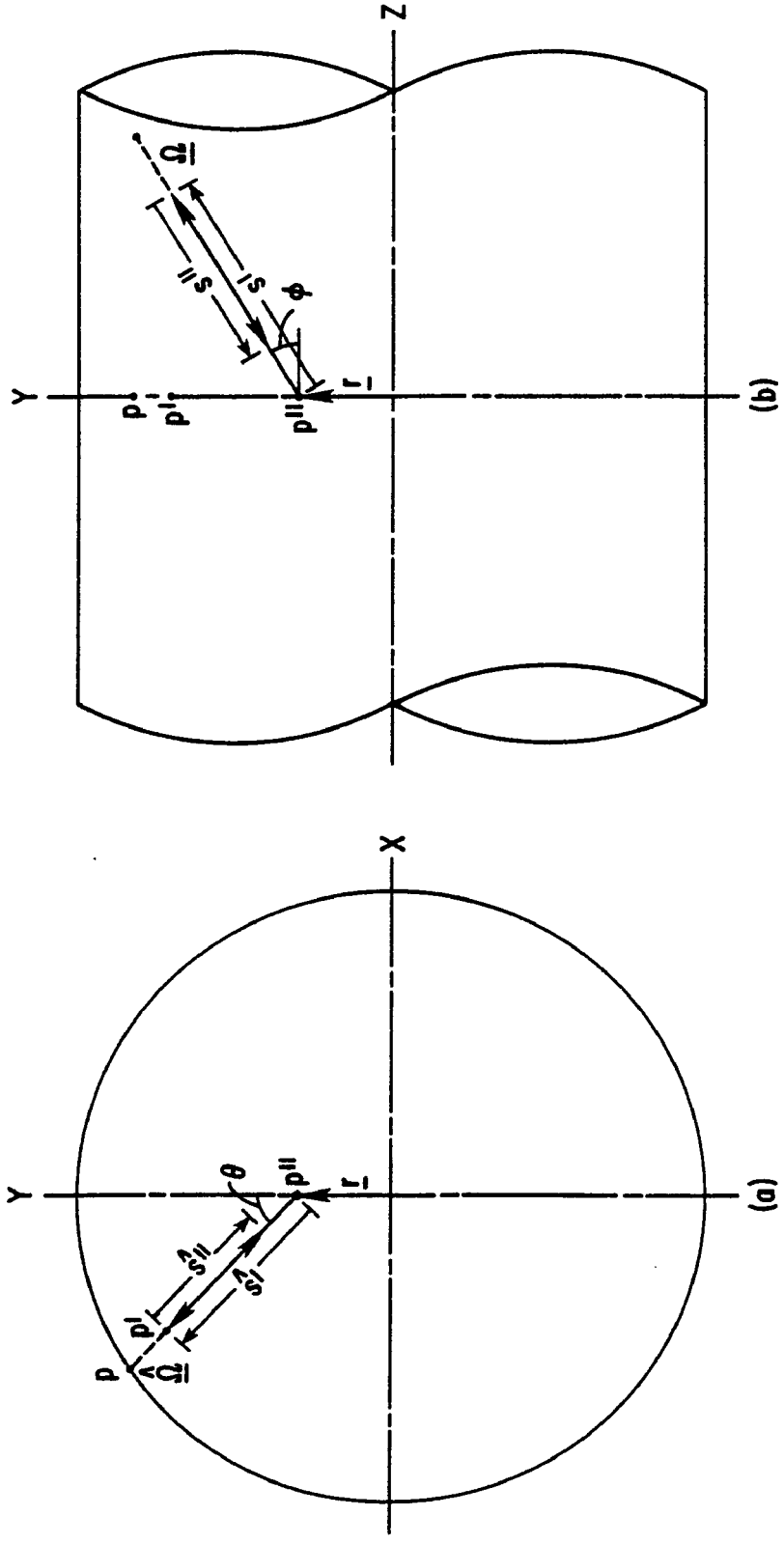

Figure C.1 Orientation of vectors for the integration of equation (C.21) in infinite cylindrical geometry. The vectors in (a) lie in the X-Y plane. In (b) the X axis points into the paper.

where the line integrals are now over $\hat{s}'$ and $\hat{s}''$ and the limits are given in Figure (C.1). Since $n^g(\underline{r})$ is independent of μ, the integral over the variable μ may be brought out of equation (C.21) to yield an integral of the form:

(C.22)

$$I(\hat{s}') = \int_{-1}^{1} d\mu \frac{1}{\sqrt{1-\mu^2}} \exp -\left[\frac{1}{\sqrt{1-\mu^2}} \rho(\hat{s}')\right],$$

where we have identified the optical depth as

$$\rho(\hat{s}') = \int_{P'(\hat{s}')}^{P''(\underline{r})} d\hat{s}'' \left(\frac{N_i(\underline{r}-\hat{s}''\hat{\underline{\Omega}}) \langle \sigma v \rangle_{cx}(T_i)}{v_i} + \frac{N_e(r-\hat{s}''\hat{\underline{\Omega}}) \langle \sigma v \rangle_{ei}(T_i)}{v_i} \right). \tag{C.23}$$

To perform the integral of equation (C.22) we introduce the convenient change of variables

$$\mu = \tanh t, \tag{C.24}$$

which allows equation (C.22) to be written as

(C.25)

$$I(\hat{s}') = 2 \int_0^{\infty} \frac{\exp[-\rho(\hat{s}')\cosh t]}{\cosh t} dt = 2 K_{i_1}(\rho),$$

where Ki_1 is identified as the first repeated integral of the Bessel function [65].

With the result (C.25), equation (C.21) can be simplified to the form

(C.26)

$$n^{g+1}(\underline{r}) = \int_0^{\pi} \frac{d\theta}{\pi} \int_{\rho''(\underline{r})}^{\rho(\underline{r},\theta)} \frac{N_i(\underline{r}-\hat{s}'\hat{\Omega})}{v_i} n^g \langle\overline{\sigma v}\rangle_{cx} Ki_1(\rho)\, d\hat{s}',$$

where we have used the fact that the solution will be symmetric about $\theta=\pi$.

The complicated dependence of Ki_1 on ρ can be approximated (to within 10%) by the exponential function in the range $.4 < \rho < 1$, as seen from Figure (C.2), which corresponds to the optical depth of many plasmas (e.g. for ST $\rho \sim .8$). However, most plasmas of current and future interest (PLT, TFTR, ALCATOR) have optical depths $\rho \geq 3$. For this range the exponential approximation is no longer valid. Notwithstanding this restriction, the exponential approximation allows equation (C.26) to be reduced to

$$n^{g+1}(\underline{r}) = \int_0^{\pi} \frac{d\theta}{\pi} \int_{\rho''(\underline{r})}^{\rho(\underline{r},\theta)} \frac{N_i(\underline{r}-\hat{s}'\hat{\Omega})}{v_i} n^g(\underline{r}-\hat{s}'\hat{\Omega}) \times \langle\overline{\sigma v}\rangle_{cx}(\underline{r}-\hat{s}'\hat{\Omega})\, e^{-\rho(\hat{s}')}\, d\hat{s}'. \tag{C.27}$$

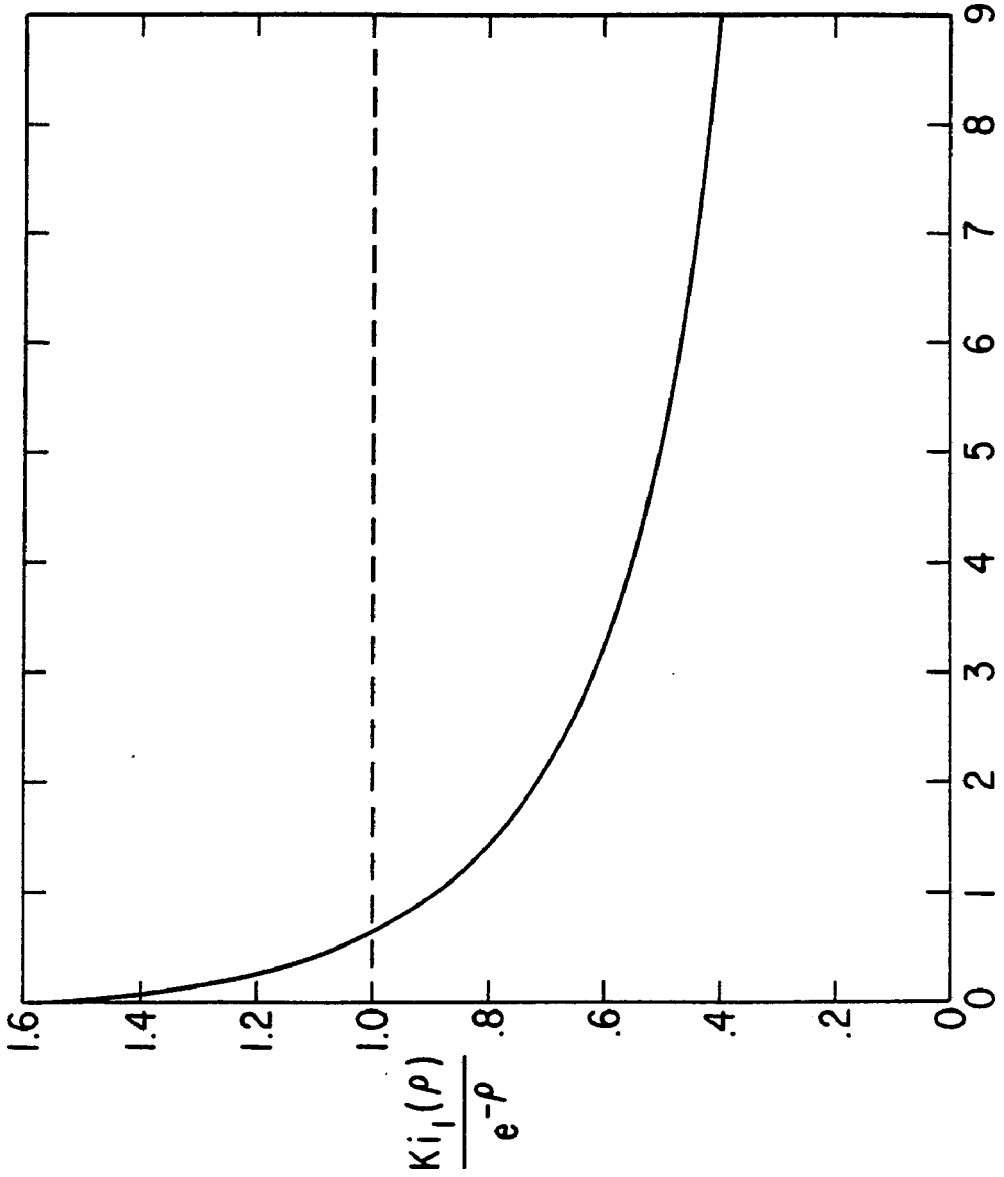

Figure C.2 The ratio of the First Repeated Integral of the Bessel Function (Ki_1) to the Exponential Function ($e^{-\rho}$) for values of the argument ρ.

Equation (C.27) is the approximation to the integral Boltzmann equation that is solved for the neutral atom distribution by the generation method.

We review the approximations that have been used to arrive at equation (C.27). The charge exchange source was assumed to be a function of the density $n^g(\underline{r},E')$ rather than the angular density $n^g(\underline{r},\underline{\Omega}',E')$. This has the effect of removing the $\underline{\Omega}$ dependence from the charge exchange source and simplifies the computational solution. Regarding the energy variable, the ion distribution function was assumed to be $\delta(E-kT_i)$, and thus monoenergetic at the local kT_i. The energy distribution of the current neutral generation ($n^g(E)$) is also assumed monoenergetic at a kT^g. The "temperature", kT^g, is obtained as an average over the temperatures of the neutrals that reach the point in question. Finally, the exponential function is used as an approximation to the function Ki_1 in the integral attenuation term. The latter function is arrived at by integrating out the angular coordinate corresponding to the z axis in infinite cylindrical geometry. This approximation is seen to be valid for only a small range of the attenuation parameter ρ (seen in Figure (C.2)).

LIST OF REFERENCES

1. D. N. ZUBAREV, U. N. KLIMOV, Plasma Physics and the Problem of Controlled Thermonuclear Reactions, (Pergamon Press, New York, 1959) Vol. 1, p. 162.

2. E. GREENSPAN, Nuclear Fusion 14, 771 (1974).

3. W. W. ENGLE, JR., A Users Manual for ANISN, Oak Ridge Gaseous Diffusion Plant Report K-1693 (1967).

4. Y. N. DNESTROVSKII, D. P. KOSTOMAROV, N. L. PAVLOVA, Princeton Plasma Physics Laboratory Report Translation MATT-TRANS 107 (1971).

5. S. REHKER, H. WOBIG, Plasma Physics 15, 1083 (1973).

6. J. T. HOGAN, J. F. CLARKE, Surface Effects in Controlled Fusion, H. Wiedersich, M. S. Kaminsky, K. M. Zwilsky, eds. (North-Holland Publishing Company, Amsterdam, 1974) pp. 1-8.

7. J. F. CLARKE, D. J. SIGMAR, Proceedings of the Seventh European Conference on Controlled Fusion and Plasma Physics (Centre de Recherches en Physique des Plasmas, Lausanne, 1975) Vol. I, p. 134.

8. D. F. DÜCHS, D. E. POST, P. H. RUTHERFORD, Nuclear Fusion 17, 565 (1977).

9. K. MOLVIG, Massachusetts Institute of Technology, Research Laboratory of Electronics Report (April 1976).

10. B. LEHNERT, Nuclear Fusion 8, 173 (1968).

11. H. HINNOV, J. Nucl. Mat. 53, 9 (1974).

12. D. L. DIMOCK, H. P. EUBANK, E. HINNOV, L. C. JOHNSON, E. B. MESERVEY, Nuclear Fusion 13, 271 (1973).

13. A Fusion Power Plant, R. G. Mills, ed., Princeton Plasma Physics Laboratory Report MATT-1050 (1974).

14. T. KAMMASH, Fusion Reactor Physics - Principles and Technology. (Ann Arbor Science Publishers, Ann Arbor, Michigan, 1975).

15. E. HINNOV, Princeton Plasma Physics Laboratory Report MATT-270 (1964).

16. E. McDANIEL, Collisional Phenomena in Ionized Gases, (John Wiley and Sons, Inc., New York. 1964).

17. B. COPPI, et al., Massachusetts Institute of Technology Report PRR-7417 (1974).

18. W. STODIEK, K. BOL, H. EUBANK, S. VON GOELER, D. J. GROVE, Plasma Physics and Controlled Nuclear Fusion Research (International Atomic Energy Agency, Vienna, 1971) Vol. I, pp. 465-478.

19. J. G. CORDEY, W. G. F. CORE, J. SHEFFIELD, Nuclear Fusion 15, 755 (1975).

20. S. A. COHEN, J. Nucl. Mat. 63, 65 (1976).

21. J. G. GILLIGAN, S. L. GRALNICK, W. G. PRICE, JR., Bull. Am. Phys. Soc. 19, 853 (1974).

22. J. H. MARABLE, E. M. OBLOW, Nuclear Science and Engineering 61, 90 (1976).

23. Z. EL DERINI, E. M. GELBARD, Trans. Am. Nucl. Soc. 23, 45 (1976).

24. J. G. GILLIGAN, S. L. GRALNICK. W. G. PRICE, JR., T. KAMMASH, Proc. Annual Mtg. Theoretical Aspects of Controlled Thermonuclear Research, Paper 3A-4, Madison, Wisconsin (1976).

25. W. PFEIFFER, Gulf General Atomic Report GA-A13995 (1976).

26. K. H. BURREL, Gulf General Atomic Report GA-A14113 (1976).

27. B. R. WIENKE, W. F. MILLER, JR., T. J. SEED, P. L. ROOD, Los Alamos Scientific Laboratory Report LA-UR 77-839 (1977).

28. A. M. WEINBERG, E. P. WIGNER, The Physical Theory of Neutron Chain Reactors (University of Chicago Press, Chicago, 1958).

29. J. R. LAMARSH, Introduction to Nuclear Reactor Theory (Addison-Wesley Publishing Co. Inc., Reading, Massachusetts, 1966).

30. J. J. DUDERSTADT, G. W. HAMILTON, Nuclear Reactor Analysis, (John Wiley & Sons, Inc., New York, 1976).

31. A. C. RIVIÈRE, Nuclear Fusion 11, 363 (1971).

32. W. LOTZ, The Astrophysical Journal, Supplemental Series, 14, No. 128, 207 (1967).

33. S. REHKER, E. SPETH, Max-Plank-Institut für Plasmaphysik Report IPP2/217 (1974).

34. R. L. FREEMAN, E. M. JONES, Culham Laboratory Report CLM-R 137 (1974).

35. R. E. OLSEN, A. SALOP, Stanford Research Institute Report MP 77-59 (1977).

36. G. I. BELL, S. GLASSTONE, Nuclear Reactor Theory (Van Nostrand Rheinhold Company, New York, 1970).

37. M. T. ROBINSON, Proceedings of the 3rd National Conference, Atomic Collisions in Solids, Kiev, USSR, October 1974.

38. J. G. GILLIGAN, S. L. GRALNICK, W. G. PRICE, JR., T. KAMMASH, presented orally at Conference on Atomic Processes in High Temperature Plasmas, Knoxville, February 1977.

39. K. M. CASE, P. F. ZWEIFEL, Linear Transport Theory (Addison-Wesley Publishing Co., Reading, Massachusetts, 1967).

40. Computing Methods in Reactor Physics, H. Greenspan, C. N. Kelber, D. Okrent, eds., (Gordon and Breach, New York, 1968).

41. K. D. LATHROP, Reactor Technology 15, 107 (1972).

42. G. L. BLACKSHAW, R. L. MURRAY, Nuclear Science and Engineering 27, 520 (1967).

43. N. A. KRALL, A. W. TRIVELPIECE, Principles of Plasma Physics, (McGraw-Hill Book Co., New York, 1973) p. 5.

44. R. L. MILLER, G. H. MILEY, University of Illinois Nuclear Engineering Report COO-2218-26 (1975).

45. R. L. MILLER, G. H. MILEY, Proceedings of the Second Topical Meeting of the Technology of Controlled Nuclear Fusion, (Natl. Technical Information Service, Springfield, Virginia, 1976) Vol. II, pp. 515-527.

46. B. G. CARLSON, K. D. LATHROP, Computing Methods in Reactor Physics, H. Greenspan, C. N. Kelber, D. Okrent, eds., (Gordon and Breach, New York, 1968) p. 171.

47. K. D. LATHROP, Nuclear Science and Engineering 24, 381 (1966).

48. G. I. BELL, G. E. HANSEN, H. A. SANDMEIER, Nuclear Science and Engineering 28, 376 (1967).

49. R. BEHRISCH, paper presented at the Erice "Summer School 1976 of Tokamak Reactors for Breakeven", Erice, Italy, September, 1976.

50. J. E. MOREL, B. R. WIENKE, Los Alamos Scientific Laboratory Report LA-6661-MS (1977).

51. W. PFEIFFER, Gulf General Atomic Report GA-A14159 (1976).

52. F. H. TENNEY, Private Communication (1975).

53. P. HENRICI, Elements of Numerical Analysis (John Wiley & Sons, Inc., New York, 1964).

54. W. G. PRICE, JR., Princeton Plasma Physics Laboratory Report MATT-1035 (1974).

55. Tokamak Fusion Test Reactor, Final Conceptual Design Report, Princeton Plasma Physics Laboratory Report PPPL-1275 (1976).

56. Tokamak Experimental Power Reactor Conceptual Design, Argonne National Laboratory Report ANL/CTR-76-3 (1976).

57. D. W. DRAWBAUGH, Nuclear Science and Engineering 44, 58 (1971).

58. S. L. GRALNICK, Nuclear Science and Engineering 60 302 (1976).

59. J. JUNG, Nuclear Science and Engineering 60, 74 (1976).

60. D. E. POST, Private Communication (1976).

61. K. BOL, et al., Plasma Physics and Controlled Nuclear Fusion Research (International Atomic Energy Agency, Vienna, 1975).

62. D. M. MEADE, H. P. FURTH, P. H. RUTHERFORD, F. G. R. SEIDL, D. F. DÜCHS, Plasma Physics and Controlled Nuclear Fusion Research (International Atomic Energy Agency, Vienna, 1975) Vol. I, pp. 605-619.

63. P. SIGMUND, Phys. Rev. 89, 383 (1969).

64. A. J. SUMMER, N. J. FREEMAN, N. R. DALY, J. Appl. Phys. 42, 4774 (1971).

65. Handbook of Mathematical Functions, M. Abramowitz, I. A. Stegun, eds., (National Bureau of Standards, Washington, D. C., 1964) p. 483.